Modeling the local reaction environment in CO2 electrolysis

Butt, E.N.

DOI
10.4233/uuid:d37a2d0c-84df-403b-a172-8e5cb767c656

Publication date
2025

Document Version
Final published version

Citation (APA)
Butt, E. N. (2025). *Modeling the local reaction environment in CO2 electrolysis*. [Dissertation (TU Delft), Delft University of Technology]. https://doi.org/10.4233/uuid:d37a2d0c-84df-403b-a172-8e5cb767c656

MODELING THE LOCAL REACTION ENVIRONMENT IN CO_2 ELECTROLYSIS

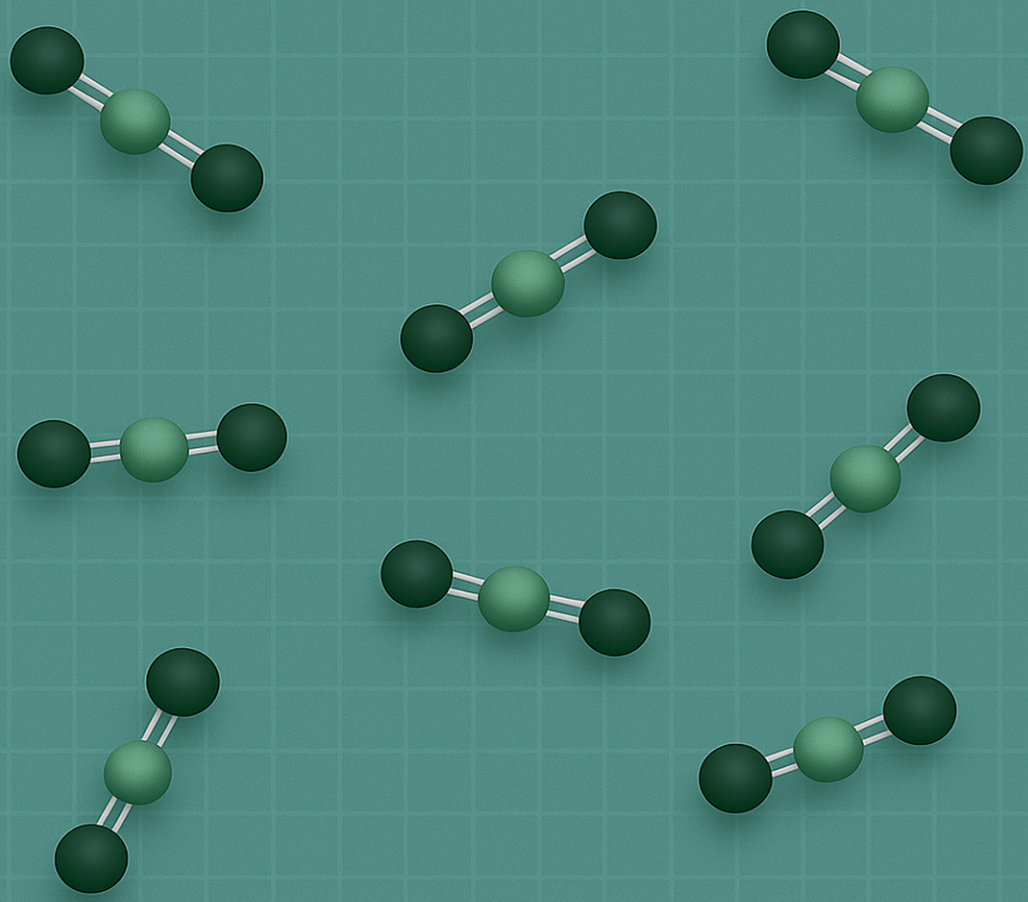

Esaar Naeem Butt

MODELING THE LOCAL REACTION ENVIRONMENT IN CO_2 ELECTROLYSIS

MODELING THE LOCAL REACTION ENVIRONMENT IN CO_2 ELECTROLYSIS

Dissertation

for the purpose of obtaining the degree of doctor
at Delft University of Technology
by the authority of the Rector Magnificus, prof.dr.ir. T.H.J.J. van der Hagen,
chair of the Board for Doctorates
to be defended publicly on
Friday 23 May 2025 at 10:00 o'clock

by

Esaar NAEEM BUTT

Master of Science in Chemical & Energy Engineering,
Otto von Guericke University Magdeburg, Germany,
born in Gujranwala, Pakistan.

This dissertation has been approved by the promotors. Composition of the doctoral committee:

Rector Magnificus	Chairperson
Prof. dr. ir. J. T. Padding	Delft University of Technology, Promotor
Dr. ir. R. M. Hartkamp	Delft University of Technology, Promotor
Independent members:	
Prof. dr. A.J. Houtepen	Delft University of Technology
Prof. dr. V. Garbin	Delft University of Technology
Prof. dr. ir. R.G.H. Lammertink	University of Twente
Prof. dr. B. Rotenberg	Sorbonne University
Dr. T. E. Burdyny	Delft University of Technology

This work is part of the research programme Towards large-scale electroconversion systems (TOeLS) financed by Shell and the Topsectors Chemistry, HTSM and Energy.

Printed by: Proefschriftenprinten | www.Proefschriftenprinten.nl

Cover by: Esaar Naeem Butt. Designed using DALL·E 3 and Canva.

CONTENTS

SUMMARY

The pressing need to address climate change and resource sustainability has catalyzed interest in technologies that can effectively mitigate CO_2 emissions. Electrochemical reduction of CO_2 is one such technology, offering a pathway to convert CO_2 into valuable chemicals and fuels using renewable electricity. Despite its promise, the industrial application of CO_2 electrolysis faces significant challenges, including limited mass transport, inefficient reaction kinetics, and poor control over the local reaction environment at the catalyst interface. This dissertation tackles these challenges through advanced numerical modeling. The research identifies key bottlenecks, such as CO_2 solubility limits and local pH shifts, and explores strategies to overcome them using innovative electrode designs and operation modes. By extending the Poisson–Nernst–Planck framework to include finite size effects and the Frumkin-corrected Tafel relation, this work provides a detailed understanding of the electric double layer, steric effects, and solvent dynamics near the catalyst surface for H-cell configurations. These models are validated against experimental data, ensuring their robustness and applicability.

Gas diffusion electrodes offer significant advantages over traditional H-cell systems by enabling direct CO_2 delivery to the reaction site. However, these systems introduce new complexities, such as the interplay between pore structure, ion transport, and local reaction conditions. By simulating the behavior of these gas diffusion electrodes under various operating conditions, the research identifies optimal configurations for an ideal local reaction environment, thus paving the way for more efficient CO_2 conversion. A novel aspect of this dissertation is the exploration of dynamic pulsed potential systems. These modes allow better control over product selectivity by leveraging transient reaction environments. The insights gained from these studies not only improve our understanding of CO_2 electrolysis mechanisms but also provide practical guidelines for scaling up the technology.

The work concludes by presenting a roadmap for the development of scalable, sustainable CO_2 electroreduction systems. It emphasizes the importance of integrating experimental and computational approaches to tackle the multiscale challenges inherent in CO_2 electrolysis. The models developed here serve as powerful tools for predicting system performance, designing next-generation reactors, and accelerating the transition to industrial-scale applications. The findings contribute to the broader effort of developing technologies that enable a circular carbon economy, thereby addressing global energy and environmental challenges.

SAMENVATTING

De dringende noodzaak om klimaatverandering en hulpbronnenduurzaamheid aan te pakken, heeft de interesse gewekt in technologieën die effectief CO_2-emissies kunnen verminderen. Elektrochemische reductie van CO_2 is een van deze technologieën en biedt een route om CO_2 om te zetten in waardevolle chemicaliën en brandstoffen met behulp van hernieuwbare elektriciteit. Ondanks de belofte ervan, staan industriële toepassingen van elektrochemische CO_2-reductie voor aanzienlijke uitdagingen, waaronder beperkte massatransport, inefficiënte reactiekinetiek en een gebrekkige controle over de lokale reactieve omgeving aan het katalysatoroppervlak. Dit proefschrift pakt deze uitdagingen aan door middel van geavanceerde numerieke modellering.

Het onderzoek identificeert cruciale knelpunten, zoals de beperkte oplosbaarheid van CO_2 en lokale pH-schommelingen, en verkent strategieën om deze te overwinnen door middel van innovatieve elektrodesigns en operationele modi. Door het Poisson Nernst Planck raamwerk uit te breiden met eindige grootte-effecten en de Frumkin-gecorrigeerde Tafelrelatie, biedt dit werk een gedetailleerd inzicht in de elektrische dubbellaag, sterische effecten en solventdynamica nabij het katalysatoroppervlak in H-cel configuraties. Deze modellen zijn gevalideerd aan de hand van experimentele data, wat hun robuustheid en toepasbaarheid garandeert. Gasdiffusie-elektroden bieden aanzienlijke voordelen ten opzichte van traditionele H-cell systemen doordat ze directe CO_2-aanvoer naar de reactieve interface mogelijk maken. Deze systemen brengen echter nieuwe complexiteiten met zich mee, zoals de wisselwerking tussen poriënstructuur, ionentransport en lokale reactieomstandigheden. Door het gedrag van deze gasdiffusie-elektroden onder verschillende operationele omstandigheden te simuleren, identificeert het onderzoek optimale configuraties voor een ideale lokale reactieve omgeving, en effent het zo de weg naar efficiëntere CO_2-omzetting.

Een nieuw aspect van dit proefschrift is de verkenning van dynamische gepulste potentiaalmodi. Deze methoden bieden betere controle over productspecificiteit door gebruik te maken van transiënte reactieve omgevingen. De inzichten uit deze studies verbeteren niet alleen ons begrip van de mechanismen van CO_2-elektrolyse, maar bieden ook praktische richtlijnen voor het opschalen van de technologie.

Het werk besluit met het presenteren van een routekaart voor de ontwikkeling van schaalbare, duurzame CO_2-elektroreductiesystemen. Het benadrukt het belang van het integreren van experimentele en computationele benaderingen om de multischalige uitdagingen die inherent zijn aan CO_2-elektrolyse aan te pakken. De hier ontwikkelde modellen fungeren als krachtige hulpmiddelen om systeemprestaties te voorspellen, de volgende generatie reactoren te ontwerpen en de overgang naar industriële toepassingen te versnellen. De bevindingen leveren een bijdrage aan de bredere inspanning om technologieën te ontwikkelen die een circulaire koolstofeconomie mogelijk maken en zo de mondiale energie- en milieuproblemen aanpakken.

1

INTRODUCTION

1

The escalating concentration of carbon dioxide (CO_2) in the atmosphere is a pressing global concern, contributing significantly to climate change and environmental degradation [1]. The combustion of fossil fuels for energy production and industrial processes has led to unprecedented levels of CO_2 emissions, necessitating urgent action to mitigate their impact. Transitioning towards sustainable energy systems and developing technologies for carbon capture and utilization are critical steps in addressing this challenge. Among the technologies proposed to combat CO_2 emissions, the electrochemical reduction of CO_2 (CO_2ER) to value-added products is gaining a widespread popularity. This is primarily because electrochemical conversions not only provide a sustainable carbon neutral cycle (fig. 1.1), but are generally able to be carried out at room temperature and ambient pressures, thus making the technology industrially more feasible as well [2, 3].

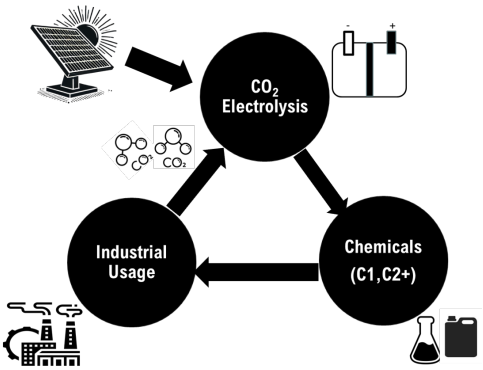

Figure 1.1: CO2ER based carbon neutral cycle.

1.1. THEORETICAL BACKGROUND

Fig. 1.2 depicts an H-cell configuration typical of an electrochemical process. Such a cell generally consists of a planar cathode, anode and an electrolyte. The electrochemical reaction is the exchange of electrons to or from one of the electrodes. The transport of both reactive and non-reactive species in such a cell happens in the electrolyte. For a CO_2ER process, CO_2 travels to the cathode side of the electrochemical cell and undergoes reduction (accepts electrons). These electrons are produced at the anode via the oxidation (releasing electrons) of the water molecules. Depending on the number of electrons transferred during the reduction of CO_2 and the type of catalyst used, a wide range of products can be obtained. Despite their utility in laboratory studies, H-cells face significant limitations that hinder their applicability for industrial-scale CO_2ER. Achieving cost-effective CO_2 electrolysis requires high current density (>200 mA·cm^{-2}) [4]. H-cell configuration with a planar electrode is severely limited in this regard, resulting in only tens of mA·cm^{-2}. This is caused by the low solubility of CO_2 in a water-based electrolyte. The low solubility of CO_2 in water limits the reactant supply to the catalytic surface. Furthermore, the operating conditions in H-cells, such as static electrolytes and low pressures, differ from those required for large-scale systems, limiting the relevance of H-cell results to industrial processes. One way to overcome this limitation is to simply

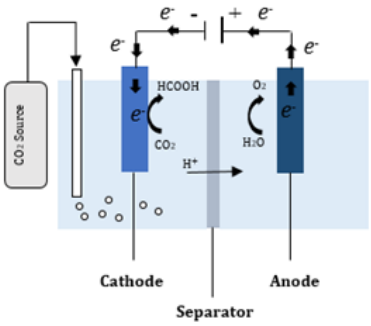

Figure 1.2: Schematic of a typical H-type CO_2ER cell.

increase the concentration of available CO_2. This can be done by either injecting CO_2 at high pressures [5, 6] or by using a non-aqueous solvent with high solubility for CO_2 [5, 7]. Finding a suitable solvent with adequate properties is generally considered more difficult of the two processes. Increasing the pressure of CO_2 gas enhances its solubility in the electrolyte and increases the driving force for diffusion, thereby improving the reactant concentration near the catalyst surface. Experiments conducted on a lab scale have shown that high pressures can result in high CO_2ER to format current density. A current density of 200 mA.cm^{-2} was attained at lab scale experiments using Hg, In and Pb catalysts [6]. Translating the lab-scale experiments into more of an industrial application has not seen the same levels of success. One study found that using Pb pellets in a fixed bed configuration only resulted in a current density of 1.5 mA.cm^{-2} towards formate. Another study using standard pallets resulted in a current density of 50 mA.cm−2 at 30 bar pressure. Clearly, there is a lack of understanding in terms of the physicochemical phenomenon underlying high pressure CO_2ER. Numerical simulation studies have been conducted to better understand the process [8]; however, they are often based on simplified reaction-diffusion (RD) models, resulting in several crucial phenomena being overlooked.

Another way to overcome the mass transport limitations of a planar electrode H-cell configuration is to use a gas diffusion electrode (GDE). Fig. 1.3 shows the schematic of a typical GDE half cell. This type of electrode is typically used in conjunction with a flowing electrolyte. Unlike traditional H-cell, where CO_2 must dissolve in the electrolyte and diffuse to the catalyst, GDEs introduce CO_2 gas directly to the catalytic interface. This significantly reduces the diffusion path length and overcomes the low solubility of CO_2 in aqueous electrolytes, enhancing reactant availability [9]. Most of the research efforts in GDEs are directed towards the optimal catalytic material [10]. Despite the advancements offered by GDEs, significant gaps remain in our understanding of the local reaction environment at the catalyst interface. The triple-phase boundary, where gas, liquid, and solid phases interact, is highly dynamic and influenced by various factors such as local pH gradients, ionic distributions, and reactant concentrations. For instance, studies have shown that pH at the catalytic surface can deviate significantly from bulk electrolyte values due to electrochemical reactions and ion transport phenomena, which directly impact product selectivity and reaction rates [11]. Similarly, the identity and the distribution

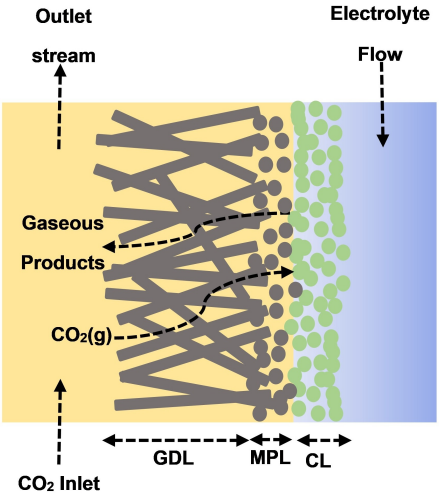

Figure 1.3: Schematic of a typical GDE based CO_2ER system.

of cations near the electrode surface influence the local reaction environment. Higher cationic concentration also leads to depletion or blocking of CO_2, further complicating the reaction environment [12]. However, capturing these intricate details experimentally is challenging. The nanometer-scale dimensions of GDE pores and the rapid timescales of ion and reactant dynamics make direct measurements exceedingly difficult. Traditional experimental techniques often provide bulk-averaged information, failing to resolve the spatial and temporal variations within the GDE structure. Moreover, the inaccessibility of the internal pores limits our ability to probe critical reaction zones where most of the catalytic activity occurs.

1.1.1. NUMERICAL MODELS

Both H-cells and GDE systems, present unique challenges related to mass transport, reaction kinetics, and local environment dynamics. Numerical modeling addresses these challenges by providing insights into critical processes that are often inaccessible through experimental methods. The core components of CO_2ER models include mechanisms for mass transport, electrochemical kinetics, and electric field distributions. Mass transport models focus on the movement of ions and reactants, such as dissolved CO_2, through the electrolyte and towards the catalytic surface. This involves diffusion, migration under electric fields, and convection in cases where flow systems are used. Electrochemical kinetics models describe the reaction rates of the various reduction pathways, incorporating the effects of applied potentials, surface intermediates, and competing side reactions like hydrogen evolution. The incorporation of electric field effects is essential for capturing the behavior of the Electric Double Layer (EDL), a region near the electrode surface where significant ionic and potential gradients exist, directly influencing the driving force for interfacial charge transfer reactions. In the context of a planar electrode, most models in this field generally neglect the influence of EDL. One such model based on the diffusion

process for transport and the homogeneous set of reactions, was developed by Gupta. et. al [13]. This model determined the influence of electrolyte concentration on the surface concentration of CO_2. Another such study, using a similar RD model, replicated the influence of high pressures on partial current densities [8]. Bohra. et. al [12] developed a Generalized Modified Poisson Nernst Planck (GMPNP) model for mass transport in an H-cell planar electrode configuration. It includes the influence of migration and steric limits for the solution species as well as an EDL region. However, the predicted concentration for CO_2 is extremely low. Furthermore, they did not explicitly include the kinetic model in their work. This necessitates further extension of the GMPNP model to incorporate a kinetic model and a correct estimate of CO_2 concentration.
Most of the modeling studies on GDEs rely on one-dimensional (1D) models, which often fail to account for the structural and spatial variations within the pores, leading to an incomplete representation of the local environment [9, 14, 15]. Studies that focus on 2D modeling often ignore the formation and thus the influence of EDL on concentration gradients and pH values near the pore walls[16]. Variations in ion concentrations and pH values within the EDL region directly influence the catalytic properties, affecting reaction rates and the selectivity of desired products [17, 18]. For instance, pH shifts at the reaction plane can alter intermediate stability and reaction pathways, leading to changes in product distribution of the desired products [12, 17, 18]. Bohra et. al. [11] developed a pore scale model that incorporates the formation of EDL within the nanopore, however; the predictive capabilities of their model were severely limited by the low potential range in which numerical stability was observed. As a result, there remains a critical need for robust modeling frameworks capable of resolving pore-scale dynamics across the full range of operating potentials to bridge the gap between fundamental research and industrial feasibility.

1.1.2. RESEARCH QUESTIONS AND OBJECTIVES

The primary goal of this research is to develop and apply advanced modeling frameworks to better understand the physicochemical phenomena involved in a CO_2ER process for both H-cell and GDE configurations and then leverage it to further optimize the process for higher selectivities and productivities. More specifically the questions focused on in this work are:

- How to accurately account for CO_2 concentration near the electrode surface and how do local conditions near the catalyst, such as EDL, steric effects, and ion distributions, impact efficiency and selectivity in CO_2ER?
- To what extent do high pressure systems overcome the mass transfer limitations in an H-cell based CO_2ER process?
- How do key parameters such as pore size, electrolyte concentration, and applied electrode potential influence the local reaction environment within the GDEs?
- What is the interplay between the concentration of cations and CO_2 molecules inside a GDE and how does the thickness of the catalyst layer (CL) influence this dynamic?

- Can time-dependent modeling under pulsed potential operations enhance our understanding of dynamic processes in CO_2ER and lead to improved performance over constant potential systems?

To address these questions, the objectives of this dissertation are:

- **Development of the FBV-SMPNP Model**: Formulate a modeling framework that accurately captures the physicochemical phenomena within the EDL, including ion steric effects, solvent molecule sizes, and Frumkin-corrected kinetics.
- **Test for High Pressure systems**: Adapting the model for a high pressure H-cell configuration and testing its validity by comparing the simulated results with experimental data in the literature.
- **Application to Nanoporous GDEs**: Adapting the modeling framework for CO_2ER process within nanopores of GDEs, analyzing how nanoscale confinement affects mass transport.
- **Investigation of Key Parameters**: Studying the influence of pore size, electrolyte concentration, and applied potential on the local reaction environment inside a GDE nanopore.
- **Extension to Pulsed Potential Operations**: Extending the model to pulsed potential operations, comparing the performance of GDE systems under pulsed and constant potential conditions.

1.1.3. STRUCTURE OF THE DISSERTATION

The remainder of this dissertation is organized as follows:

Chapter 2 details the development of the Frumkin–Butler–Volmer Size-Modified Poisson–Nernst–Planck (FBV-SMPNP) model, including theoretical foundations and computational methods. The model is adapted for a H-cell operating at high pressures. We use the model to predict the reaction environment close to the planar electrode and we validate the findings with experimental data

Chapter 3 details the complete methodology to adapt the mass transport model in the context of a nanoporous GDE, analyzing the effects of various parameters on the local reaction environment and identifying key geometric parameter to tweak it.

Chapter 4 extends the model to simulate pulsed potential operations, comparing the performance of GDE systems under pulsed and constant potentials, and discussing the influence of catalyst layer thickness.

Chapter 5 concludes the dissertation with a summary of findings, contributions to the field, and recommendations for future research.

Through this work, we aim to advance the understanding of the electrochemical reduction of CO_2ER, particularly within nanoporous GDEs and under dynamic operating conditions, contributing to the development of more efficient and scalable carbon utilization technologies.

REFERENCES

[1] Thomas Burdyny and Wilson A. Smith. “CO2 reduction on gas-diffusion electrodes and why catalytic performance must be assessed at commercially-relevant conditions”. In: *Energy Environ. Sci.* 12 (2019), p. 1442. DOI: DOI:10.1039/c8ee03134g.

[2] Xu Lu, Dennis Y.C. Leung, Huizhi Wang, Michael K.H. Leung, and Jin Xuan. “Electrochemical Reduction of Carbon Dioxide to Formic Acid”. In: *ChemElectroChem* 1 (5 2014), pp. 836–849. ISSN: 21960216. DOI: 10.1002/celc.201300206.

[3] Walter Leitner. “Carbon Dioxide as a Raw Material: The Synthesis of Formic Acid and Its Derivatives from CO2”. In: *Angewandte Chemie International Edition in English* 34 (20 1995), pp. 2207–2221. ISSN: 15213773. DOI: 10.1002/anie.199522071.

[4] Jing Lin, Shenglin Yan, Chunxiao Zhang, Qing Hu, and Zhenmin Cheng. “Electroreduction of CO_2 toward High Current Density”. In: *Processes* 10 (5 2022), p. 826. ISSN: 2227-9717. DOI: https://doi.org/10.3390/pr10050826. URL: https://www.mdpi.com/2227-9717/10/5/826.

[5] John-Paul Jones, G. K. Surya Prakash, and George A. Olah. “Electrochemical CO2 Reduction: Recent Advances and Current Trends”. In: *Israel Journal of Chemistry* 54 (10 2014), pp. 1451–1466. DOI: 10.1002/ijch.201400081. URL: https://doi.org/10.1002/ijch.201400081.

[6] Makoto Todoroki, Kohjiro Hara, Akihiko Kudo, and Tadayoshi Sakata. “Electrochemical reduction of high pressure CO_2 at Pb, Hg and In electrodes in an aqueous $KHCO_3$ solution”. In: *Journal of Electroanalytical Chemistry* 394 (1 1995), pp. 199–203. ISSN: 1572-6657. DOI: https://doi.org/10.1016/0022-0728(95)04010-L.

[7] Tomonori Saeki, Kazuhito Hashimoto, Naokazu Kimura, Koji Omata, and Akira Fujishima. “Electrochemical reduction of CO_2 with high current density in a CO2 + methanol medium at various metal electrodes”. In: *Journal of Electroanalytical Chemistry* 404 (2 1996), pp. 299–302. DOI: https://doi.org/10.1016/0022-0728(95)04374-8.

[8] Andrew R. T. Morrison, Vincent van Beusekom, Mahinder Ramdin, Leo J. P. van den Broeke, Thijs J. H. Vlugt, and Wiebren de Jong. “Modeling the Electrochemical Conversion of Carbon Dioxide to Formic Acid or Formate at Elevated Pressures”. In: *Journal of The Electrochemical Society* 166 (4 2019), E77–E86. ISSN: 0013-4651. DOI: 10.1149/2.0121904jes.

[9] Matthias Heßelmann, Berinike Clara Bräsel, Robert Gregor Keller, and Matthias Wessling. “Simulation-based guidance for improving CO_2 reduction on silver gas diffusion electrodes”. In: *Electrochemical Science Advances* 3 (1 Feb. 2023), p. 2100160. ISSN: 26985977. DOI: 10.1002/elsa.202100160.

[10] Karan Malik, Biju Mani Rajbongshi, and Anil Verma. “Syngas production from electrochemical reduction of CO_2 at high current density using oxide derived Zn/Cu nanocomposite”. In: *J. CO2 Util.* 33 (2019), pp. 311–319. DOI: https://doi.org/10.1016/j.jcou.2019.06.020..

[11] Divya Bohra, Jehanzeb H Chaudhry, Thomas Burdyny, Evgeny A Pidko, and Wilson A Smith. "Mass transport in catalytic pores of GDE-based CO_2 electroreduction systems". In: *ChemRxiv* (2020). DOI: https://doi.org/10.26434/chemrxiv.13073348.v1.

[12] Divya Bohra, Jehanzeb H. Chaudhry, Thomas, Evgeny A. Pidko, and Wilson A. Smith. "Modeling the electrical double layer to understand the reaction environment in a CO_2 electrocatalytic system". In: *Energy and Environmental Science* 12 (11 2019), pp. 3380–3389. ISSN: 17545706. DOI: 10.1039/c9ee02485a.

[13] N. Gupta, M. Gattrell, and B. MacDougall. "Calculation for the cathode surface concentrations in the electrochemical reduction of CO2 in KHCO3 solutions". In: *Journal of Applied Electrochemistry* 36 (2 2006), pp. 161–172. ISSN: 0021891X. DOI: 10.1007/s10800-005-9058-y.

[14] Lien-Chun Weng, Alexis T. Bell, and Adam Z. Weber. "Modeling gas-diffusion electrodes for CO_2 reduction". In: *Phys. Chem. Chem. Phys.* 20 (2018), pp. 16973–16984. DOI: https://doi.org/10.1039/C8CP01319E.

[15] Ying Chuan Tan, Kelvin Berm Lee, Hakhyeon Song, and Jihun Oh. "Modulating Local CO_2 Concentration as a General Strategy for Enhancing C C coupling in CO_2 Electroreduction". In: *Joule* 4 (2020), pp. 1104–1120. DOI: https://doi.org/10.1016/j.joule.2020.03.013.

[16] Joseph W. Blake, Vojtěch Konderla, Lorenz M. Baumgartner, David A. Vermaas, Johan T. Padding, and J. W. Haverkort. "Inhomogeneities in the Catholyte Channel Limit the Upscaling of CO_2 Flow Electrolysers". In: *ACS Sustainable Chemistry and Engineering* 11 (7 Feb. 2023), pp. 2840–2852. ISSN: 21680485. DOI: 10.1021/acssuschemeng.2c06129.

[17] Min Liu, Yuanjie Pang, Bo Zhang, Phil De Luna, Oleksandr Voznyy, Jixian Xu, Xueli Zheng, Cao Thang Dinh, Fengjia Fan, Changhong Cao, F. Pelayo García De Arquer, Tina Saberi Safaei, Adam Mepham, Anna Klinkova, Eugenia Kumacheva, Tobin Filleter, David Sinton, Shana O. Kelley, and Edward H. Sargent. "Enhanced electrocatalytic CO_2 reduction via field-induced reagent concentration". In: *Nature* 537 (7620 Aug. 2016), pp. 382–386. ISSN: 14764687. DOI: 10.1038/nature19060.

[18] Joaquin Resasco, Leanne D. Chen, Ezra Clark, Charlie Tsai, Christopher Hahn, Thomas F. Jaramillo, Karen Chan, and Alexis T. Bell. "Promoter Effects of Alkali Metal Cations on the Electrochemical Reduction of Carbon Dioxide". In: *Journal of the American Chemical Society* 139 (32 Aug. 2017), pp. 11277–11287. ISSN: 15205126. DOI: 10.1021/jacs.7b06765.

2

Modeling Kinetics and Transport in H-Cells

Electrochemical reduction of CO_2 *heavily depends on the reaction conditions found near the electrode surface. These local conditions are affected by phenomena such as electric double layer formation and steric effects of the solution species, which in turn impact the passage of* CO_2 *molecules to the catalytic surface. Most models for* CO_2 *reduction ignore these effects, leading to an incomplete understanding of the local electrode environment. In this work, we present a modeling approach consisting of a set of size-modified Poisson-Nernst-Planck equations and the Frumkin interpretation of Tafel kinetics. We introduce a modification to the steric effects inside the transport equations which results in more realistic concentration profiles. We also show how the modification lends the model numerical stability without adopting any separate stabilization technique. The model can replicate experimental current densities and Faradaic efficiencies till -1.5 vs SHE/V of applied electrode potential. We also show the utility of this approach for systems operating at elevated* CO_2 *pressures. Using Frumkin-corrected kinetics gels well with the theoretical understanding of the double layer. Hence, this work provides a sound mechanistic understanding of the* CO_2 *reduction process, from which new insights on key performance controlling parameters can be obtained.*

This chapter is based on the article: E. N. Butt, J. T. Padding, R. M. Hartkamp, "Size-modified Poisson–Nernst–Planck Approach for Modeling a Local Electrode Environment in CO_2 Electrolysis," *Sustainable Energy Fuels*, 2023, **7**, 144–154, DOI: 10.1039/D2SE01262F.

2.1. INTRODUCTION

Electrochemical Reduction of CO_2 (CO_2ER) has emerged as one of the most promising technologies to mitigate the excessive amounts of CO_2 in the atmosphere [1–3]. Renewable electricity can be used to power the conversion of CO_2 into different hydrocarbon molecules, which can then be utilized as fuels, energy storage media and chemicals for various industrial applications such as plastic production, preservatives and anti freezing. However, there are several challenges for such a technology to be fully functional under industrially relevant operating conditions. A lot of these challenges stem from the gap in knowledge about the exact physicochemical phenomena taking place in the immediate environment of the catalyst surface. This local environment of a CO_2ER catalyst is thought to be a vital ingredient determining the overall system performance [4].

The concentrations of the solution species found in the vicinity of the electrode end up affecting the properties of the catalyst and consequently the selectivities of the desired products [5, 6]. The build up of cations on the surface of the electrode results in the formation of an electric double layer (EDL), which affects the mass transport of reactive CO_2 as well as the driving force for the interfacial charge transfer reactions. Hence, it becomes essential to develop modeling approaches that are able to correctly resolve the mass transport as well the electric field within the EDL, see Table 2.1. Most techniques used to model the CO_2ER process ignore these EDL effects and are insufficient in their theoretical implementation. Modeling techniques based on atomistic calculations have been used a lot for modeling double layer effects [7, 8], but atomistic simulations may not be the preferred approach to model reactions, capture the role of pH, and cover the range of length scales relevant to CO_2ER. Continuum-based methods offer a more practical approach to model CO_2ER, where the underlying physics is largely included in a mean-field way.

Out of the many approaches to model CO_2ER transport, one of the most commonly used, is the reaction-diffusion model [9]. This type of approach is based on the charge neutrality assumption and hence is not suitable for modeling mass transport inside the EDL [10–13]. Another approach, rooted in dilute solution theory, uses a set of Poisson-Nernst-Planck (PNP) equations [14]. This model specifically considers the migration of ions towards the catalyst surface. However, steric effects due to the finite size of solution species, are usually neglected. As a result, unphysically high ionic concentrations are typically predicted in the EDL region [15–17].

Steric effects are predicted to play a significant role in dictating the local reaction conditions of an electrode [15, 16, 18]. More recently, a set of generalized modified PNP (GMPNP) equations was adopted in the context of CO_2ER by Bohra et. al. [17]. This model highlighted the importance of steric effects in the EDL region, as it corrected for the high ionic concentrations predicted by the classical PNP models. This GMPNP modeling approach predicts extremely low CO_2 concentration at the reaction plane for cathodic potentials of -0.9 vs standard hydrogen electrode (SHE)/V for an Ag(111) catalyst surface. These low concentrations are a direct result of the introduction of steric effects leading to increased mass transfer limitations for CO_2. However, it is known from experimental studies that CO_2ER is not completely mass transfer limited (reaching limiting current density) at these electrode potentials [19], suggesting that there is an overestimation of steric effects experienced by a CO_2 molecule in the GMPNP modeling approach. Because

Table 2.1: Different modeling approaches for the coupling of electrode reactions and mass transport to and from an electrode surface with varying levels of complexity: reaction-diffusion (RD), Poisson-Nernst-Planck (PNP), Generalized Modified Poisson-Nernst-Planck (GMPNP), and Frumkin-Butler-Volmer Size-Modified Poisson-Nernst-Planck (FBV-SMPNP) models

Model	Diffusion	Migration	Steric Effects	Solvent Steric Effect	Frumkin Correction
RD[9]	Y	N	N	N	N
PNP	Y	Y	N	N	N
GMPNP[17]	Y	Y	Y	N	N
FBV-SMPNP	Y	Y	Y	Y	Y

overcoming mass transfer limitations of CO_2 is one of the primary challenges in the optimal design of a CO_2ER system, it is essential to have models that are able to predict the CO_2 concentration in the EDL region accurately. In this work, we propose a set of size-modified PNP equations (SMPNP) for modeling the mass transport in a CO_2ER system, and we couple this transport model with Frumkin corrected Tafel relations. Overall, the FBV-SMPNP model provides a unique methodology to better approximate the local electrode environment in a computationally tractable manner and can be easily implemented for a wide range of applications including the evaluation of optimal conditions under which maximum Faradaic efficiencies can be attained. The SMPNP equations extend the GMPNP approach by explicitly including the influence of solvent (water) molecule size on the chemical potential of each solution species. The origin of this modification is rooted in a lattice model for the free energy and has been previously utilized in biomolecular systems [20, 21]. Another factor to consider is that most CO_2ER models include the reaction rates as either fixed input to the system [9, 17, 22] or use some formulation of Butler-Volmer (BV) or Tafel relations with experimentally fixed kinetics parameters to predict reaction rates [10, 23]. The latter approach is often used to validate the models against experimental data. This is not possible if the reaction rates are fixed input to the system. Another advantage of explicitly considering kinetics inside the model is that it allows for the prediction of current densities at elevated pressures by fixing the kinetics parameters at just one experimental pressure value [23]. Working at elevated pressures allows one to offset the CO_2 solubility limitations which can be a technological solution to attaining industrially relevant operating current densities. Morrison et. al.[23] used a Tafel relation to predict limiting current densities for a CO_2 to $HCOO^-$ system at elevated pressures. However, a standard Tafel kinetics relation does not explicitly take into account the influence of surface charging on reactions that are determined by the rate of interfacial charge transfer, because it assumes the driving force for the reaction to be the potential difference between the electrode and the bulk of electrolyte. However, in the presence of an EDL, the driving force for an interfacial charge transfer reaction comes from the potential drop across the immobile Stern layer [24–26]. This is the so-called Frumkin correction to Butler-Volmer kinetics (FBV)[25, 27]. The addition of this correction incorporates double layer behavior in the form of altered electrode rate constants. Considering this type of kinetics description is also necessary because the local concentrations in the EDL affect the local electric field and consequently the driving force for the interfacial charge transfer reactions. In this study, we use the complete set of FBV-SMPNP equations to obtain the concentration profiles for all components in the solution near the electrode

surface. We present comparisons for the concentration profiles using different modeling approaches summarized in Table (2.1) and highlight the advantages of using an SMPNP type mass transport formulation. We focus on the concentration of CO_2 in the EDL, which was previously a bottleneck in the GMPNP model. We present a comparison between both models based on the estimated concentrations and highlight the significance of considering the modification of steric effects as presented in the SMPNP equations. The model is then validated by comparing the partial current densities of reactions that are sensitive to CO_2 concentration with experimental data. Finally, we make a case for using the Frumkin-corrected kinetics approach for its merits in predicting the hydrogen evolution current densities with great accuracy and for its theoretical consistency with the EDL formulation.

2.2. REACTION AND MASS TRANSPORT MODELING

The electrochemical model is developed for a 1-D simulation domain stretching from the bulk of the electrolyte to the cathode. Only the cathodic side of the electrochemical cell is considered because the CO_2ER reactions occurring at the cathode and the EDL are not influenced by the anodic section. The model also takes into account the so-called Nernst diffusion layer, sandwiched between the bulk electrolyte region and the EDL. It represents the charge-neutral layer of electrolyte where the concentrations of the species deviate from the bulk value because of the limited diffusivity of the solution species. Fig. 2.1 represents the complete simulation domain considered in this work. This study is based on potassium bicarbonate ($KHCO_3$) electrolyte solution, which is one of the most commonly used electrolytes for CO_2ER [28]. The electrode material is assumed to be indium (In). The main product of CO_2ER is $HCOO^-$. The electrolyte solution is saturated with CO_2 at high pressures. The following homogeneous carbonate equilibrium reactions occur in the electrolyte:

$$HCO_3^- + OH^- \underset{k_{-1}}{\overset{k_1}{\rightleftharpoons}} CO_3^{2-} + H_2O \tag{2.1}$$

$$CO_2 + OH^- \underset{k_{-2}}{\overset{k_2}{\rightleftharpoons}} HCO_3^- \tag{2.2}$$

$$H_2O \underset{k_{-3}}{\overset{k_3}{\rightleftharpoons}} H^+ + OH^- \tag{2.3}$$

k_n and k_{-n} represent the forward and backward rate constants, respectively. Values for these rate constants can be found in Appendix D (Table D.2). The following solution species are considered in the model: CO_2, OH^-, HCO_3^-, K^+, CO_3^{2-} and H^+. The bulk concentration of K^+ depends on the electrolyte concentration, which is taken as 0.5 M in this work. The concentration for all other components inside the bulk is calculated by solving the rate equations (2.1-2.3), coupled with the Sechenov equation [17, 29, 30]. The Sechenov equation takes into account the effect of ionic concentration on the solubility of CO_2. The chemisorbed form of CO_2, H_2CO_3, is present in extremely low amount as compared to CO_2 [31] and hence its influence on equilibrium reactions is neglected. The detailed methodology to calculate bulk concentrations and the values of these calculated

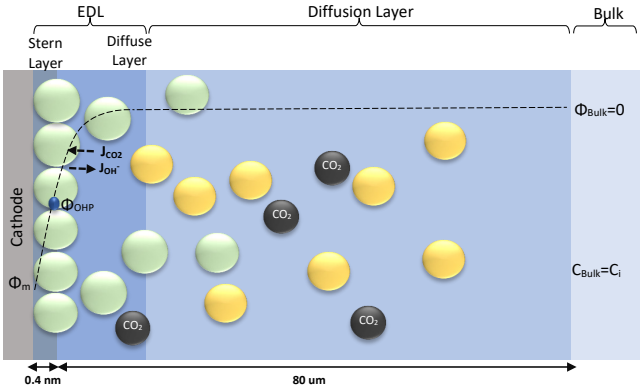

Figure 2.1: Schematic of mass transport regions for a CO_2ER process. Stern layer composed mainly of K^+. The plane of closest approach for the solution species is the outer Helmholtz plane (OHP).

bulk concentrations are given in Appendix D. The electrochemical model solves for the mass transport of solution species within the diffusion layer and EDL region. The SMPNP equations are used to model the transport:

$$\frac{\partial C_i}{\partial t} = \nabla \cdot \left[D_i \nabla C_i + \frac{D_i C_i z_i \mathrm{F}}{\mathrm{R_G} T} \nabla \Phi + D_i C_i \left(\frac{\beta_i \mathrm{N_A} \sum_{j=1}^{n} a_j^3 \nabla C_j}{1 - \mathrm{N_A} \sum_{j=1}^{n} a_j^3 C_j} \right) \right] + \sum_s R_i \tag{2.4}$$

Here C_i is the concentration of species i in the solution. R_i is the rate of formation for species i in the homogeneous reactions Eqs. (2.1-2.3). D_i and z_i represent the diffusivity and charge of species i, a_j is the effective solvated size of the ionic species. For j=CO_2 a_j represents the size of the unhydrated CO_2 molecule. Φ is the local electric potential, F is the Faraday constant, $\mathrm{R_G}$ is the gas constant, T is the absolute temperature and $\mathrm{N_A}$ is Avogadro's number. Values of diffusivities and diameters of all solution species can be found in Appendix D. The terms on the right hand side of Eq. (2.4) inside the divergence operator collectively represent the molar flux $\vec{J}_i$ of species i. The first two contributions inside the flux term represent diffusion and migration terms, respectively. The third contribution comes from the excluded volume/steric effect. The consideration of the size effects through the excluded volume term allows us to overcome the limitations presented in a dilute solution theory based model [17, 18, 32–34]. One of the key features of the SMPNP approach presented in this study is the inclusion of the β_i factor in the excluded volume term given by:

$$\beta_i = \frac{a_i^3}{a_0^3} \tag{2.5}$$

here a_0 is the effective size of solvent species H_2O. β_i serves as a magnification factor for the excluded volume effects felt by species i inside the solution. The $\beta_i \ll 1$ for species with sizes much smaller than a water molecule and $\beta_i \gg 1$ for species with sizes much larger than a water molecule. This factor is often neglected even in the models that do take into account the finite size behavior of solution species [17, 34]. β_i factor results from

a lattice model for the partition function (and consequently free energy) of a mixture of large and small species that cannot occupy the same space [20, 21]. Since water molecules are the majority species, their influence on the partition function will also be the largest. It is also worth pointing out that the β_i value is very sensitive to the sizes of each species. Often, these sizes are not well defined in the literature and one must rely on parametric fitting. Later in this study, we will show that the inclusion of this factor becomes necessary for a model that aims to resolve the EDL while also reproducing the experimental current densities. Eq. (2.4) is to be solved concurrently with the Poisson equation:

$$\nabla \cdot (\epsilon_0 \epsilon_r \nabla \Phi) = -\mathrm{F} \sum_{i=1}^{n} z_i C_i \tag{2.6}$$

here ϵ_0 and ϵ_r represent the vacuum permittivity and the relative permittivity of the aqueous electrolyte. ϵ_r is assumed to vary with the local concentration of the cationic species (K^+, H^+) [17, 35, 36] and is evaluated at every time step using:

$$\epsilon_r = \epsilon_r^0 \left[\frac{M_{\mathrm{H_2O}} - \sum_i^{n_{cat}} w_i C_i}{M_{\mathrm{H_2O}}} \right] + \epsilon_r^{min} \left[\frac{\sum_i^{n_{cat}} w_i C_i}{M_{\mathrm{H_2O}}} \right] \tag{2.7}$$

ϵ_r^0 and $M_{\mathrm{H_2O}}$ are the relative permittivity and molarity of water at room temperature, taken as 80.1 and 55 M, respectively. w_i is the number of water molecules bound to the cation (w_{K^+}=4, w_{H^+}=10 [36]). ϵ_r^{min} is the dielectric constant of water at the dielectric saturation condition and its value is taken as 6. Eq. (2.7) shows how the bulk and cation bound water molecules contribute to the relative permittivity [17]. The EDL is based on Gouy-Chapman-Stern theory, which predicts an immobile layer of tightly bound cations at the surface of the electrode, making up the Stern layer as shown in Fig. 2.1. The width of the Stern layer is assumed to be slightly larger than the radius of a solvated K^+ ion (≈0.4 nm) [17]. Because of the presence of a Stern layer, the plane of closest approach for the solution species is the outer Helmholtz plane (OHP). The chosen catalyst surface (indium), primarily promotes CO_2ER to $HCOO^-$. This material is chosen to compare the current density results obtained from the model with experimental data available in the literature. The following electrochemical reactions occur at the indium electrode:

$$\mathrm{CO_2(aq) + H_2O + 2\,e^- \rightleftharpoons HCOO^- + OH^-} \tag{2.8}$$

$$\mathrm{CO_2(aq) + H_2O + 2\,e^- \rightleftharpoons CO\,(g) + 2\,OH^-} \tag{2.9}$$

$$\mathrm{2\,H_2O + 2\,e^- \rightleftharpoons H_2\,(g) + 2\,OH^-} \tag{2.10}$$

It is worth mentioning that Eqs.(2.8-2.10) represent the overall stoichiometric reaction and not the elementary electron transfer reactions. CO_2 reduction reactions are complex multistep processes. In this work, the reaction mechanism is based on the work by Feaster et. al. [37]. In the first step of CO_2 reduction, one electron is transferred to form a radical anion $CO_2^{\bullet -}$. The radical anion may or may not be strongly adsorbed to the surface of the catalyst depending on the type of metal and the eventual product being produced [38]. For $HCOO^-$ forming metals the CO_2 binding occurs via the oxygen atoms resulting in intermediate *OCHO and for CO forming metals via the carbon atom

resulting in intermediate *COOH [37]. Regardless of the intermediate species, the final step involves the transfer of the second electron to the reactive intermediate to form the products ($HCOO^-$, CO). The rate-determining step (RDS) is assumed to be the initial electron transfer to CO_2 to form the radical anion [39, 40]. It is assumed that the adsorbed intermediate species do not influence or restrict CO_2 to bind with the surface of the catalyst. This assumption has merit for catalyst surfaces such as indium, where at any time only small amounts of intermediate adsorbed species were found on the metal [38, 41]. Furthermore, experimental studies done at increasingly high CO_2 pressures suggest an almost linear increase in limiting current densities, suggesting that even at high CO_2 concentration, the adsorbed intermediates have negligible influence on the reaction rate[28]. The flux of the species involved in the charge transfer reactions at the OHP (defined in our model as x=0) and time t is given by:

$$J_{i,(\mathrm{OHP},\,t)} = \sum_p \frac{\nu_{i,p}\, j_p}{n_p \mathrm{F}} \qquad i = \mathrm{CO_2},\ \mathrm{OH^-} \tag{2.11}$$

All other solution species are not taking part in charge transfer reactions, hence:

$$J_{i,(\mathrm{OHP},\,t)} = 0 \qquad i = {\mathrm{CO_3}}^{2-},\ \mathrm{K^+},\ {\mathrm{HCO_3}}^-,\ \mathrm{H^+} \tag{2.12}$$

The product species CO and H_2 have very low solubility in water at room temperature hence it is assumed that they bubble out instantly from the system. $HCOO^-$ is assumed to not influence the overall transport of other solution species because it does not take part in homogeneous reactions [23] and was found only in small amounts inside the system. $\nu_{i,p}$ is the stoichiometric coefficient of species i in reaction p (Eqs. (2.8-2.10)). n_p is the number of overall electrons transferred in reaction p. j_p is the current density of the RDS involved in the overall reaction p. In many models, j_p is assumed and given as input to the model alongside the applied electrode potential E. In reality, j_p is influenced by local electric fields and the EDL environment until a steady state is reached. Therefore, in this work, only the electrode potential E is given as input to the model, and j_p is evaluated at every time step, which in turn helps to inform the electrode flux boundary condition via Eq. 2.11. It is also worth mentioning that due to sharp concentration gradients experienced near the surface of the electrode, we can not assume local equilibria as often done in such systems. Because there is practical interest in relatively high cathodic overpotentials, the backward reactions are ignored [23] and the following Frumkin-corrected Tafel equation is used to evaluate current densities [24, 25, 42]:

$$j_p = j_p^* \frac{C_{\mathrm{CO_2OHP},\,t}}{C_{\mathrm{CO_2Bulk}}} \exp\left[\frac{-a_p^* \mathrm{F}}{\mathrm{R_G}\,T}\left(E - E_{eq,p} - \Phi_{\mathrm{OHP},\,t}\right)\right] \tag{2.13}$$

$C_{\mathrm{CO_2OHP},\,t}$ is the concentration of CO_2 at the OHP and time t. $C_{\mathrm{CO_2Bulk}}$ is the concentration of CO_2 in bulk electrolyte. j_p^* and a_p^* represent an effective exchange current density and charge transfer coefficient, respectively, and their values are calculated from Tafel plot data taken from the literature [28]. $E_{eq,p}$ is the reference equilibrium potential for a reaction p according to standard potentials at pH=7 (Table D.9 in Appendix D). $\Phi_{\mathrm{OHP},\,t}$ is the electric potential at the reaction plane (OHP) and time t, modeled as:

$$\Phi_{\mathrm{OHP},\,t} = E - L_{\mathrm{Stern}} \left(\frac{\partial \Phi}{\partial x} \right)_{\mathrm{OHP},\,t} \tag{2.14}$$

Eq. (2.14) is based on the idea that the Stern layer acts as a uniform dielectric film leading to a linear variation of the electric potential from the surface of the metal electrode to the OHP, with a continuous electric field at the OHP [27, 43]. Since the main reactant for the hydrogen evolution reaction in Eq. (2.10) is H_2O, there are no mass transfer limitations and the current density for HER becomes:

$$j_p = j_p^* \exp\left[\frac{-a_p^* \mathrm{F}}{\mathrm{R_G} T} \left(E - E_{eq,p} - \Phi_{\mathrm{OHP},\,t} \right) \right] \tag{2.15}$$

The significance of the Frumkin-corrected kinetics expressions Eqs. (2.13-2.15) is that the driving force for the elementary electron transfer is the potential difference between the metal electrode and the OHP. This correction accounts for the EDL by taking into consideration the variation of the apparent rate constants as a result of changing electric fields and local reaction environment [44, 45]. The concentration of the reactive species involved in the RDS is also evaluated at the OHP, which is the reaction plane in our model. This is in contrast to the standard BV formulation where the driving force is taken to be the potential difference between the metal electrode and the bulk region of the electrolyte. Furthermore, a standard BV formulation for kinetics is inconsistent with the Gouy-Chapman-Stern formulation of the EDL, as it ignores the influence of a diffuse layer. All potential values in the simulations are referenced with respect to the potential at the point of zero charge (PZC). The PZC value depends heavily on the material properties of the electrode as well as the electrolyte environment [46]. Since we aim to recreate the experimental conditions, the value of PZC is fitted to data available in the literature [28]. Fig. 2.1 details the boundary conditions used in the model. Initially, all concentrations will be at bulk values and the electric potential value will be 0 throughout the simulation domain. The length of the diffusion layer is determined to be 80 μm based on the diffusion-limited current for such a system[23, 28]. Dirichlet boundary conditions for concentrations and potential are imposed on the right side of the simulation domain. At x=0 (OHP), Neumann boundary conditions for the flux of the solution species are applied using Eqs. (2.11-2.12). Eq. (2.14) is used as a Robin type boundary condition for the electric potential value at the OHP. Both Neumann and Robin boundary conditions are evaluated at every time step, making the model also suitable for transient and dynamic applications. The finite element package FEniCS is used to solve a weak formulation of the non-linear FBV-SMPNP equations. The complete set of equations (FBV Eqs. (2.11-2.15) and SMPNP Eqs. (2.4-2.7)) are solved self-consistently using a Newton solver. Spatial and temporal discretization is done using a finite element method and backward Euler scheme, respectively. The FBV-SMPNP model becomes less stable with increasing applied electrode potential. This is caused by the vastly different lengths and time scales required to model the different physicochemical processes. Hence the time step used in the first 7 milliseconds is 1x10^{-7} s and after that, a time step of 1x10^{-3} s is used until steady-state is reached. Similarly, a variable mesh spacing is used in the simulations, with a finer mesh near the OHP and a coarser mesh in the diffusion layer.

2.3. RESULTS

In this section, we first present the resolved concentration profiles for various solution species in the vicinity of the electrode as a function of multiple applied electrode potentials (Fig. 2.2). The results are mainly centered around the first few nanometers because this is the region where most of the uncertainty with regard to concentrations of solution species exists. We show the effect of including the size ratio β_i on the overall mass transfer. This effect is then validated against experimental partial current density values found in the literature (Fig. 2.4). The predictive power of the FBV-SMPNP model is tested by comparing partial current densities at elevated pressures of 40 bar (Fig. 2.5). We then show that using the FBV type kinetics approach gives better estimates of HER partial current densities as compared to a standard BV-based kinetics model (Fig. 2.7).

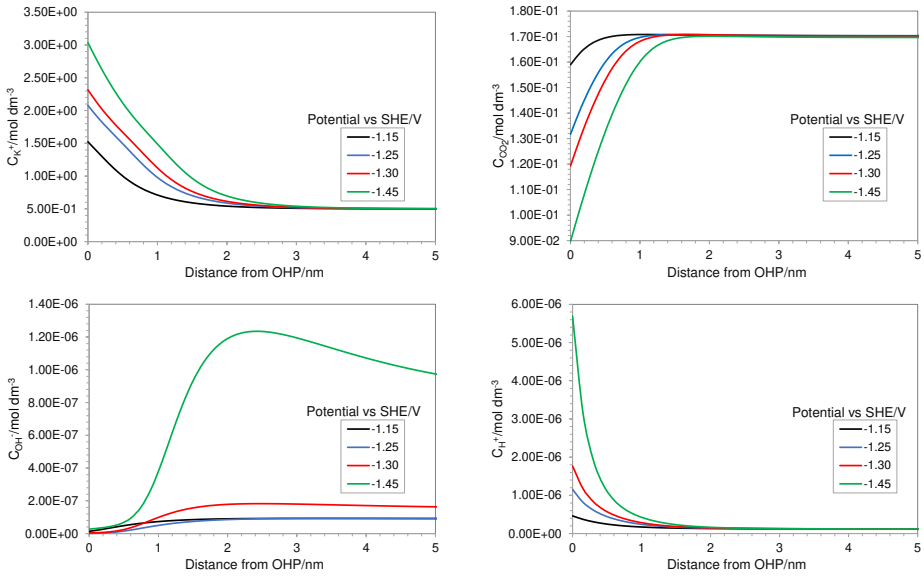

Figure 2.2: Concentration profiles in the EDL region at varying applied electrode potentials for a 0.5 M $KHCO_3$ solution at 5 bar CO_2 pressure.

Fig. 2.2a depicts the build up of the cation K^+ in the EDL region at increasing electrode potentials. Because the size of the solvated cations is explicitly considered in the model, there will be a limit on the maximum concentration of K^+ ions at the OHP. Once this steric limit is reached, the thickness of the EDL profile increases. This results in the EDL behaving as a condensed layer of cations, rather than a diffuse layer. This in turn has implications for the CO_2 reduction reaction, because now CO_2 has to diffuse through a thicker dense layer of counter ions, leading to reduced access to the catalyst surface and, consequently, decrease in maximum attainable current density. Fig. 2.2b shows the decreasing CO_2 concentration as the electrode potential is increased. This is correlated with the increasing K^+ concentration and suggests that the rate of mass transfer is limiting the reaction. Fig. 2.2c depicts an almost complete depletion of OH^- ions at the OHP. This is due to the negative charge associated with an OH^- ion, resulting in increasing

electrostatic repulsion near the OHP. This repulsion is taken into account by the migration term in Eq. (2.4). Similarly, an increase in the positively charged H^+ ion concentration is observed with increasing electrode potential (Fig. 2.2d). The combined effect of OH^- repulsion and H^+ attraction leads to a significant drop in the local pH values. It is worth pointing out that not considering the volume exclusion effect will result in an unrealistically low pH [17]. This is because in the absence of the volume exclusion term in Eq. (2.4), point-like species are assumed with no steric limits. For point-like species the concentration of H^+ at the OHP would be unrealistically high, whereas considering the size of hydrated H^+ ions puts a steric limit to the maximum attainable concentration. It is also worth noting that the hydrated size of a H^+ ion is considered since free protons generally do not exist in solution due to their lack of an electron cloud. Since pH is one of the more vital performance controlling parameters experimentally [30], it becomes essential to consider size effects when modeling a CO_2 reduction system. The general trend for concentration profiles as a function of applied potential is in agreement with the trends found by Bohra et. al. [17] using the GMPNP model but for different operating conditions of CO_2 pressure, applied electrode potential and electrolyte concentration.
Fig. 2.3a shows the concentration profiles of K^+ as predicted by different models at the same operating conditions. Each model differs in the level of complexity and physico-chemical phenomena included in them (see Table 2.1). A reaction-diffusion type model (RD) predicts negligible cation concentration at the OHP as compared to other modeling approaches. This is because such an approach does not explicitly take into account the migration due to the assumption of charge neutrality. Consequently, such an approach might be only suitable for analyzing the mass transport behavior in the diffusion layer

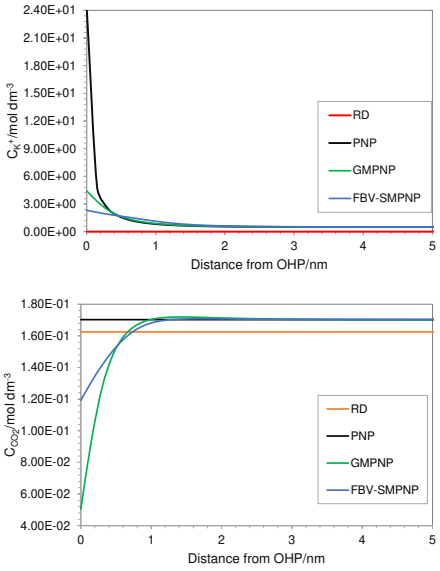

Figure 2.3: Comparison of concentration profiles in EDL using different approaches at applied electrode potential of -1.3 vs SHE/V for a 0.5 M $KHCO_3$ solution at 5 bar CO_2 pressure.

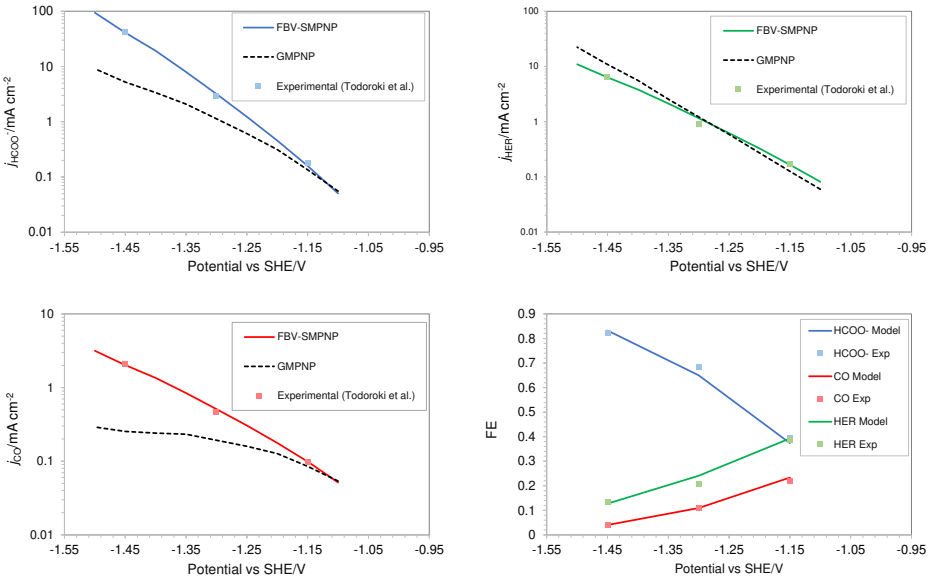

Figure 2.4: Comparison of partial current densities with experimental values using GMPNP and FBV-SMPNP methods (a-c). Comparison between Faradaic efficiencies obtained from FBV-SMPNP model and experiments (d). The system is 0.5 M $KHCO_3$ solution at 5 bar CO_2 pressure based on an In catalyst. Experimental values are taken from the literature [28].

and for highly concentrated solutions where the entire double layer charge is carried inside the Stern layer, giving us a Helmholtz description of the EDL.
The concentration of K^+ predicted by the PNP model is extremely high (24 mol dm^{-3}) at the OHP due to the absence of volume exclusion effects (dilute solution theory). The GMPNP model predicts lower concentration at the OHP owing to the excluded volume effects. As a result, a somewhat realistic concentration of 4.5 mol dm^{-3} can be seen. However, using the FBV-SMPNP approach, the observed concentration is approximately 50% lower than that predicted by GMPNP. This is due to the consideration of the β_i ratio (a_i^3/a_0^3) in Eq. (2.4). Larger species encounter more steric repulsion as compared to smaller ones. In the GMPNP model, the underlying assumption is that β_i is essentially 1 for all species. In the case of K^+ transport, this would mean that hydrated K^+ ions and H_2O molecules have a similar size. The FBV-SMPNP model corrects this assumption using the estimated sizes in Appendix d (Table D.5). As a result, the β_i ratio is much larger than 1 for K^+ ions, hence the steric effects on the cation are also enhanced, which can be clearly seen in Fig. 2.3a. Mathematically, the β factor acts as a hard limit on the maximum attainable concentration of K^+ ions. Since the build up of cations in the vicinity of the electrode influences both the electric field strength and access to the catalyst for CO_2, using the correct formulation for volume exclusion effects becomes essential. The study conducted by Bohra et. al. [17] using the GMPNP model, observed almost no CO_2 concentration at the OHP beyond an electrode potential of -0.9 vs SHE/V for a 1 bar CO_2 pressure system at Ag(111) surface. As the authors noted, this is highly unrealistic because

it is known experimentally that CO_2ER has not reached the limiting current density at this potential. Applying the GMPNP approach to our system results in similarly lower CO_2 concentrations (Fig. 2.3b), which are also inconsistent with the experimental current density data [28], suggesting an underestimation of CO_2 concentration at the reaction plane. In contrast, the FBV-SMPNP model estimates a much higher concentration for CO_2 at the OHP (2.3b). The size of the unhydrated CO_2 molecule is smaller than all other hydrated solution species including K^+ [47], and hence the steric effect experienced by a CO_2 molecule is small relative to the other solution species. This in turn gives CO_2 more space to diffuse towards the OHP. For both RD and PNP models, the concentration of CO_2 remains close to the bulk values. This is because of the point species assumption in both RD and PNP approaches. The slightly lower concentration of CO_2 in the RD model as compared to PNP is because, in the absence of migration, the RD model predicts a relatively more basic environment near the electrode surface, leading to the promotion of the CO_3^{2-} forming reaction (2.1). To validate the effect of the β_i ratio and the resulting CO_2 concentration predicted at the OHP, we compare the partial current density data predicted by both FBV-SMPNP and GMPNP models with the experimental data from the literature [28].

The simulations were performed assuming an indium catalyst and 5 bar of CO_2 pressure, matching the experimental operating conditions. CO_2 reduction on an In catalyst results in the formation of $HCOO^-$ and trace amounts of CO. The first step of the reduction process, namely the interfacial charge transfer reaction to form the intermediate radical anion (the rate determining step) depends on the CO_2 concentration at the reaction plane (OHP) [48]. Hence, a good match with experimental current densities would suggest an accurate estimation of CO_2 concentration. The predicted $HCOO^-$ formation current density in Fig. 2.4a and the CO formation current density in Fig. 2.4c, using the FBV-SMPNP approach are in much better agreement with the experimental partial current densities as than a GMPNP model within a range of applied electrode potentials (upto ≈ -1.5 vs SHE/V). The FBV-SMPNP model requires the applied electrode potential and the fitted kinetics parameters as input to solve for the current densities using dynamic FBV kinetics as described by Eq. (2.13). This is different from models such as GMPNP [17] and RD [9], both of which take current density and applied electrode potential at a specific catalyst surface as input. The FBV-SMPNP approach is then used

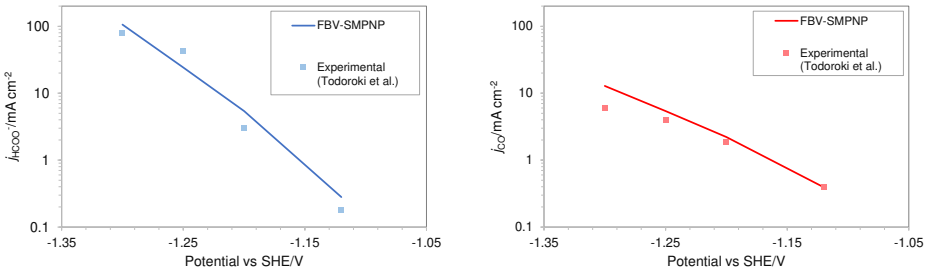

Figure 2.5: Comparison of partial current densities for CO_2 reduction in a 0.5 M $KHCO_3$ solution at 40 bar CO_2 pressure based on an In catalyst. Experimental values used are taken from the literature [28].

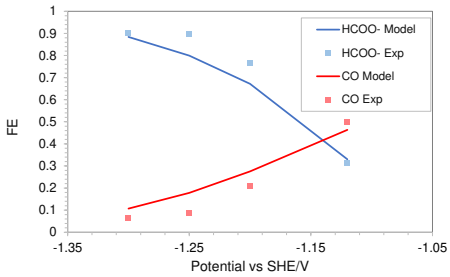

Figure 2.6: Comparison of Faradaic efficiencies of CO_2 based reduction products in a 0.5 M $KHCO_3$ solution at 40 bar CO_2 pressure based on an In catalyst. Experimental values used are taken from literature [28].

to analyze the current-voltage behavior and the resulting selectivities of all three electro reduction products at elevated pressures of 5 (Fig. 2.4) and 40 bar (Figs. 2.5 and 2.7). At 5 bar pressure, within the applied potential range, $HCOO^-$ remains the dominant product with the highest Faradaic efficiency of about 0.84 at -1.45 vs SHE/V (Fig. 2.4d). Increasing the pressure of CO_2 to 40 bar leads to a significant increase in the partial current density of $HCOO^-$ (Fig. 2.5a) with respect to the current density at 5 bar (Fig. 2.4a). Similarly, the partial current density of CO also increases with increasing CO_2 pressure (Fig. 2.5b vs 2.4c). This is due to the increased amount of CO_2 available in the system. The match with experimental Faradic efficiencies remains good even at high pressure of 40 bar as seen in Fig. 2.6. The current density data for $HCOO^-$ and CO formation will eventually start to diverge from the experimental values at higher applied electrode potentials. The experimental results in the literature suggest a faster consumption of CO_2 at electrode potentials above -1.5 vs SHE/V, compared to what is predicted by the FBV-SMPNP model. This leads to divergence between the predicted and experimental limiting current density values. This could be because the specific adsorption of intermediate species plays an increasingly important role in determining the rate of reaction (current densities) at high electrode potentials. In our model, this effect is not explicitly included. For further discussion see Section(4). Nevertheless, the match between experimental and predicted partial current densities remains extremely good upto -1.5 vs SHE/V for all 3 products. The predictive power of the FBV-SMPNP model for the hydrogen evolution reaction is very good at both pressures (Fig. 2.4b and 2.7). HER varies directly with applied electrode potential and has no dependence on CO_2 concentration at the OHP, hence the limitations found in the prediction of partial current densities for $HCOO^-$ and CO are practically non-existent. Fig. 2.7 shows the comparison of HER partial current density predicted by the FBV-SMPNP model, the RD model and experimental values found in literature [28]. Both models are compared to the same experimental study so that the difference in the predicted values can be associated with the difference in modeling methodology rather than possible variation in the experimental setup. A RD model that is based on the standard Tafel kinetics equations massively overpredicts the partial current density of HER. This is especially true at high applied electrode potentials. The partial current density at -1.86 vs SHE/V using RD type model is approximately 400 mA cm^{-2}, almost three times the actual experimental current density. Compared to the RD system, the

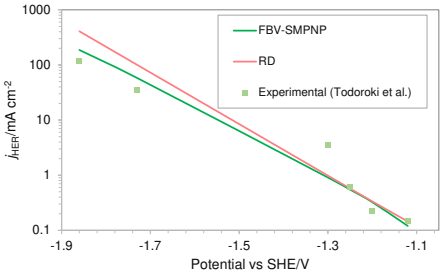

Figure 2.7: Comparison of HER partial current densities for CO_2 reduction in a 0.5 M $KHCO_3$ solution at 40 bar CO_2 pressure based on an In catalyst. Experimental values used are taken from literature [28].

FBV-SMPNP model performs exceptionally well in predicting the partial current densities of HER. This is because the Tafel relation in a RD model does not explicitly take into account the influence of varying OHP potentials on the rate constants. This effect is included in our model by employing the Frumkin correction within a Tafel relation.
It should be noted that a RD model based on the traditional Butler-Volmer relations can be interpreted as a theoretical limiting case of the FBV-SMPNP model. When the charge is carried entirely by the Stern layer, the EDL would consist almost entirely of densely packed cations, as shown in Fig. 2.8. This is similar to the Helmholtz description of the EDL. This would mean that now the plane of closest approach for the solution species is at the edge of the EDL. As a result, the concentration of CO_2 involved in at least the first step of the reduction process, will be the same as the bulk concentration of CO_2 and the potential at reaction plane $\Phi_{OHP,\,t}$ in Eq. (2.13) becomes the same as the potential value in the bulk of electrolyte Φ_{Bulk}, hence the Frumkin-Butler-Volmer equation (Eq. 2.13) gets reduced to a simple Tafel relation:

$$j_p = j_{0,p} \frac{C_{CO_2,\,t}}{C_{CO_2 Bulk}} \exp\left[\frac{-a_{0,p}\mathrm{F}}{\mathrm{R_G}\,T}\left(E - E_{eq,p}\right)\right] \tag{2.16}$$

where $j_{0,p}$ and $a_{0,p}$ are the standard Tafel kinetics parameters. This type of model is now essentially solving the mass transport only in the diffusion layer with a Tafel like relation serving as a boundary condition at the edge of the diffusion layer. Since the diffusion

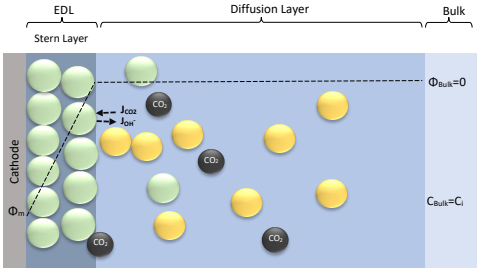

Figure 2.8: Limiting case of EDL consisting entirely of Stern layer.

layer can be assumed as charge neutral, the migration term in Eq. (2.4) can be dropped. The steric effects will have a negligible influence on the transport of the species in the diffusion layer, hence it can also be dropped from Eq. (2.4). As a result, the complete SMPNP transport equation reduces to a simple RD equation:

$$\frac{\partial C_i}{\partial t} = \nabla \cdot [D_i \nabla C_i] + \sum_s R_i \tag{2.17}$$

Hence using a standard Tafel kinetics equation, such as Eq. (2.16), is implicitly tied to using a RD type transport equation Eq. (2.17) and the EDL is described by the Helmholtz model. This type of formulation of EDL might be appropriate for high ionic strength systems but for the presented system, such a formulation is not sufficient, as the migration and steric effects inside the diffuse layer play a key role in the overall EDL dynamics and the charge transfer reactions.

2.4. DISCUSSION

The presented continuum scale approach to model CO_2 electrochemical reduction is extremely useful in analyzing the behavior of solution species in the EDL, while simultaneously being able to achieve practical current densities. Within a range of applied electrode potentials, this model can be used as a predictive tool for current-voltage analysis at elevated pressures. However, the model does find limitations at high applied electrode potentials, where we observed that the FBV-SMPNP model overpredicts the CO_2 concentration at the OHP and consequently overestimates the partial current density for $HCOO^-$ and CO formation, as both these products depend heavily on CO_2 concentration at the OHP. It is likely that at high applied electrode potentials, the first reduction step initiates beyond the condensed layer of counter ions [17]. This would in turn imply an overestimation of CO_2 in our current model at high electrode potentials. The kinetics model employed here is simplified by assuming that the specific adsorption of intermediate species and their lateral interactions do not significantly influence the interfacial charge transfer reactions. Explicitly accounting for these effects using DFT simulations might be necessary at these high electrode potentials since the coverage of metal surface and consequently the free space available for CO_2 intermediates depends heavily on the applied electrode potentials. Another possible explanation could be that at higher electrode potentials the EDL becomes increasingly more condensed, which in turn decreases the local diffusivities of solution species, which are currently assumed to have constant (Fickian) values. In our model, we use a linear equation (2.7) to evaluate the relative permittivity. This is done to avoid a high degree of nonlinearity that arises using more advanced approaches such as the Booth or Clausius-Mossotti equation[17, 49, 50]. Furthermore, It is also worth mentioning that the molarity of water in Eq. 2.7 is also assumed to be constant, however, the concentration of water would diminish near the electrode surface due to the presence of a condensed layer of solute species. We are currently exploring these effects as an extension for the FBV-SMPNP model.

The continuum-scale approach provides a cost effective alternative for the computationally expensive atomic-scale modeling of EDL. It can also be coupled with atomistic quantum models to provide the steady-state condition under which energetics are to be studied [17]. A continuum scale approach does not account for the ion-ion interactions,

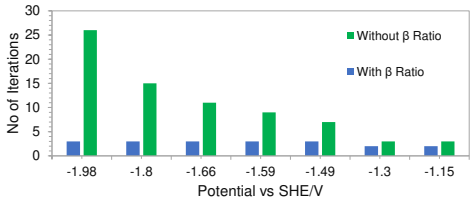

Figure 2.9: Comparison of computational efficiency with and without the inclusion of β_i ratio.

which become relevant in concentrated electrolytes. Giera et. al performed extensive MD simulations using a primitive model to successfully account for electrostatic correlations as well as steric interactions between ions[51]. However, the applicability of such an approach for a typical CO_2ER process still remains unexplored. This is primarily because a typical CO_2ER process involves electrode reactions and homogenous reactions, and local pH plays an important role. These factors affect the EDL in a CO_2ER system and are generally hard to simulate in MD. Moreover, the accuracy of an MD simulation would be contingent on a good description of molecular interactions between all the fluid components and their interaction with the electrode[52]. Available interaction potentials are typically not suitable to describe the interface between a conducting surface and a multicomponent concentrated solution. A more suitable methodology will be to use a tandem approach based on coupling MD simulations and continuum scale models to leverage their complementary strengths and overcome the inherent limitations in both approaches.

Another feature of the Frumkin-corrected kinetics approach is that it does not presuppose a fixed OHP potential. Rather it is evaluated at every time step. This would in turn determine the local electric field strength of the EDL, which eventually dictates the concentrations of different ionic species. This feature can be especially useful for dynamic CO_2 reduction models, where the applied electrode potential is switched on and off (or high to low voltage) repeatedly to overcome diffusion limitations. Traditionally, it has been seen that solving (G)MPNP type differential equations at relatively high applied electrode potentials, in an EDL like environment leads to increased instability [17]. Extremely small time steps and spatial discretizations, along with stabilization techniques such as the SUPG method, have to be adopted to get a tractable solution. Interestingly, using our FBV-SMPNP type approach leads to a computationally much more efficient solution, without the need for any stabilization technique. This is due to a hard concentration limit being enforced on the solution species near the electrode surface via the introduction of the β_i ratio in the volume exclusion term resulting in less extreme potential gradients. Fig. 2.9 shows a comparison of the average number of iterations required (per time step) using Newton's method, with and without the inclusion of the β_i ratio, as a function of applied electrode potential. In the case where the ratio was excluded from the model, the solution would not even converge at high electrode potentials. The number of iterations in the green bars represents the average number of iterations before the system fails to converge. However for the case where the ratio was included, not only does the solution converge but the number of iterations remained relatively stable throughout the range of

applied electrode potentials.

2.5. CONCLUSIONS

In this work we presented a CO_2 reduction modeling approach based on a combination of size-modified Poisson-Nernst-Planck equations (SMPNP) for transport of the solution species and Frumkin-corrected Butler-Volmer type kinetics expression (FBV) to account for the interfacial reactions. By considering steric effects, we established the impact of the condensed layer of cations on the accessibility of the catalyst surface to the reacting CO_2. We also observed a 50% decline in the estimated cation concentration at the reaction plane as compared to a GMPNP model [17]. This is due to the inclusion of the molecular size (β_i) ratio in the transport equations of our model. Perhaps its impact is most prominent in the estimation of CO_2 concentration at the OHP, which was predicted to be extremely low in the GMPNP model. Using the β_i ratio, we were able to rectify this problem and attain a much more realistic CO_2 concentration at the OHP. We also validated the usage of this factor by matching the partial current density data for CO_2 consuming products such as $HCOO^-$ and CO with the experimental Tafel plot data from the literature. The FBV-SMPNP model can also be used to make predictions for a high pressure CO_2 electrolyzer, which is of great industrial significance. Within a range of applied electrode potentials, we were able to predict the partial current densities of all 3 products with accuracy at elevated pressures of 5 and 40 bar, although the model does find limitations in predicting partial current densities for CO_2 consuming products at high applied electrode potentials. We also observed that the model predicts the HER current densities much more accurately than a traditional RD model. This is due to the Frumkin-corrected kinetics formulation which assumes the driving force for interfacial charge transfer reactions to be the potential difference between the metal electrode and the OHP.

Overall, the model provides a good approximation of the CO_2 reaction environment which consists of several physicochemical phenomena occurring at vastly different lengths and time scales, in a computationally inexpensive manner. Gas diffusion electrodes (GDE) based CO_2 electro-reduction systems are being studied extensively because of their advantage of reduced diffusion length for CO_2 molecules. Such a system can also be incorporated within the FBV-SMPNP framework presented in this study. The model can also be useful in dynamic CO_2 reduction systems, where step changes in the applied potential are used as a method to overcome diffusive limitations via the dispersion of the double layer.

REFERENCES

[1] Xu Lu, Dennis Y.C. Leung, Huizhi Wang, Michael K.H. Leung, and Jin Xuan. “Electrochemical Reduction of Carbon Dioxide to Formic Acid”. In: *ChemElectroChem* 1 (5 2014), pp. 836–849. ISSN: 21960216. DOI: 10.1002/celc.201300206.

[2] Wilson A. Smith, Thomas, David A. Vermaas, and Hans Geerlings. “Pathways to Industrial-Scale Fuel Out of Thin Air from CO_2 Electrolysis”. In: *Joule* 3 (8 Aug. 2019), pp. 1822–1834. ISSN: 25424351. DOI: 10.1016/j.joule.2019.07.009.

[3] Zhifei Yan, Jeremy L. Hitt, John A. Turner, and Thomas E. Mallouk. "Renewable electricity storage using electrolysis". In: *Proceedings of the National Academy of Sciences of the United States of America* 117 (23 June 2020), pp. 12558–12563. ISSN: 10916490. DOI: 10.1073/pnas.1821686116.

[4] Gastón O. Larrazábal, Antonio J. Martín, and Javier Pérez-Ramírez. "Building Blocks for High Performance in Electrocatalytic CO2 Reduction: Materials, Optimization Strategies, and Device Engineering". In: *Journal of Physical Chemistry Letters* 8 (16 Aug. 2017), pp. 3933–3944. ISSN: 19487185. DOI: 10.1021/acs.jpclett.7b01380.

[5] Min Liu, Yuanjie Pang, Bo Zhang, Phil De Luna, Oleksandr Voznyy, Jixian Xu, Xueli Zheng, Cao Thang Dinh, Fengjia Fan, Changhong Cao, F. Pelayo García De Arquer, Tina Saberi Safaei, Adam Mepham, Anna Klinkova, Eugenia Kumacheva, Tobin Filleter, David Sinton, Shana O. Kelley, and Edward H. Sargent. "Enhanced electrocatalytic CO_2 reduction via field-induced reagent concentration". In: *Nature* 537 (7620 Aug. 2016), pp. 382–386. ISSN: 14764687. DOI: 10.1038/nature19060.

[6] Joaquin Resasco, Leanne D. Chen, Ezra Clark, Charlie Tsai, Christopher Hahn, Thomas F. Jaramillo, Karen Chan, and Alexis T. Bell. "Promoter Effects of Alkali Metal Cations on the Electrochemical Reduction of Carbon Dioxide". In: *Journal of the American Chemical Society* 139 (32 Aug. 2017), pp. 11277–11287. ISSN: 15205126. DOI: 10.1021/jacs.7b06765.

[7] Laura Scalfi, Mathieu Salanne, and Benjamin Rotenberg. "Molecular Simulation of Electrode-Solution Interfaces". In: *Annual Review of Physical Chemistry* 72.1 (2021), pp. 189–212. DOI: 10.1146/annurev-physchem-090519-024042.

[8] Max F. Döpke, Fenna Westerbaan van der Meij, Benoit Coasne, and Remco Hartkamp. "Surface Protolysis and Its Kinetics Impact the Electrical Double Layer". In: *Phys. Rev. Lett.* 128 (5 Feb. 2022), p. 056001. DOI: 10.1103/PhysRevLett.128.056001. URL: https://link.aps.org/doi/10.1103/PhysRevLett.128.056001.

[9] N. Gupta, M. Gattrell, and B. MacDougall. "Calculation for the cathode surface concentrations in the electrochemical reduction of CO2 in KHCO3 solutions". In: *Journal of Applied Electrochemistry* 36 (2 2006), pp. 161–172. ISSN: 0021891X. DOI: 10.1007/s10800-005-9058-y.

[10] Charles Delacourt and John Newman. "Mathematical Modeling of CO[sub 2] Reduction to CO in Aqueous Electrolytes". In: *Journal of The Electrochemical Society* 157 (12 2010), B1911. ISSN: 00134651. DOI: 10.1149/1.3502533.

[11] David Raciti, Mark Mao, and Chao Wang. "Mass transport modelling for the electroreduction of CO(2) on Cu nanowires." In: *Nanotechnology* 29 (4 Jan. 2018), p. 44001. ISSN: 1361-6528 (Electronic). DOI: 10.1088/1361-6528/aa9bd7.

[12] Hiroshi Hashiba, Lien-Chun Weng, Yikai Chen, Hiroki K Sato, Satoshi Yotsuhashi, Chengxiang Xiang, and Adam Z Weber. "Effects of Electrolyte Buffer Capacity on Surface Reactant Species and the Reaction Rate of CO2 in Electrochemical CO2 Reduction". In: *The Journal of Physical Chemistry C* 122 (7 Feb. 2018). doi: 10.1021/acs.jpcc.7b11316, pp. 3719–3726. ISSN: 1932-7447. DOI: 10.1021/acs.jpcc.7b11316. URL: https://doi.org/10.1021/acs.jpcc.7b11316.

[13] Silvan Suter and Sophia Haussener. “Optimizing mesostructured silver catalysts for selective carbon dioxide conversion into fuels”. In: *Energy & Environmental Science* 12 (5 2019), pp. 1668–1678. ISSN: 1754-5692. DOI: 10.1039/C9EE00656G.

[14] John Newman and Karen Thomas-Alyea. *Electrochemical Systems*. 3rd ed. John Wiley & Sons, 2004.

[15] Mustafa Sabri Kilic, Martin Z. Bazant, and Armand Ajdari. “Steric effects in the dynamics of electrolytes at large applied voltages. I. Double-layer charging”. In: *Physical Review E - Statistical, Nonlinear, and Soft Matter Physics* 75 (2 2007), pp. 1–16. ISSN: 15393755. DOI: 10.1103/PhysRevE.75.021502.

[16] Mustafa Sabri Kilic, Martin Z. Bazant, and Armand Ajdari. “Steric effects in the dynamics of electrolytes at large applied voltages. II. Modified Poisson-Nernst-Planck equations”. In: *Physical Review E - Statistical, Nonlinear, and Soft Matter Physics* 75 (2 Feb. 2007), p. 021502. ISSN: 15393755. DOI: 10.1103/PhysRevE.75.021503.

[17] Divya Bohra, Jehanzeb H. Chaudhry, Thomas, Evgeny A. Pidko, and Wilson A. Smith. “Modeling the electrical double layer to understand the reaction environment in a CO_2 electrocatalytic system”. In: *Energy and Environmental Science* 12 (11 2019), pp. 3380–3389. ISSN: 17545706. DOI: 10.1039/c9ee02485a.

[18] Martin Z Bazant, Mustafa Sabri Kilic, Brian D Storey, and Armand Ajdari. “Towards an understanding of induced-charge electrokinetics at large applied voltages in concentrated solutions.” In: *Advances in colloid and interface science* 152 (1-2 Nov. 2009), pp. 48–88. ISSN: 1873-3727 (Electronic). DOI: 10.1016/j.cis.2009.10.001.

[19] Toru Hatsukade, Kendra P Kuhl, Etosha R Cave, David N Abrama, and Thomas F Jaramillo. “Insights into the electrocatalytic reduction of CO2 on metallic silver surfaces”. In: *Physical Chemistry Chemical Physics* (2014), pp. 13814–13819. DOI: 10.1039/C4CP00692E.

[20] Benzhuo Lu and Y. C. Zhou. “Poisson-Nernst-Planck equations for simulating biomolecular diffusion-reaction processes II: Size effects on ionic distributions and diffusion-reaction rates”. In: *Biophysical Journal* 100 (10 May 2011), pp. 2475–2485. ISSN: 15420086. DOI: 10.1016/j.bpj.2011.03.059.

[21] Kherim Willems, Dino Ruic, Florian L.R. Lucas, Ujjal Barman, Niels Verellen, Johan Hofkens, Giovanni Maglia, and Pol Van Dorpe. “Accurate modeling of a biological nanopore with an extended continuum framework”. In: *Nanoscale* 12 (32 Aug. 2020), pp. 16775–16795. ISSN: 20403372. DOI: 10.1039/d0nr03114c.

[22] Kunna Wu, Erik Birgersson, Byoungsu Kim, Paul J. A. Kenis, and Iftekhar A. Karimi. “Modeling and Experimental Validation of Electrochemical Reduction of CO 2 to CO in a Microfluidic Cell”. In: *Journal of The Electrochemical Society* 162 (1 2015), F23–F32. ISSN: 0013-4651. DOI: 10.1149/2.1021414jes.

[23] Andrew R. T. Morrison, Vincent van Beusekom, Mahinder Ramdin, Leo J. P. van den Broeke, Thijs J. H. Vlugt, and Wiebren de Jong. "Modeling the Electrochemical Conversion of Carbon Dioxide to Formic Acid or Formate at Elevated Pressures". In: *Journal of The Electrochemical Society* 166 (4 2019), E77–E86. ISSN: 0013-4651. DOI: 10.1149/2.0121904jes.

[24] A Frumkin. "wasserstoffuberspannung und struktur der doppelschicht." In: *Zeitschrift für physikalische Chemie* 164 (1 1933), pp. 121–133.

[25] M van Soestbergen. "Frumkin-Butler-Volmer theory and mass transfer in electrochemical cells". In: *Russian Journal of Electrochemistry* 48 (6 2012), pp. 570–579. ISSN: 1608-3342. DOI: 10.1134/S1023193512060110.

[26] Stefan Ringe, Carlos G. Morales-Guio, Leanne D. Chen, Meredith Fields, Thomas F. Jaramillo, Christopher Hahn, and Karen Chan. "Double layer charging driven carbon dioxide adsorption limits the rate of electrochemical carbon dioxide reduction on Gold". In: *Nature Communications* 11 (1 Dec. 2020), p. 33. ISSN: 20411723. DOI: 10.1038/s41467-019-13777-z.

[27] Marco Rossi, Thomas Wallmersperger, Stefan Neukamm, and Kathrin Padberg-Gehle. "Modeling and Simulation of Electrochemical Cells under Applied Voltage". In: *Electrochimica Acta* 258 (2017), pp. 241–254. ISSN: 00134686. DOI: 10.1016/j.electacta.2017.10.047. URL: http://dx.doi.org/10.1016/j.electacta.2017.10.047.

[28] Makoto Todoroki, Kohjiro Hara, Akihiko Kudo, and Tadayoshi Sakata. "Electrochemical reduction of high pressure CO_2 at Pb, Hg and In electrodes in an aqueous $KHCO_3$ solution". In: *Journal of Electroanalytical Chemistry* 394 (1 1995), pp. 199–203. ISSN: 1572-6657. DOI: https://doi.org/10.1016/0022-0728(95)04010-L.

[29] S Weisenberger and A Schumpe. "Estimation of gas solubilities in salt solutions at temperatures from 273 K to 363 K". In: *AIChE Journal* 42 (1 Jan. 1996). doi: 10.1002/aic.690420130, pp. 298–300. ISSN: 0001-1541. DOI: 10.1002/aic.690420130. URL: https://doi.org/10.1002/aic.690420130.

[30] Thomas Burdyny, Percival J. Graham, Yuanjie Pang, Cao-Thang Dinh, Min Liu, Edward H. Sargent, and David Sinton. "Nanomorphology-Enhanced Gas-Evolution Intensifies CO_2 Reduction Electrochemistry". In: *ACS Sustainable Chemistry and Engineering* 5 (5 May 2017), pp. 4031–4040. DOI: 10.1021/acssuschemeng.7b00023.

[31] B. Patrick Sullivan and H. E. Guard K. Krist. *Electrochemical and Electrocatalytic Reactions of Carbon Dioxide*. 1st ed. Elsevier Science, 1993.

[32] Martin Z. Bazant, Kevin T. Chu, and B. J. Bayly. "Current-voltage relations for electrochemical thin films". In: *SIAM Journal on Applied Mathematics* 65 (5 2005), pp. 1463–1484. ISSN: 00361399. DOI: 10.1137/040609938.

[33] Antoine Bonnefont, Francçoise Argoul, and Martin Z. Bazant. "Analysis of diffuse-layer effects on time-dependent interfacial kinetics". In: *Journal of Electroanalytical Chemistry* 500 (1-2 2001), pp. 52–61. ISSN: 00220728. DOI: 10.1016/S0022-0728(00)00470-8.

[34] Hainan Wang, Alexander Thiele, and Laurent Pilon. “Simulations of Cyclic Voltammetry for Electric Double Layers in Asymmetric Electrolytes: A Generalized Modified Poisson–Nernst–Planck Model”. In: *The Journal of Physical Chemistry C* 117 (36 Sept. 2013), pp. 18286–18297. ISSN: 1932-7447. DOI: 10.1021/jp402181e.

[35] J. B. Hasted, D. M. Ritson, and C. H. Collie. “Dielectric Properties of Aqueous Ionic Solutions. Parts I and II”. In: *The Journal of Chemical Physics* 16 (1 Jan. 1948), pp. 1–21. ISSN: 0021-9606. DOI: 10.1063/1.1746645. URL: http://aip.scitation.org/doi/10.1063/1.1746645.

[36] John Bockris and Amulya Reddy. *Modern Electrochemistry*. 2nd. Springer New York, NY, 1998.

[37] Jeremy T Feaster, Chuan Shi, Etosha R Cave, Toru Hatsukade, David N Abram, Kendra P Kuhl, Christopher Hahn, Jens K Nørskov, and Thomas F Jaramillo. “Understanding Selectivity for the Electrochemical Reduction of Carbon Dioxide to Formic Acid and Carbon Monoxide on Metal Electrodes”. In: *ACS Catalysis* 7 (7 July 2017). doi: 10.1021/acscatal.7b00687, pp. 4822–4827. DOI: 10.1021/acscatal.7b00687. URL: https://doi.org/10.1021/acscatal.7b00687.

[38] Yoshio Hori, Hidetoshi Wakebe, Toshio Tsukamoto, and Osamu Koga. “Electrocatalytic process of CO selectivity in electrochemical reduction of CO2 at metal electrodes in aqueous media”. In: *Electrochimica Acta* (1994). https://doi.org/10.1016/0013-4686(94)85172-7, pp. 1833–1839. DOI: 10.1016/0013-4686(94)85172-7.

[39] Yoshio Hori. *Modern Aspects of Electrochemistry pp 89–189*. Vol. 42. Springer, New York, NY, 2008.

[40] Jiayu Li, Minghui Zhu, and Yi Fan Han. “Recent Advances in Electrochemical CO2 Reduction on Indium Based Catalysts”. In: *European Society Journal for Catalysis* (2020). https://doi.org/10.1002/cctc.202001350, pp. 514–531. DOI: 10.1002/cctc.202001350.

[41] S. Kapusta and N. Hackerman. “The Electroreduction of Carbon Dioxide and Formic Acid on Tin and Indium Electrodes”. In: *Journal of the Electrochemical Society* (1983). https://doi.org/10.1149/1.2119761, p. 607. DOI: 10.1149/1.2119761.

[42] E 31 Itsicovich, A A Korxyshev, and 3j A Vorotyntsev. *Subjcct classification: 14.3.2; 14.3.4; 22.5.1 Institute of Blectrochmmatry, Academy of ScieiLces of tlw USSR, iV-Ioscow') (u) and it chanico-,MnthPmatienl Faculty*. 1977.

[43] P. M. Biesheuvel, M. van Soestbergen, and M. Z. Bazant. “Imposed currents in galvanic cells”. In: *Electrochimica Acta* 54 (21 2009), pp. 4857–4871. ISSN: 00134686. DOI: 10.1016/j.electacta.2009.03.073.

[44] Paul Delahay. *Double Layer and Electrode Kinetics*. 2nd ed. Interscience, 1965.

[45] Allen Bard and Larry Faulkner. *Electrochemical Methods: Fundamentals and Applications, 2nd ed.* Vol. 38. Wiley, 2002. DOI: 10.1023/A:1021637209564.

[46] Sergio Trasatti and Enn Lust. “The Potential of Zero Charge”. In: *Modern Aspects of Electrochemistry* (2002), pp. 1–215. DOI: 10.1007/0-306-46917-0_1.

[47] E Nightingale. “PHENOMENOLOGICAL THEORY OF ION SOLVATION. EFFECTIVE RADII OF HYDRATED IONS”. In: *J. Phys. Chem* (1959).

[48] Xinwei Zhu, Jun Huang, and Michael Eikerling. "Electrochemical CO_2 Reduction at Silver from a Local Perspective". In: *ACS Catalysis* 11 (23 Dec. 2021), pp. 14521–14532. ISSN: 21555435. DOI: 10.1021/acscatal.1c04791.

[49] F. Booth. "The Dielectric Constant of Water and the Saturation Effect". In: *The Journal of Chemical Physics* (1951). https://doi.org/10.1016/0013-4686(94)85172-7, pp. 391–394. DOI: 10.1063/1.1748233.

[50] John Daintith. *A Dictionary of Chemistry*. Vol. 6. OUP Oxford, 2008.

[51] Brian Giera, Neil Hanson, Edward M. Kober, and M.Scot Shell Todd M. Squires. "Electric Double-Layer Structure in Primitive Model Electrolytes: Comparing Molecular Dynamics with Local-Density Approximations". In: *Langmuir* (2015), pp. 3553–3562. DOI: https://doi.org/10.1021/la5048936.

[52] Max F. Döpke and Remco Hartkamp. "The importance of specifically adsorbed ions for electrokinetic phenomena: Bridging the gap between experiments and MD simulations". In: *The Journal of Chemical Physics* 154 (2021), p. 094701. DOI: https://doi.org/10.1063/5.0038161.

3

PORE-SCALE DYNAMICS IN GDE SYSTEMS

The local conditions inside a gas diffusion electrode (GDE) pore, especially in the electrical double layer (EDL) region, influence the charge transfer reactions and the selectivity of desired CO_2ER products. Most GDE computational models ignore the EDL or are limited in their applicability at high potentials. In this work, we present a continuum model to describe the local environment inside a catalytic pore at varying potentials, electrolyte concentrations and pore diameters. The systems studied in this work are based on an Ag catalyst in contact with $KHCO_3$ solution. Our study shows that steric effects dominate the local environment at high cathodic potentials (≪-25 mV vs pzc at the OHP), leading to a radial drop of CO_2 concentration. We also observe a drop in pH value within 1 nm of the reaction plane due to electrostatic repulsion and attraction of OH^- and H^+ ions, respectively. We studied the influence of pore radii (1-10 nm) on electric field and concentrations. Pores with a radius smaller than 5 nm show a higher mean potential, which lowers the mean CO_2 concentration. Pores with a favourable local environment can be designed by regulating the ratio between the pore radius and Debye length.

3.1. INTRODUCTION

With the growing awareness of the impact of climate change, the demand for cleaner and non-fossil fuel-based energy sources is also increasing, and storing renewable energy over a long period of time is becoming of utmost importance. In this regard, CO_2 electrochemical reduction (CO_2ER) is one of the most attractive technologies to replace fossil fuels [1–3]. This process results in the formation of molecules that can be utilized as fuels and as chemical feedstock in various industries such as pharmaceutical, cosmetic, and plastic [4–6]. Although extensive research has been performed to make the CO_2ER

This chapter is based on the article: E. N. Butt, J. T. Padding. R. M. Hartkamp, "Local Reaction Environment Deviations within Gas Diffusion Electrode Pores for CO_2 Electrolysis," *Journal of The Electrochemical Society*, 2024, **171**(1), 014504, DOI: 10.1149/1945-7111/ad1cb4.

process commercially viable, large-scale implementation is still not possible due to the inherent complexity of the process.

Conventional metal electrode cells are limited in their applicability due to severe mass transfer limitations for CO_2. Gas diffusion electrodes (GDE) overcome the limitation by delivering CO_2 in the gas phase directly to the catalytic pore in contact with the electrolyte[7]. This significantly reduces the distance CO_2 has to travel and has been shown to increase the current densities of desired CO_2ER reactions[8, 9].

Optimal design of a GDE is at the forefront of CO_2ER research. Most of the experimental research in this field focuses on the optimization of catalyst metal composition [7, 10]. The goal is generally to optimize for stability and selectivity of the desired CO_2ER products[11]; however, because of the small length scales involved in such an electrochemical cell configuration, it is extremely challenging to probe the local environment inside a pore using experimental techniques. Continuum models are a cheap and reliable alternative to not only study the GDEs but also to optimize their design. The main interest in CO_2ER models lies in the cathodic half of the cell, where the CO_2ER process takes place [12–17]. The cathodic GDE is made up of a macroporous gas diffusion layer (GDL) for the distribution of CO_2 from the gas inlet to the catalytic pores and for the transport of products from the catalytic pores to the outlet stream. A hydrophobic microporous layer (MPL) composed of carbon nanoparticles is deposited on top of the GDL, acting as a current collector and barrier for the liquid electrolyte. The catalyst nanoparticle layer (CL) is coated directly on top of the MPL. Gaseous CO_2 is introduced via an inlet stream that flows along the GDL. It passes through the GDL/MPL sections to reach the catalyst layer where the reaction takes place. The aqueous electrolyte is circulated via the electrolyte flow channel alongside the catalyst layer.

Most of the research on GDE flow cells is based on one-dimensional (1D) models that do not incorporate the influences of pore size on the local reaction environment [8, 18–20] and thus are unable to capture the complete spatial variation in the concentration. Some models assume an infinitely thin CL in contact with the electrolyte, hence bypassing the modelling of ion transport inside the CL [21]. There have been some attempts to include the 2D effects along the flow channel; however, such models often do not account for pore-scale transport [22] or do not consider the influence of steric effects on the local concentrations and pH profiles [23, 24]. Furthermore, most of these models assume electroneutrality throughout the simulation domain. This condition is generally valid for modelling the transport of solution species within the diffusion layer. However, this is not valid for transport within the diffuse layer of the electric double layer (EDL). This region is defined by charge separation which results in large concentration gradients near the pore wall. This local environment within the catalytic pore is a key factor determining the overall performance and selectivity of desired products [25–28]. Bohra et. al. [29] attempted a pore-scale model that did consider the EDL and steric effects inside a nanopore; however, the authors faced numerical instability beyond a potential value of -25 mV vs pzc on the outer helmholtz plane (OHP). This severely limited the descriptive capabilities of their model as many industrially relevant CO_2ER reactions become thermodynamically favoured at higher potential ranges [30].

In this work, we present an approach to model the CO_2ER process inside a single cylindrical nanopore of a GDE-based electrolyzer. We use the size-modified Poisson-Nernst-

Planck (SMPNP) framework as described in our previous work for a flat metal-based electrode system and modify it for a GDE nanopore [31]. Our aim with this study is to highlight the variation in the predicted local properties inside a nanopore due to changes in key performance-controlling parameters such as the size of the pore, electrolyte concentration, and the applied electrode potential. We first highlight the influence of the applied potential on the concentration profiles of solution species inside a nanopore. By doing so, we emphasize the importance of steric effects for such nanoporous spaces in CO_2ER. We then point out the radial trend of the local pH and show its variation with applied potential. We also show a strong influence of ionic strength on the amount of dissolved CO_2 inside the nanopore. Finally, we highlight the effect of pore size on the local reaction environment and demonstrate the importance of the ratio between the pore radius R and the Debye length λ_{Debye} in regulating the pH behaviour inside a nanopore.

3.2. MODEL DESCRIPTION

Fig. 3.1a illustrates the idealized CL, assumed to be in the shape of an axisymmetric cylindrical nanopore. Since the studied catalyst pores are very small (1-10 nm) and hydrophilic, they are completely flooded by electrolyte[18, 29]. The pore entrance on the left-hand side serves as the location of gas/liquid interface. The model is adopted for an Ag(111)-based catalytic pore. Silver is chosen because it is one of the more extensively researched metals in GDE-based CO_2ER studies due to its high selectivity towards CO [18, 29, 32]. The axisymmetric pore is conveniently described in a two-dimensional model (fig. 3.1b). Furthermore, we introduce a reservoir section at the right hand side of the domain between the pore and the bulk electrolyte region. The reservoir section not only allows for a realistic transport of solution species into the catalyst layer but it also facilitates numerical convergence by allowing a gradual development of ionic concentration profiles at high applied potentials, thus enhancing stability. The risk of instability is highest at the pore entrance near the reaction plane B2. By applying the same potential on the reservoir wall B3 as on the reaction plane B2 (fig. 3.1b), we allow a smooth gradient in the potential fields which makes the overall system numerically stable even at high applied potentials. The applied potential ranges from -0.12 to -0.3 V vs pzc at the OHP. The boundaries in the reservoir section do not take part in the CO_2ER reactions. The transport equations and the homogeneous reactions are solved throughout the simulation domain.

$KHCO_3$ is chosen as the electrolyte in this work because it is one of the most commonly used electrolytes in Ag-based CO_2ER processes [18, 29, 32]. The following homogeneous equilibrium reactions occur in the electrolyte:

$$HCO_3^- + OH^- \underset{k_{-1}}{\overset{k_1}{\rightleftharpoons}} CO_3^{2-} + H_2O, \tag{3.1}$$

$$CO_2 + OH^- \underset{k_{-2}}{\overset{k_2}{\rightleftharpoons}} HCO_3^-, \tag{3.2}$$

$$H_2O \underset{k_{-3}}{\overset{k_3}{\rightleftharpoons}} H^+ + OH^-. \tag{3.3}$$

Here, k_n and k_{-n} are the forward and backward rate constants, respectively. All the rate constant values are listed in Appendix D (Table D.2). The model solves for the

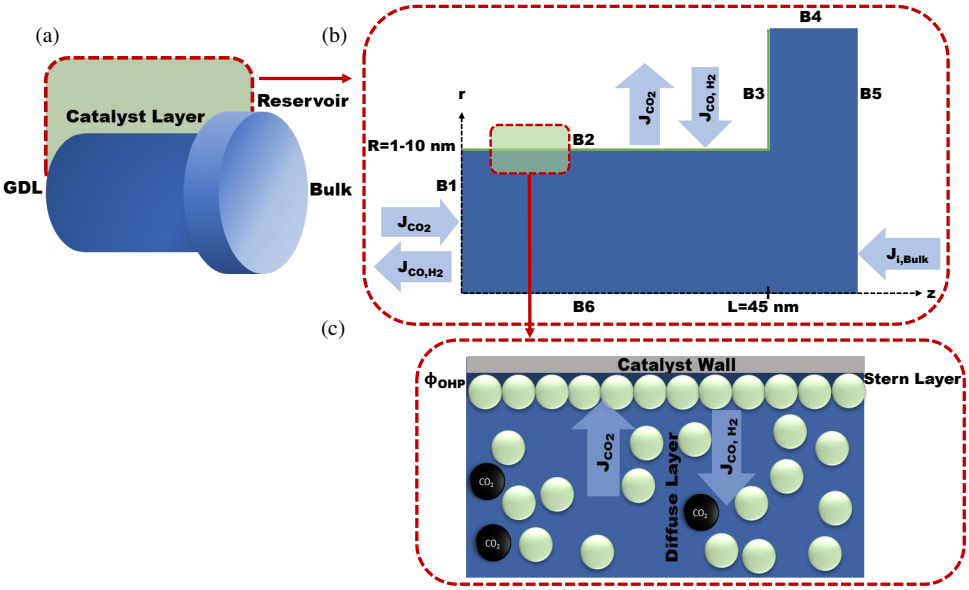

Figure 3.1: (a) Schematic of an idealized catalyst layer in the shape of a cylindrical pore along with reservoir section. (b) 2D simulation domain based on the axisymmetry condition. (c) A zoomed-in visual of the catalyst pore wall including cation-bound Stern and Diffuse layer. The reservoir section has width=5 nm and a height of height=R+5 nm. B1 to B6 represent the boundaries of the simulation domain.

mass transport of the following 8 species: CO_2, CO, OH^-, H_2, $HCO_3{}^-$, K^+, $CO_3{}^{2-}$ and H^+ throughout the simulation domain (fig. 3.1b). The following set of SMPNP equations (eqs. 3.4-3.7) is used to model the transport:

$$\frac{\partial C_i}{\partial t} = \nabla \cdot \left[D_i \nabla C_i + \frac{D_i C_i z_i F}{RT} \nabla \Phi + D_i C_i \left(\frac{\beta_i N_A \sum_{j=1}^{n} a_j^3 \nabla C_j}{1 - N_A \sum_{j=1}^{n} a_j^3 C_j} \right) \right] + \sum_s R_i. \tag{3.4}$$

C_i represents the concentration of solution species i. z_i is the valency of species i, a_j represents the effective hydrated size of all ionic species. However, for j=CO_2, a_j represents the size of the unhydrated CO_2 molecule because CO_2 has a very weak solvation shell in polar solvents. Φ is the local electric potential. F is Faraday's constant, R is the gas constant, T represents the absolute temperature of the system and N_A is Avogadro's number. R_i represents the formation rate for species i in the homogeneous reactions (eqs. 3.1-3.3) (see Appendix D for detailed methodology). D_i is the diffusivity of species i. Values of all diffusivities and sizes of all the solution species are given in Appendix D. The first two terms on the right-hand side of eq. 3.4 are the diffusion and migration terms, respectively. The third term comes from the excluded volume effect [33–38]. The β_i factor in the excluded volume term is given by:

$$\beta_i = \frac{a_i^3}{a_0^3}. \tag{3.5}$$

Here, a_0 is the effective size of H_2O molecules. β_i acts as a magnification factor for the steric repulsion acting on species i inside the solution ([31, 39, 40]). Eq. (3.4) is solved self-consistently with the Poisson equation:

$$\nabla \cdot (\epsilon_0 \epsilon_r \nabla \Phi) = -F \sum_{i=1}^{n} z_i C_i. \tag{3.6}$$

Here, ϵ_0 is the permittivity of the vacuum and ϵ_r is the relative permittivity of the aqueous electrolyte. ϵ_r varies with the local cation concentration (K^+, H^+) [27, 41, 42] and it is evaluated at every time step:

$$\epsilon_r = \epsilon_r^0 \left[\frac{M_{H_2O} - \sum_i^{n_{cat}} w_i C_i}{M_{H_2O}} \right] + \epsilon_r^{min} \left[\frac{\sum_i^{n_{cat}} w_i C_i}{M_{H_2O}} \right]. \tag{3.7}$$

M_{H_2O} and ϵ_r^0 represent the molarity and the permittivity of pure water at room temperature. w_i is the number of cation-bound water molecules. ϵ_r^{min} is the dielectric constant of water under the condition of dielectric saturation [41, 42]. Based on the Gouy-Chapman-Stern theory for the EDL, an immobile layer of adsorbed cations is formed at the pore wall due to an applied surface potential. This layer is called the Stern layer and its thickness is assumed to be slightly larger than the radius of a solvated K^+ ion (≈0.4 nm) [27]. Consequently, the outer Helmholtz plane (OHP) marks the plane of closest approach for the solution species and also the CO_2ER reaction plane. The potential drop across the Stern layer is often a modelling parameter as it requires assuming the relative permittivity and thickness of the Stern layer, both of which are hard to measure experimentally. A mixed Robin boundary condition based on the experimental data on Stern layer capacitance under similar conditions can be used to calculate the drop[43]. Since this work mainly focuses on resolving the local environment within the diffuse layer, we fix the potential values at the OHP rather than at the electrode. Note that the OHP corresponds to boundary B2 in fig. 3.1b, and that therefore the radius R of the simulation domain is slightly smaller than the physical pore radius. The electrochemical reactions occurring at B2 are as follows:

$$CO_2(aq) + H_2O + 2e^- \rightleftharpoons CO(g) + 2OH^-, \tag{3.8}$$

$$2H_2O + 2e^- \rightleftharpoons H_2(g) + 2OH^-. \tag{3.9}$$

The mass transport model presented in this work can also be used for CO_2ER processes based on other catalytic metals such as Cu, Sn and In. This can be achieved by accounting for heterogeneous reactions and products specific to the catalyst being used, instead of Ag (111) (eqs. 3.8 and 3.9). The next subsections detail the boundary conditions implemented in the simulation domain.

Gas/Liquid Interface (B1)

This boundary exists at the interface of the MPL and the CL. The inlet gas stream passes through the GDL/MPL region to reach the gas/liquid interface B1. The flux of all solution species, except CO_2, CO and H_2, is assumed to be 0.

$$J_i = 0, \qquad i = HCO_3^-, K^+, H^+, OH^-, CO_3^{2-}. \tag{3.10}$$

The CO and H_2 concentrations at the B1 boundary are determined by the following Dirichlet boundary condition:

$$C_i^{B1} = H_i p_1 y_i \rho_{elec}, \qquad i = \mathrm{CO}, \mathrm{H_2}. \tag{3.11}$$

Here, H_i is Henry's constant, p_1 is the gas stream pressure and ρ_{elec} is the electrolyte density, taken to be the density of water. y_i is the gas phase fraction of species i (Table S7). For CO_2, a Neumann flux condition based on Sechenov-corrected Henry's law is used[8, 29, 44, 45].

$$J_{\mathrm{CO_2}}^{B1} = \kappa_{B1}(C_{\mathrm{CO_2}}^{B1} - C_{\mathrm{CO_{2(aq)}}}). \tag{3.12}$$

Here, $C_{\mathrm{CO_2}}^{B1}$, is the saturated concentration of CO_2, evaluated at every time step using the Sechenov-corrected Henry's relation (Appendix D). $C_{\mathrm{CO_{2(aq)}}}$ is the local concentration of CO_2 inside the pore. κ_{B1}, is the gas/liquid interface mass transfer coefficient and is calculated based on film theory [8, 23].

$$\kappa_{B1} = \frac{D_{\mathrm{CO_2}}}{\sigma}. \tag{3.13}$$

Here, the film thickness (σ) depends on the level of saturation (S) inside the pore [8, 18]:

$$\sigma = \frac{d_p}{2}(1 - \sqrt{1 - S}). \tag{3.14}$$

A zero electric field condition is adopted for the B1 interface:

$$\nabla \Phi = 0. \tag{3.15}$$

Reaction Plane (B2)

The flux of the species involved in the charge transfer reactions at OHP (r=R) and time t is given by:

$$J_{i,(OHP,t)} = \sum_p \frac{\nu_{i,p} I_{ECSA} F E_p}{n_p F}, \qquad i = \mathrm{CO_2}, \mathrm{H_2}, \mathrm{CO}, \mathrm{OH^-}. \tag{3.16}$$

$\nu_{i,p}$ represents the stoichiometric coefficient for species i in reaction p (eqs. 3.8 and 3.9). n_p is the number of overall electrons transferred in reaction p. I_{ECSA} is the current density of the electrochemically active surface area and is calculated as [29]:

$$I_{ECSA} = \frac{I_{GEOM}}{f_r}. \tag{3.17}$$

I_{GEOM} is the geometric current density and f_r is the electrode roughness factor. The electrochemically active surface area increases with increasing roughness of the electrode. f_r depends on the type of catalyst material used as well as the thickness of CL. FE_p is the Faradaic efficiency of reaction p.
For the species that do not take part in the charge transfer reactions:

$$J_{i,(OHP,t)} = 0, \qquad i = \mathrm{CO_3^{2-}}, \mathrm{K^+}, \mathrm{HCO_3^-}, \mathrm{H^+}. \tag{3.18}$$

The fixed potential at the OHP is given by:

$$\Phi_{OHP} = E_{App}. \tag{3.19}$$

Bulk Electrolyte/Pore Interface (B5)

The flux of species i depends on the concentration difference between interface B5 and the bulk electrolyte:

$$J_i^{B5} = \kappa_{B5_i}(C_{i_{B5}} - C_{i_{BULK}}), \qquad i = CO_2, CO, H_2, OH^-, {CO_3}^{2-}, K^+, {HCO_3}^-, H^+. \tag{3.20}$$

Here, $C_{i_{B5}}$ and $C_{i_{BULK}}$ are the concentrations of species i at the interface B5 and the bulk of electrolyte, respectively. The bulk concentrations of all the species except the products (CO and H_2), are calculated by solving the rate of reactions associated with eqs. 3.1-3.3 at steady state. The product species will leave the liquid phase immediately due to their low solubility. To facilitate the simulations, an arbitrarily low value is set for the product species in the bulk of electrolyte. A more sophisticated approach can be coupled with the present model to simulate the mass transfer of these species into the bulk electrolyte. However, this would not influence the results presented in this study because these product species do not take part in the homogeneous reactions and they do not influence the electric field since they are charge neutral [29]. κ_{B5_i} is the convective mass transfer coefficient of species i, calculated as:

$$\kappa_{B5_i} = \frac{D_i}{L_c}\left(1.017\frac{2L_c}{L_{cross}}\mathrm{ReSc}_i\right)^{\frac{1}{3}}. \tag{3.21}$$

L_c is the length of the catalyst layer over which the electrolyte flows. L_{cross} is the width of the flow channel. Re and Sc represent the Reynolds and the Schmidt numbers, respectively, given by:

$$\mathrm{Re} = \frac{\rho_{elec} L_c V_{elec}}{A_{cross}\mu_{elec}}, \tag{3.22}$$

$$\mathrm{Sc}_i = \frac{\mu_{elec}}{\rho_{elec} D_i}. \tag{3.23}$$

A_{cross} is the electrolyte flow cross-section. V_{elec} is the flow rate and μ_{elec} is the viscosity of the electrolyte. The potential at the boundary B5 is set to 0:

$$\Phi_{B5} = 0. \tag{3.24}$$

Other Boundaries (B3, B4, B6)

For the remaining boundaries (B3, B4, B6), zero flux is assumed for the species' transport:

$$J_i^{B3,B4,B6} = 0. \tag{3.25}$$

For the reservoir boundary B3, a fixed applied potential, similar to that at OHP (B2), is adopted in order to avoid a discontinuity in the potential at the interface between boundaries B2 and B3. Such a boundary condition is consistent with the properties of a conducting electrode.

$$\Phi_{B3} = E_{App}. \tag{3.26}$$

For the remaining two boundaries (B4, B6), zero electric field is assumed:

$$\nabla\Phi = 0. \tag{3.27}$$

Numerical Solver Details

All concentrations will initially (t=0) be at their bulk values throughout the domain. The OHP potential is referenced with respect to the potential of zero charge (pzc) and ranges from -0.12 to -0.30 V vs pzc. The finite element package FEniCS is used to solve the weak formulation of the non-linear SMPNP equations. Temporal discretizations are carried out using the backward Euler scheme. A time step of 10^{-7} s is used until a steady state is attained. For the presented system, this time will be in milliseconds. Variable mesh spacing is used in the simulation domain, with finer mesh near the high-potential boundaries. To overcome instability, the potential values at boundaries B2 and B3 are increased in a step-wise manner. In the absence of a stepwise potential increase, extremely sharp potential gradients will be present in the initial stages of the simulation. A very small initial time step of $\approx 10^{-9}$ s (corresponding to the capacitative charging of EDL) would then be required to resolve the evolution of the potential profile.

3.3. RESULTS AND DISCUSSION

In this section, we quantify the dependence of the local reaction environment on changes in key control parameters such as applied potential, bulk electrolyte concentration and pore radius. All radial profiles are evaluated at a distance of 25 nm from the gas/liquid interface B1.

Influence of Applied Potential

Fig. 3.2a represents the radial profile of CO_2 inside the nanopore against a range of applied potentials (-0.12 to -0.30 V vs pzc). The potential is applied at the OHP. It can be observed that the concentration of CO_2 remains constant from the centre of the pore (2.5 nm) up to ≈1 nm away from the OHP, but decreases from this point onward. The radial

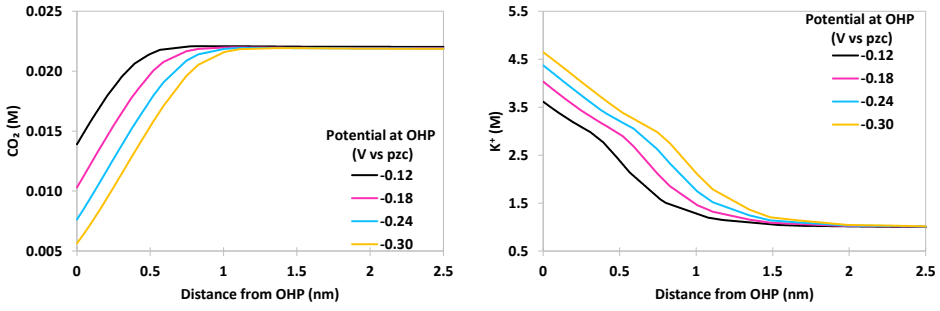

(a) (b)

Figure 3.2: Radial variation of concentrations as a result of changing OHP potential (vs pzc) for an Ag (111) catalytic nanopore (R=2.5 nm, L=45 nm) in a 1.0 M $KHCO_3$ solution at I_{ECSA}= 2 mAcm^{-2} and 1 bar CO_2 pressure. (a) CO_2, (b) K^+.

drop in the CO_2 concentration is due to the presence of a dense layer of K^+ ions near the OHP. Electromigration drives K^+ ions to form a concentrated diffuse layer beyond the

OHP. This imposes strong steric hindrances onto the CO_2 molecules based on eq. 3.4, leading to a drop in CO_2 concentration near the electrode. Without these steric effects, pore models fail to capture the large radial variation of the CO_2 concentration [22, 46]. This trend becomes even more pronounced at increasing applied potentials due to the fact that more K^+ ions are now attracted towards the OHP (fig. 3.2b). This behaviour was predicted by Bohra et. al. [29] for a similar model; however, they did not observe an influence of steric effects in their pore model because their model was limited to very low applied potentials (≈25 mV vs pzc).

Fig. 3.3 depicts the pH profile along the radial direction. A decline in the pH is observed

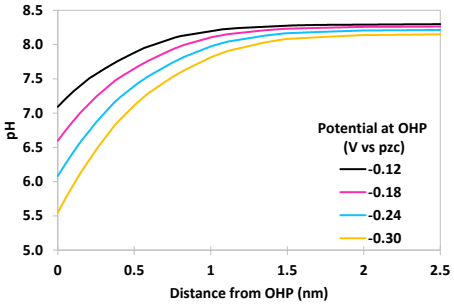

Figure 3.3: Radial variation of pH for different OHP potentials (vs pzc) for an Ag (111) catalytic nanopore (R=2.5 nm, L=45 nm) in a 1.0 M $KHCO_3$ solution at I_{ECSA}= 2 mAcm^{-2} and 1 bar CO_2 pressure.

as we move toward the reaction plane. This decline is caused primarily by the increased presence of H^+ ions in the vicinity of the OHP under negative applied potential. Furthermore, OH^- ions are electrostatically repelled from the reaction plane, causing a drop in the local pH near the reactive surface. This effect increases with applied potential. Notably, CO_2ER studies often report an increase in local pH when going from the bulk towards the surface due to the production of OH^- ions [18, 32].

We have seen that steric effects play an important role in the EDL at high applied surface potential. This also affects the interfacial pH. In the absence of steric effects (i.e. point charges assumption), there will be no limitation on the possible concentration of attracted H^+ ions near the OHP, leading to an underestimated pH value at high applied potentials. It is also worth mentioning that the pH behaviour in fig. 3.3 is based on a fixed current density value. In reality, the current density depends on the applied potential and is described by Butler-Volmer type kinetic expressions. A more sophisticated, microkinetic model might be necessary to accurately account for such reactions[43]. A higher current density results in a greater production rate of OH^- as shown in fig. 3.4. This would not change the trend of local pH within the EDL as the potential changes because the repulsion of OH^- ions is the dominating factor.

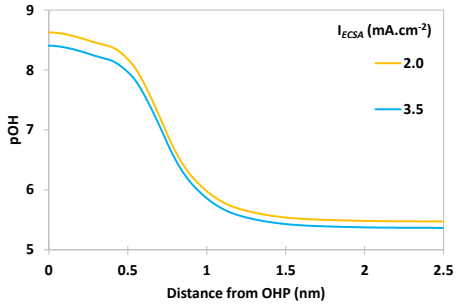

Figure 3.4: Radial variation of pOH as a result of changing I_{ECSA} for an Ag (111) catalytic nanopore (R=2.5 nm, L=45 nm) in a 1.0 M $KHCO_3$ solution at a fixed Φ_{OHP}=-0.24 V vs pzc and 1 bar CO_2 pressure.

Influence of Bulk Electrolyte Concentration

Fig. 3.5a shows the influence of bulk electrolyte concentration on the radial concentration profile of CO_2. Increasing the electrolyte concentration from 0.01 M to 0.50 M $KHCO_3$ reduces the CO_2 concentration at the reaction plane. As shown in fig. 3.2a, the interfacial CO_2 concentration decreases due to steric effects as more K^+ ions accumulate near the electrode (fig. 3.5b). It can also be observed that beyond a certain distance from the OHP, the influence of the electric field and thus steric effects diminish and the concentrations reach their bulk values.

Apart from the steric effects, the electrolyte also affects the CO_2 concentration by reduc-

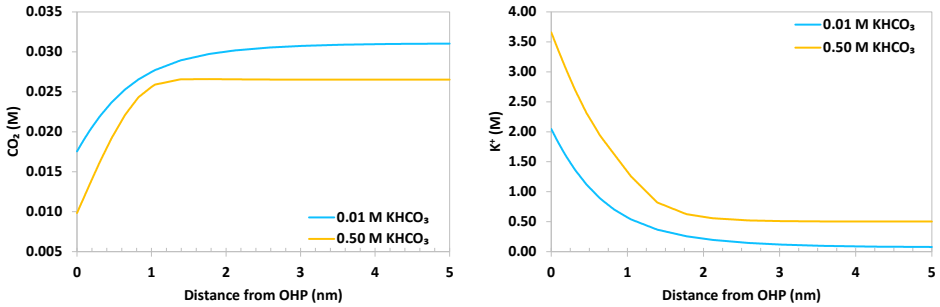

(a) (b)

Figure 3.5: Radial concentration profiles for different electrolyte concentrations, for an Ag (111) catalytic nanopore (R=5 nm, L=45 nm), under Φ_{OHP}= -0.24 V vs pzc at I_{ECSA}= 2 mAcm^{-2} and 1 bar CO_2 pressure.

ing the dissolution of the incoming CO_2 at the gas/liquid interface. A higher electrolyte concentration would result in a lower CO_2 mass transfer rate across the B1 boundary based on the Sechenov correction of Henry's law. The CO_2 mass transfer rate at B1 is calculated using eq. 3.12, where $C^{B1}_{CO_2}$ is evaluated at every time step using the Sechenov-corrected Henry's law (Appendix D). This relation depends on the ionic concentration of

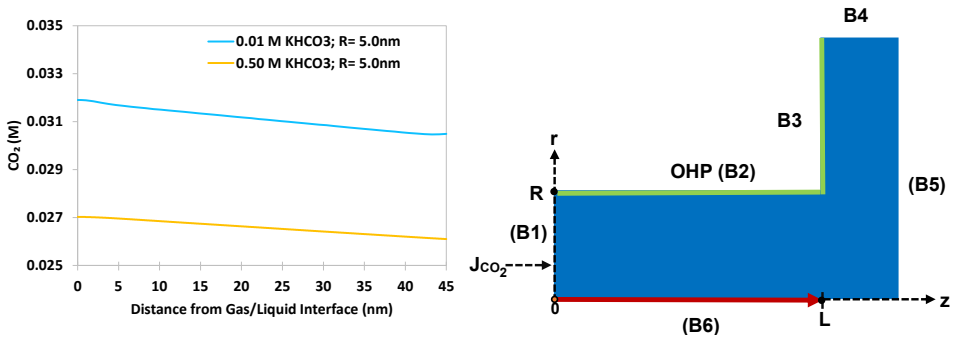

(a) (b)

Figure 3.6: Longitudinal concentration profile of CO_2 taken at the axisymmetric axis (B6) as a result of changing electrolyte concentration, for an Ag (111) catalytic nanopore (R=5 nm, L=45 nm), under Φ_{OHP}= -0.24 V vs pzc at I_{ECSA}= 2 mAcm^{-2} and 1 bar CO_2 pressure.

electrolytic species at the B1 interface. A higher ionic presence in the pore reduces the value of $C^{B1}_{CO_2}$, which in turn reduces the mass transfer rate of CO_2 across the interface. In order to quantify this effect, we show the longitudinal variation of CO_2 concentration (fig. 3.6). We take the measurement at the axisymmetry boundary (solid red line in fig. 3.6b), which is the farthest away from the applied potential source. As a result, the steric effects would be the least at this boundary. We can observe that there is a linear drop in the CO_2 concentration from the gas/liquid interface at z=0 nm until z=45 nm for both electrolyte concentrations. This trend follows from a balance between the rate of CO_2 consumption and the rate at which CO_2 dissolves and diffuses back into the pore. The concentration of CO_2 at the gas/liquid interface already shows a significant difference for the two electrolyte concentrations used. The CO_2 concentration at this point (gas/liquid interface (z=0) and axisymmetry axis (r=0)) primarily depends on the ionic concentration inside the pore via the mass transfer condition in eq. 3.12. Thus, for a high electrolyte concentration solution, we end up with an overall lower CO_2 concentration inside the pore.

Influence of Pore Diameter

The influence of pore size on the radial CO_2 concentration profile can be seen in Fig. 3.7a. The radial profile is evaluated at a distance of z= 25 nm from the gas/liquid interface. Pore size has a negligible effect on CO_2 concentration at the reaction plane. This is because CO_2 concentration at high applied potentials largely depends on the concentration of K^+ ions. For a fixed value of Φ_{OHP} and bulk electrolyte concentration, the K^+ ions reach a concentration at the OHP that is independent of the pore size (fig. 3.7b). However, moving away from the reaction plane, the K^+ concentration profiles for different pore sizes diverge.

The K^+ concentration in the centre of the pore increases when going from a larger pore radius of 10 nm to a smaller pore radius of 1 nm (fig. 3.7b). This is because the mean po-

tential inside the pore relative to the bulk potential is higher for a smaller pore compared to a larger-sized pore (Appndix B fig.B.2). This results in a stronger pull for K^+ ions from the bulk of electrolyte into the pore. This in turn lowers CO_2 concentration values. We can observe this behaviour in fig. 3.7a, where a smaller pore leads to a smaller mean CO_2 concentration inside the pore. For a pore radius of 5 nm and beyond, the concentration profiles become largely independent of the pore size. This is because the electric field gets screened near the reaction plane, as shown in Appendix B fig. B.2. We can see that bulk potential values (=0 V vs pzc) are reached at the central axis of the pore (r=0). This is why a similar concentration of K^+ is observed at the centre of both the 5 and 10 nm pores. The higher mean cation concentrations in larger pores, in turn, influence the homogeneous reactions and the average pH inside the pore.

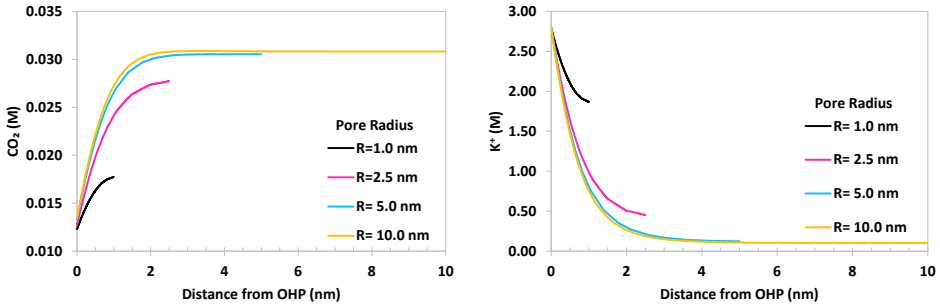

(a) (b)

Figure 3.7: Radial variation of concentrations as a result of changing pore size for an Ag (111) catalytic nanopore in a 0.1 M $KHCO_3$ solution under Φ_{OHP}=-0.24 V vs pzc, I_{ECSA} of 2 mAcm^{-2} and 1 bar CO_2 pressure.

Fig. 3.8a shows the radial variation of pH for various pore sizes in a 0.5 M $KHCO_3$ solution. Based purely on the idea of smaller pores having a higher mean potential, the expected trend in pH should be opposite to the trend in K^+ concentration shown in fig. 3.7b. A higher mean potential inside the pore should result in a higher concentration of H^+ ions, thus a lower pH. This trend can indeed be observed in fig. 3.8a, when looking at the pores of at least 2.5 nm radius. These pores show a slight increase in the interfacial pH with an increasing pore size. However, the pore of 1 nm radius completely deviates from this trend by showing a higher interfacial pH than each of the larger pores. This is because, besides the mean potential, there are several other competing phenomena that influence the overall makeup of the pH. For example, a smaller pore would have a lower mean CO_2 concentration (fig. 3.7a), this would lead to a decrease in bicarbonate production and consequently a decrease in the consumption of OH^- ions (eq. 3.1), making the pore more basic. Furthermore, a smaller pore would have a higher surface-to-volume ratio; hence, for a fixed I_{ECSA} value, a smaller pore would have a higher mean OH^- concentration. Another factor to consider is that the potential drop from the OHP to the center of the pore is extremely small for the pore of 1 nm radius. Consequently, this would result in a more basic pore via the decreased overall pull for H^+ ions towards the reaction plane.

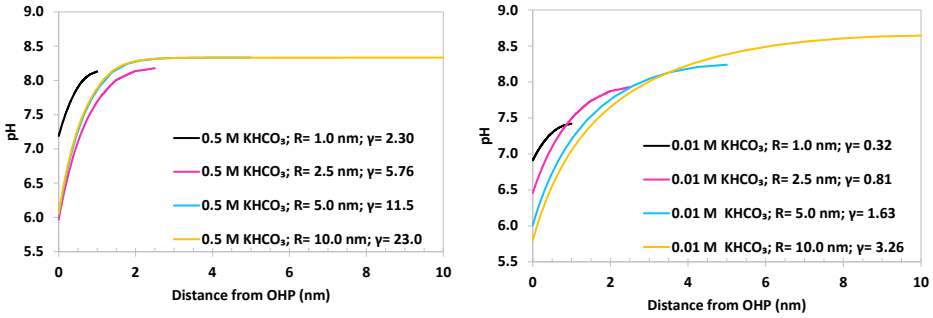

(a) (b)

Figure 3.8: Radial variation of pH as a result of changing pore size for an Ag (111) catalytic nanopore under Φ_{OHP}=-0.24 V vs pzc, I_{ECSA} of 2 mAcm^{-2} and 1 bar CO_2 pressure. (a) 0.5 M $KHCO_3$ solution, (b) 0.01 M $KHCO_3$ solution.

This behaviour can be modulated by the ratio:

$$\gamma = \frac{R}{\lambda_{Debye}}. \tag{3.28}$$

Here, R is the radius of the pore (upto the OHP) and λ_{Debye} is the Debye length, defined as:

$$\lambda_{Debye} = \sqrt{\frac{\epsilon_0 \epsilon_r^0 k_B T}{2\epsilon_0^2 C_{elec} N_A}}. \tag{3.29}$$

k_B is Boltzmann's constant and C_{elec} is the concentration of the electrolyte. When γ is $\approx$ 2.3 (for 1 nm pore in figure. 3.8a) or less, the influence of the mean potential is expected to be less relevant compared to the counteracting phenomena discussed above, resulting in pores becoming more basic as seen in the case of the 1 nm pore in fig. 3.8a. To test this theory, we lower the electrolyte concentration from 0.5 M to 0.01 M $KHCO_3$ (fig. 3.8b). This increases the Debye length from $\lambda_{Debye} \approx 0.43$ nm to $\lambda_{Debye} \approx 3$ nm and consequently decreases γ. As a result, pores of radius 2.5 nm and 5 nm, both show a more basic pH trend near the reaction plane as compared to the 10 nm pore. Considering the importance of the local pH in maintaining a favourable reaction environment inside the pore, the ratio γ can provide crucial insight into the optimal design of a GDE. One can regulate the ratio by varying either the pore size or the ionic strength of the system, in order to get a desired pH trend inside the catalyst layer.

The presented GDE model involves multiscale mass transport coupled with homogeneous and heterogeneous reactions. Our pore-scale model describes the mass transport in the pore subject to imposed reaction rates. It can be used to predict the local environment inside the EDL of the pore. This model could be coupled to descriptions of the larger length scales as well as an explicit description of the molecular transport and reaction processes on the smaller scales. The pore model can be seamlessly integrated with a gas transport model such as convection and mixed average diffusion model [18, 22] to account for the GDL. The GDL model will inform the amount of gaseous species at the

gas/liquid interface (eqs. 3.11-3.12).
The 2D pore-scale model can also be coupled to a microkinetic model to [43, 47] to quantify the influence of GDE structural properties on faradaic efficiencies of the desired products. If the rate-determining steps of the CO_2ER reactions are known, then a simplified Frumkin-corrected Tafel relation can also be used to get an accurate estimation of the current densities [31, 48–51]. Currently, the model does not account for the specific adsorption of ions on the surface of the catalyst. This is theorized to have an impact on the concentration and potential profiles [27, 52, 53]. Even though the continuum hypothesis does hold for the smallest pore size used in this work (which has a diameter of 2 nm, excluding the Stern layer) [54], the consequence of not being able to capture the exact molecular effects at the surface, including ion-ion correlations, may be substantial in this smallest pore due to the large surface-to-volume ratio. A coupled approach with molecular dynamics simulation should be developed to inform the continuum scale transport models.

3.4. CONCLUSION

This work presents a 2D GDE nanopore model for CO_2ER based on a set of size-modified PNP equations. Traditionally, GDE models for CO_2ER tend to ignore the formation of the EDL and hence fail to accurately describe the local environment such as concentration profiles and pH inside the pore. Our approach overcomes this limitation by incorporating the EDL region near the reaction plane.
The study was performed based on Ag(111) catalyst in contact with a $KHCO_3$ solution. Our model predicts a significant drop in the CO_2 concentration near the reaction plane due to the high local concentration of K^+ ions. This effect increases with applied cathodic potentials. Most of the literature on GDE models for CO_2ER fail to account for this drop that is induced by steric effects. We also observed a drop in pH going from the centre of the pore to the reaction plane. This is because the region near the OHP has a stronger electric field and thus a stronger pull for H^+ ions relative to the centre of the pore. The attraction of H^+ ions inside the pore and repulsion for OH^- ions from the walls of the pore increase with cathodic potentials, making the pore more acidic at higher potentials. The CO_2 concentration inside the pore also drops with increased electrolyte concentration due to both increased steric effects as well as due to the decreased dissolution of CO_2 in the liquid phase. This decrease was quantified using the Sechenov-corrected Henry's law.
The model also describes the influence of pore size on the local environment. Four different pore sizes were simulated. The difference in CO_2 and cation concentration at the reaction plane is found to be independent of the pore size, while the smaller pores showed a higher mean cation concentration relative to a larger pore due to a greater potential difference between the pore and the bulk of electrolyte. This increases the steric repulsion for CO_2 and thus a decreased mean concentration is observed for CO_2 in a smaller pore. The effect of pore size on the pH is, however, not entirely dictated by the mean potential as several competing phenomena can influence the local pH. For example, even if the potential value at any given point is high in a smaller pore, making the pore more acidic, the carbonate balance and increased surface-to-volume ratio would impart a more basic character to the pore. This is why a pore radius of 1 nm shows a more basic pH near the reaction plane compared to larger pores. The γ factor, which is the ratio between the pore

radius and the Debye length, can be used to predict the pH trend. Below the threshold value of 2.3, even pores of 2.5 and 5 nm radius became more basic near the reaction plane than the larger 10 nm pore. This factor can be extremely useful for researchers focusing on the optimal structural design of the pore as it allows them to regulate the pH trend inside the catalyst layer of a CO_2ER process.
The cost-effective methodology presented in this work allows us to gain key insights into the local environment within a nanopore and can be used to make informed decisions regarding the inputs for larger pore network models.

REFERENCES

[1] Wilson A. Smith, Thomas, David A. Vermaas, and Hans Geerlings. "Pathways to Industrial-Scale Fuel Out of Thin Air from CO_2 Electrolysis". In: *Joule* 3 (8 Aug. 2019), pp. 1822–1834. ISSN: 25424351. DOI: 10.1016/j.joule.2019.07.009.

[2] Zhifei Yan, Jeremy L. Hitt, John A. Turner, and Thomas E. Mallouk. "Renewable electricity storage using electrolysis". In: *Proceedings of the National Academy of Sciences of the United States of America* 117 (23 June 2020), pp. 12558–12563. ISSN: 10916490. DOI: 10.1073/pnas.1821686116.

[3] Xu Lu, Dennis Y.C. Leung, Huizhi Wang, Michael K.H. Leung, and Jin Xuan. "Electrochemical Reduction of Carbon Dioxide to Formic Acid". In: *ChemElectroChem* 1 (5 2014), pp. 836–849. ISSN: 21960216. DOI: 10.1002/celc.201300206.

[4] Estela Ruiz-López, Jesús Gandara-Loe, Francisco Baena-Moreno, as Ramirez Reina, and José Antonio Odriozola. "Electrocatalytic CO_2 conversion to C2 products: Catalysts design, market perspectives and techno-economic aspects". In: *Renew. Sust. Energ. Rev.* 161 (2022), p. 112329. ISSN: 1364-0321. DOI: https://doi.org/10.1016/j.rser.2022.112329.

[5] Devin T. Whipple and Paul J. A. Kenis. "Prospects of CO_2 Utilization via Direct Heterogeneous Electrochemical Reduction". In: *J. Phys. Chem. Lett.* 1 (24 2010), pp. 3451–3458. DOI: doi:10.1021/jz1012627.

[6] Shreyas Niphadkar, Praful Bagade, and Shadab Ahmed. "Bioethanol production: insight into past, present and future perspectives". In: *Biofuels* 9 (2018), pp. 229–238. DOI: doi:10.1080/17597269.2017.1334338.

[7] Jonathan Albo and Angel Irabien. "Cu_2O-loaded gas diffusion electrodes for the continuous electrochemical reduction of CO_2 to methanol". In: *J. Catal.* 343 (2016), pp. 232–239. DOI: https://doi.org/10.1016/j.jcat.2015.11.014.

[8] Matthias Heßelmann, Berinike Clara Bräsel, Robert Gregor Keller, and Matthias Wessling. "Simulation-based guidance for improving CO_2 reduction on silver gas diffusion electrodes". In: *Electrochemical Science Advances* 3 (1 Feb. 2023), p. 2100160. ISSN: 26985977. DOI: 10.1002/elsa.202100160.

[9] Justin C. Bui, Eric W. Lees, Lalit M. Pant, Iryna V. Zenyuk, Alexis T. Bell, and Adam Z. Weber. "Continuum Modeling of Porous Electrodes for Electrochemical Synthesis". In: *Chemical Reviews* 122 (12 June 2022), pp. 11022–11084. ISSN: 15206890. DOI: 10.1021/acs.chemrev.1c00901.

[10] Karan Malik, Biju Mani Rajbongshi, and Anil Verma. "Syngas production from electrochemical reduction of CO_2 at high current density using oxide derived Zn/Cu nanocomposite". In: *J. CO2 Util.* 33 (2019), pp. 311–319. DOI: https://doi.org/10.1016/j.jcou.2019.06.020..

[11] Jonathan Albo, Daniel Vallejo, Garikoitz Beobide, Oscar Castillo, Pedro Castaño, and Angel Irabien. "Copper-Based Metal–Organic Porous Materials for CO_2 Electrocatalytic Reduction to Alcohols". In: *ChemSusChem* 10 (2017), pp. 1100–1109. DOI: https://doi.org/10.1002/cssc.201600693.

[12] Cao-Thang Dinh, Thomas, Md Golam Kibria, Ali Seifitokaldani, Christine M Gabardo, F Pelayo García de Arquer, Amirreza Kiani, Jonathan P Edwards, Phil De Luna, Oleksandr S Bushuyev, Chengqin Zou, Rafael Quintero-Bermudez, Yuanjie Pang, David Sinton, and Edward H Sargent. "CO_2 electroreduction to ethylene via hydroxide-mediated copper catalysis at an abrupt interface". In: *Science* 360 (2018), pp. 783–787. DOI: https://doi.org/10.1126/science.aas9100.

[13] Sumit Verma, Xun Lu, Sichao Ma, Richard I. Maseld, and Paul J. A. Kenis. "The effect of electrolyte composition on the electroreduction of CO_2 to CO on Ag based gas diffusion electrodes." In: *Phys. Chem. Chem. Phys.* 18 (2016), pp. 7075–7084. DOI: https://doi.org/10.1039/C5CP05665A.

[14] Charles Delacourt, Paul L. Ridgway1, John B. Kerr, and John Newman. "Design of an Electrochemical Cell Making Syngas ($CO+H_2$) from CO_2 and H_2O Reduction at Room Temperature." In: *Journal of The Electrochemical Society* 155 (2008), B42. DOI: DOI10.1149/1.2801871.

[15] Jingjie Wu, Sichao Ma, Jing Sun, Jake I. Gold, ChandraSekhar Tiwary, Byoungsu Kim, Lingyang Zhu, Nitin Chopra, Ihab N. Odeh, Robert Vajtai, Aaron Z. Yu, Raymond Luo, Jun Lou, Guqiao Ding, Paul J. Kenis, and Pulickel M. Ajayan. "A metal-free electrocatalyst for carbon dioxide reduction to multi-carbon hydrocarbons and oxygenates". In: *Nature Communications* 7 (2016), p. 13869. DOI: https://doi.org/10.1038/ncomms13869.

[16] Christine M. Gabardo, Ali Seifitokaldani, Jonathan P. Edwards, Cao-Thang Dinh, Thomas, Md Golam Kibria, Colin P. O'Brien, Edward H. Sargent ORCID, and David Sinton. "Combined high alkalinity and pressurization enable efficient CO_2 electroreduction to CO". In: *Energy and Environmental Science* 11 (2018), pp. 2531–2539. DOI: https://doi.org/10.1039/C8EE01684D.

[17] Jing-Jing Lv, Matthew Jouny, Wesley Luc, Wenlei Zhu, Jun-Jie Zhu, and Feng Jiao. "A Highly Porous Copper Electrocatalyst for Carbon Dioxide Reduction". In: *Advanced Materials* 30 (2018), p. 1803111. DOI: https://doi.org/10.1002/adma.201803111.

[18] Lien-Chun Weng, Alexis T. Bell, and Adam Z. Weber. "Modeling gas-diffusion electrodes for CO_2 reduction". In: *Phys. Chem. Chem. Phys.* 20 (2018), pp. 16973–16984. DOI: https://doi.org/10.1039/C8CP01319E.

[19] Ying Chuan Tan, Kelvin Berm Lee, Hakhyeon Song, and Jihun Oh. "Modulating Local CO_2 Concentration as a General Strategy for Enhancing C C coupling in CO_2 Electroreduction". In: *Joule* 4 (2020), pp. 1104–1120. DOI: https://doi.org/10.1016/j.joule.2020.03.013.

[20] Luisa C. Brée, Matthias Wessling, and Alexander Mitsos. "Modeling and Simulating Electrochemical Reduction of CO_2 in a Microfluidic Cell". In: *Computers and Chemical Engineering* 139 (2020), p. 106890. DOI: https://doi.org/10.1016/j.compchemeng.2020.106890.

[21] Yosra Kotb, Seif-Eddeen K. Fateen, Jonathan Albo, and Ibrahim Ismail. "Modeling of a Microfluidic Electrochemical Cell for the Electro-Reduction of CO_2 to CH_3OH". In: *J. Electrochem. Soc.* 164 (2017), E391. DOI: 10.1149/2.0741713jes.

[22] Recep Kas, Andrew G. Star, Kailun Yang, Tim Van Cleve, Kenneth C. Neyerlin, and Wilson A. Smith. "Along the Channel Gradients Impact on the Spatioactivity of Gas Diffusion Electrodes at High Conversions during CO_2 Electroreduction". In: *ACS Sustainable Chemistry and Engineering* 9 (3 Jan. 2021), pp. 1286–1296. ISSN: 21680485. DOI: 10.1021/acssuschemeng.0c07694.

[23] Omnia A. El-Shafie, Rehab M. El-Maghraby, Jonathan Albo, Seif-Eddeen K. Fateen, and Amr Abdelghany. "Modeling and Numerical Investigation of the Performance of Gas Diffusion Electrodes for the Electrochemical Reduction of Carbon Dioxide to Methanol". In: *Ind. Eng. Chem. Res.* 59 (2020), pp. 20929–20942. DOI: https://doi.org/10.1021/acs.iecr.0c02358.

[24] Joseph W. Blake, Vojtěch Konderla, Lorenz M. Baumgartner, David A. Vermaas, Johan T. Padding, and J. W. Haverkort. "Inhomogeneities in the Catholyte Channel Limit the Upscaling of CO_2 Flow Electrolysers". In: *ACS Sustainable Chemistry and Engineering* 11 (7 Feb. 2023), pp. 2840–2852. ISSN: 21680485. DOI: 10.1021/acssuschemeng.2c06129.

[25] Gastón O. Larrazábal, Antonio J. Martín, and Javier Pérez-Ramírez. "Building Blocks for High Performance in Electrocatalytic CO2 Reduction: Materials, Optimization Strategies, and Device Engineering". In: *Journal of Physical Chemistry Letters* 8 (16 Aug. 2017), pp. 3933–3944. ISSN: 19487185. DOI: 10.1021/acs.jpclett.7b01380.

[26] Min Liu, Yuanjie Pang, Bo Zhang, Phil De Luna, Oleksandr Voznyy, Jixian Xu, Xueli Zheng, Cao Thang Dinh, Fengjia Fan, Changhong Cao, F. Pelayo García De Arquer, Tina Saberi Safaei, Adam Mepham, Anna Klinkova, Eugenia Kumacheva, Tobin Filleter, David Sinton, Shana O. Kelley, and Edward H. Sargent. "Enhanced electrocatalytic CO_2 reduction via field-induced reagent concentration". In: *Nature* 537 (7620 Aug. 2016), pp. 382–386. ISSN: 14764687. DOI: 10.1038/nature19060.

[27] Divya Bohra, Jehanzeb H. Chaudhry, Thomas, Evgeny A. Pidko, and Wilson A. Smith. "Modeling the electrical double layer to understand the reaction environment in a CO_2 electrocatalytic system". In: *Energy and Environmental Science* 12 (11 2019), pp. 3380–3389. ISSN: 17545706. DOI: 10.1039/c9ee02485a.

[28] Joaquin Resasco, Leanne D. Chen, Ezra Clark, Charlie Tsai, Christopher Hahn, Thomas F. Jaramillo, Karen Chan, and Alexis T. Bell. "Promoter Effects of Alkali Metal Cations on the Electrochemical Reduction of Carbon Dioxide". In: *Journal of the American Chemical Society* 139 (32 Aug. 2017), pp. 11277–11287. ISSN: 15205126. DOI: 10.1021/jacs.7b06765.

[29] Divya Bohra, Jehanzeb H Chaudhry, Thomas Burdyny, Evgeny A Pidko, and Wilson A Smith. "Mass transport in catalytic pores of GDE-based CO_2 electroreduction systems". In: *ChemRxiv* (2020). DOI: https://doi.org/10.26434/chemrxiv.13073348.v1.

[30] Javed Hussain, Hannes Jónsson, and Egill Skúlason. "Calculations of Product Selectivity in Electrochemical CO_2 Reduction". In: *ACS Catal.* 8(6) (2018), pp. 5240–5249. DOI: https://doi.org/10.1021/acscatal.7b03308.

[31] Esaar Naeem Butt, Johan T. Padding, and Remco Hartkamp. "Size-modified Poisson-Nernst-Planck approach for modeling a local electrode environment in CO_2 electrolysis". In: *Sustainable Energy and Fuels* 7 (1 Nov. 2023), pp. 144–154. ISSN: 23984902. DOI: 10.1039/d2se01262f.

[32] J.W. Blake, J.T. Padding, and J.W. Haverkort. "Analytical modelling of CO_2 reduction in gas-diffusion electrode catalyst layers". In: *Electrochim. Acta* 393 (2021), p. 138987. ISSN: 0013-4686. DOI: https://doi.org/10.1016/j.electacta.2021.138987.

[33] Martin Z Bazant, Mustafa Sabri Kilic, Brian D Storey, and Armand Ajdari. "Towards an understanding of induced-charge electrokinetics at large applied voltages in concentrated solutions." In: *Advances in colloid and interface science* 152 (1-2 Nov. 2009), pp. 48–88. ISSN: 1873-3727 (Electronic). DOI: 10.1016/j.cis.2009.10.001.

[34] Mustafa Sabri Kilic, Martin Z. Bazant, and Armand Ajdari. "Steric effects in the dynamics of electrolytes at large applied voltages. I. Double-layer charging". In: *Physical Review E - Statistical, Nonlinear, and Soft Matter Physics* 75 (2 2007), pp. 1–16. ISSN: 15393755. DOI: 10.1103/PhysRevE.75.021502.

[35] Mustafa Sabri Kilic, Martin Z. Bazant, and Armand Ajdari. "Steric effects in the dynamics of electrolytes at large applied voltages. II. Modified Poisson-Nernst-Planck equations". In: *Physical Review E - Statistical, Nonlinear, and Soft Matter Physics* 75 (2 Feb. 2007), p. 021502. ISSN: 15393755. DOI: 10.1103/PhysRevE.75.021503.

[36] Martin Z. Bazant, Kevin T. Chu, and B. J. Bayly. "Current-voltage relations for electrochemical thin films". In: *SIAM Journal on Applied Mathematics* 65 (5 2005), pp. 1463–1484. ISSN: 00361399. DOI: 10.1137/040609938.

[37] Antoine Bonnefont, Francçoise Argoul, and Martin Z. Bazant. "Analysis of diffuse-layer effects on time-dependent interfacial kinetics". In: *Journal of Electroanalytical Chemistry* 500 (1-2 2001), pp. 52–61. ISSN: 00220728. DOI: 10.1016/S0022-0728(00)00470-8.

[38] Hainan Wang, Alexander Thiele, and Laurent Pilon. "Simulations of Cyclic Voltammetry for Electric Double Layers in Asymmetric Electrolytes: A Generalized Modified Poisson–Nernst–Planck Model". In: *The Journal of Physical Chemistry C* 117 (36 Sept. 2013), pp. 18286–18297. ISSN: 1932-7447. DOI: 10.1021/jp402181e.

[39] Benzhuo Lu and Y. C. Zhou. "Poisson-Nernst-Planck equations for simulating biomolecular diffusion-reaction processes II: Size effects on ionic distributions and diffusion-reaction rates". In: *Biophysical Journal* 100 (10 May 2011), pp. 2475–2485. ISSN: 15420086. DOI: 10.1016/j.bpj.2011.03.059.

[40] Kherim Willems, Dino Ruic, Florian L.R. Lucas, Ujjal Barman, Niels Verellen, Johan Hofkens, Giovanni Maglia, and Pol Van Dorpe. "Accurate modeling of a biological nanopore with an extended continuum framework". In: *Nanoscale* 12 (32 Aug. 2020), pp. 16775–16795. ISSN: 20403372. DOI: 10.1039/d0nr03114c.

[41] J. B. Hasted, D. M. Ritson, and C. H. Collie. "Dielectric Properties of Aqueous Ionic Solutions. Parts I and II". In: *The Journal of Chemical Physics* 16 (1 Jan. 1948), pp. 1–21. ISSN: 0021-9606. DOI: 10.1063/1.1746645. URL: http://aip.scitation.org/doi/10.1063/1.1746645.

[42] John Bockris and Amulya Reddy. *Modern Electrochemistry*. 2nd. Springer New York, NY, 1998.

[43] Stefan Ringe, Carlos G. Morales-Guio, Leanne D. Chen, Meredith Fields, Thomas F. Jaramillo, Christopher Hahn, and Karen Chan. "Double layer charging driven carbon dioxide adsorption limits the rate of electrochemical carbon dioxide reduction on Gold". In: *Nature Communications* 11 (1 Dec. 2020), p. 33. ISSN: 20411723. DOI: 10.1038/s41467-019-13777-z.

[44] S Weisenberger and A Schumpe. "Estimation of Gas Solubilities in Salt Solutions at Temperatures from 273 K to 363 K". In: *AIChE Journal* 42 (1 1996), pp. 298–300.

[45] Thomas Burdyny, Percival J. Graham, Yuanjie Pang, Cao-Thang Dinh, Min Liu, Edward H. Sargent, and David Sinton. "Nanomorphology-Enhanced Gas-Evolution Intensifies CO_2 Reduction Electrochemistry". In: *ACS Sustainable Chemistry and Engineering* 5 (5 May 2017), pp. 4031–4040. DOI: 10.1021/acssuschemeng.7b00023.

[46] Thomas Moore, Xiaoxing Xia, Sarah E. Baker, Eric B. Duoss, and Victor A. Beck. "Elucidating Mass Transport Regimes in Gas Diffusion Electrodes for CO2 Electroreduction". In: *ACS Energy Letters* 6(10) (2021), pp. 3600–3606. DOI: https://doi.org/10.1021/acsenergylett.1c01513.

[47] Xinwei Zhu, Jun Huang, and Michael Eikerling. "Electrochemical CO_2 Reduction at Silver from a Local Perspective". In: *ACS Catalysis* 11 (23 Dec. 2021), pp. 14521–14532. ISSN: 21555435. DOI: 10.1021/acscatal.1c04791.

[48] A Frumkin. "wasserstoffuberspannung und struktur der doppelschicht." In: *Zeitschrift für physikalische Chemie* 164 (1 1933), pp. 121–133.

[49] Roger Parsons. "Structure of the electrical double layer and its influence on the rates of electrode reactions". In: *Advances in Electrochem. Electrochem. Eng.* (1 1961), pp. 1–64.

[50] Marco Rossi, Thomas Wallmersperger, Stefan Neukamm, and Kathrin Padberg-Gehle. “Modeling and Simulation of Electrochemical Cells under Applied Voltage”. In: *Electrochimica Acta* 258 (2017), pp. 241–254. ISSN: 00134686. DOI: 10.1016/j.electacta.2017.10.047. URL: http://dx.doi.org/10.1016/j.electacta.2017.10.047.

[51] P. M. Biesheuvel, M. van Soestbergen, and M. Z. Bazant. “Imposed currents in galvanic cells”. In: *Electrochimica Acta* 54 (21 2009), pp. 4857–4871. ISSN: 00134686. DOI: 10.1016/j.electacta.2009.03.073.

[52] Max F. Döpke and Remco Hartkamp. “The importance of specifically adsorbed ions for electrokinetic phenomena: Bridging the gap between experiments and MD simulations”. In: *J. Chem. Phys.* 154 (2021), p. 094701. DOI: https://doi.org/10.1063/5.0038161.

[53] Remco Hartkamp, Anne-Laure Biance, Li Fu, Jean-François Dufrêche, Oriane Bonhomme, and Laurent Joly. “Measuring surface charge: Why experimental characterization and molecular modeling should be coupled”. In: *Current Opinion in Colloid and Interface Science*. 37 (2018), pp. 101–114. DOI: https://doi.org/10.1016/j.cocis.2018.08.001.

[54] Lydéric Bocquet and Elisabeth Charlaix. “Nanofluidics, from bulk to interfaces”. In: *Chemical Society Reviews* 39 (3 2010), pp. 1073–1095. ISSN: 0306-0012. DOI: 10.1039/B909366B. URL: http://dx.doi.org/10.1039/B909366B.

4

PULSED ELECTROLYSIS FOR CO_2 REDUCTION

This study explores pulsed electrolysis as a strategy to address performance challenges in gas diffusion electrode (GDE)- CO_2 electrochemical reduction (CO_2ER). While GDEs facilitate direct CO_2 delivery to the reaction plane, they face obstacles such as cation-induced CO_2 blocking and reduced Faradaic efficiency (FE) at high cathodic potentials. Using a continuum-scale model, this work demonstrates that pulsed electrolysis can increase the current density compared to a system operating at a constant mean potential, though with a decrease relative to a constant high cathodic potential system. Pulsed electrolysis also shows an improved FE over constant high cathodic potential systems. Thicker catalyst layers (CLs) particularly benefit from pulsed electrolysis, achieving higher current densities near the gas/liquid interface along with overall improvements in Faradaic and cathodic efficiency than constant-potential systems due to prolonged time for the cations to transport back to and block the catalytic surface, which improves CO_2 accessibility. Tuning pulse parameters, especially with unequal durations, results in a similar current density as a constant potential system but with better Faradaic and cathodic efficiency. These findings underscore pulsed electrolysis as a scalable and effective method to enhance CO_2ER performance in GDE systems, offering practical improvements for industrial applications.

4.1. INTRODUCTION

The electrochemical reduction of CO_2 (CO_2ER) represents a promising avenue for mitigating CO_2 emissions while simultaneously producing valuable chemical feedstocks and fuels [1–4]. Significant research efforts have been dedicated to scaling up CO_2ER to industrial levels [5], with notable advancements in catalyst development [6], reactor design [7], and process optimization [8]. Despite these advancements, several challenges remain, such as ensuring high selectivity at industrial current densities, and reducing

This chapter is on the article: E. N. Butt, J. T. Padding, R. M. Hartkamp, "Unlocking the Potential of Pulsed Electrolysis: Mechanisms for Improved CO_2 Electroreduction in GDE Systems," *(Under review)* (2025)

energy consumption [9]. Especially for a planar H-cell type configuration, the attainable current density values are small due to mass transport limitations. Configurations using gas diffusion electrodes (GDE) are proposed to overcome these limitations by direct contact of gaseous CO_2 to the electrolyte inside a porous catalyst layer (CL), thus reducing the diffusion length of dissolved CO_2.

Apart from transporting the CO_2 towards the catalyst layer, it also needs to reach the reaction plane. Our recent computational study of a GDE pore [10] has shown that excessive cation adsorption at a high applied electrode potential sterically hinders the access of CO_2 to the reaction plane, thus limiting the current density and Faradaic efficiency (FE). Moreover, another study postulated that the local current density in a GDE pore decreases with an increasing distance from the gas/liquid interface due to CO_2 transport limitations into the flooded pore [11]. A possible way to overcome this limitation is by perturbing the reaction environment periodically via an alternating electrode potential, known as pulsed electrolysis [12, 13]. This technique has proven its ability in H-type cells to alter the selectivity of Cu and Ag catalysts through restructuring of the reaction environment [14–16], or to enhance stability by mitigating restructuring of the catalyst [17]. Combining the strengths of pulsing with those of a GDE configuration can be a powerful approach to leverage a high CO_2 transport rate while also having enhanced control over the local reaction environment within the porous matrix. Combining these techniques has been explored experimentally by Jeon et. al., who determined that pulsed operation can be used to tune the selectivity of C_1 and C_2 products in a GDE-type configuration [18]. Although experimental outcomes confirm this to be a promising approach, it is experimentally not feasible to directly probe the high-resolution spatial and temporal concentration variations that would occur throughout the porous catalyst layer during pulsed operation. Insight into the varying local conditions, and how these depend on system parameters, is needed to tailor the pulse to the specifics of the catalyst and operating conditions. Therefore, pore-scale computational models are essential to obtain detailed insight into the evolving local reaction environment during pulsed operation. To the best of our knowledge, such a pore-scale model of pulsed CO_2ER in a GDE is currently lacking. Schröder et. al. developed a 1D GDE model to simulate the pulsed current behavior for a metal-air battery system [19]. A few computational studies have focused on pulsed operation in CO_2ER, but again in the context of an H-cell configuration[20, 21]. Heßelmann et.al. developed a 1D mass transport model for Ag electrode accounting for the electric double layer (EDL) formation and concluded that a pulsed operation increased current density and cathodic efficiency relative to a constant potential operation. However, their work does not answer the question of whether pulsed operation would also benefit a GDE configuration operating at much higher (geometric) current densities.

In this work, we will use a time-dependent 2D continuum-scale model to simulate and study mass transfer alongside the catalytic reactions occurring inside a silver catalyst layer of a GDE operating under pulsed electrolysis. We will demonstrate that pulse electrolysis can help alleviate the previously reported [10] steric and transport hindrances in a CL, resulting in an increase in the Faradaic and cathodic efficiency of the system relative to a constant potential operation. We will establish that these increases are directly related to the increase in the lateral thickness of the CL. Furthermore, the optimal pulse duration to be applied to a GDE can be obtained on the thickness of the CL. We also propose a way

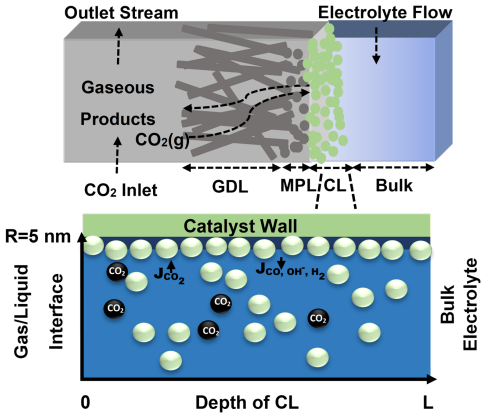

Figure 4.1: Schematic of a typical gas diffusion electrode. The zoomed-in section highlights the pore space in the catalyst layer (CL) with a characteristic depth L and characteristic radius R. Note that this schematic is not to scale because typically $L \gg R$.

to overcome the inefficient utilization of catalyst material in a GDE by leveraging pulsed electrolysis.

4.2. SIMULATION MODEL

Fig. 4.1 shows a schematic representation of a GDE, where the zoomed-in part represents the 2D flooded pore space in the CL studied here. CO_2 enters from the gas/liquid interface boundary on the side of the microporous diffusion layer (MPL) and undergoes electrochemical conversion at the outer-Helmholtz plane (OHP) of the dense immobile cation layer covering the catalyst surface. For a polycrystalline Ag surface, the main CO_2ER product is CO. The model is adapted for a 0.1 M $KHCO_3$ solution and resolves the electric potential and concentration profiles of all the solution species inside the CL pore space. Mass transfer is modeled using the size-modified Poisson-Nernst-Planck (SMPNP) equations [10, 22–27] and Frumkin-corrected Tafel equations are used to model the electrochemical reactions [28–32]. The finite element package FEniCS is used to solve the weak formulation of the non-linear SMPNP equations. Temporal discretizations are carried out using the backward Euler scheme. A time step of 10^{-6} s is used. Variable mesh spacing is used in the simulation domain, with a finer mesh near the high-potential boundaries. Details of the model and all the relevant boundary conditions are described in chapter 3.

In this study, we focus on rectangular pulsed potential operations. A high cathodic potential Φ_h is applied for a time duration of τ_h, after which the cathodic potential goes to a lower value Φ_l for a time duration τ_l, and the process repeats. Although the time-dependent cathodic potential is applied homogeneously along the catalyst surface, the resulting partial current densities will vary both in time and space due to the locally varying concentrations of reactive and charged species. Such local insight and control over conditions are instrumental in better understanding how to optimize electrochemical cells, but they are largely inaccessible in experiments. We will present both local and

spatially-averaged current densities in the following to analyze overall performance as well as being able to explain what causes the performance.

4.3. RESULTS

Fig. 4.2a shows the applied pulsed potential profile for a CO_2ER system, with the resulting partial current density shown in fig. 4.2b. For this study, the system is pulsed between Φ_h = -1.5 and Φ_l = -0.7 V vs RHE. This range provides suitable conditions for achieving high selectivities toward the desired CO_2ER reaction. The reaction rate at Φ_l is negligible (fig. 4.2b), such that the CO_2ER occurs predominantly during the Φ_h portion of the pulse period.

4.3.1. BENCHMARK CASE

For the benchmark case in this work, the thickness of the CL is L = 200 nm, the pore radius is R = 5 nm, and the durations of the pulse spent at Φ_h and Φ_l are equal, $\tau_h = \tau_l \approx$ 3.5 ms. In the later sections, we will also consider the implication of an unequal τ_h and τ_l and the influence of varying the thickness L of the CL on the performance of a pulsed system. The values for τ_h and τ_l in the benchmark case are on the approximate time needed to reach a steady state in similar GDE geometries [10]. We will show later that the relaxation time increases with the CL thickness. Correspondingly, most experimental explorations of pulsed electrolysis involve longer pulses, as the typical experimental CL thickness is also larger than those considered here. Our study provides mechanistic insights into how transport limitations and heterogeneous concentration distributions within the CL fundamentally influence performance, revealing the critical roles of CL thickness and pulsing frequency. These insights can inform and guide the interpretation and optimization of experimental systems. The main objective of lowering the cathodic potential in a pulsed operation is to slow down CO_2 consumption, thereby allowing its concentration near the reaction plane to recover. While CO_2 concentration does replenish during the Φ_l phase of a pulse cycle, it does not completely return to the initial bulk value from which the simulation began. Consequently, the first current density (j_{CO}) peak is higher than subsequent peaks (fig. 4.2b). To avoid these start-up effects, our analysis will be only on the subsequent peaks.

To understand the utility of pulsed electrolysis, we compare the time-averaged current density and Faradaic efficiency values obtained from a CO_2ER system under pulsed operation to a system operating under a constant benchmark applied potential. One option for this benchmark potential is the mean potential of the pulsed system (-1.1 V), represented by the black dotted line in fig. 4.2a. This corresponds to a scenario in which pulsed and constant potential systems operate under the same voltage efficiency ($\frac{\Phi^0}{\Phi_m}$). Alternatively, the time-averaged current density and Faradaic efficiency can be compared to those of a system operating at a constant potential of Φ_h (-1.5 V) (gray line in fig. 4.2a). The time-averaged j_{CO} due to pulsed electrolysis is 203 Am^{-2}. This is $\approx$ 44% higher than for a system operating at a constant applied potential of -1.1 V. This increase is due to the transient high current densities during the Φ_h section of the pulse cycle. Furthermore, the pulsed system steadies to a j_{CO} that is higher than a system operating at constant -1.1 V. Combined, these factors are sufficient to offset the low current density during the

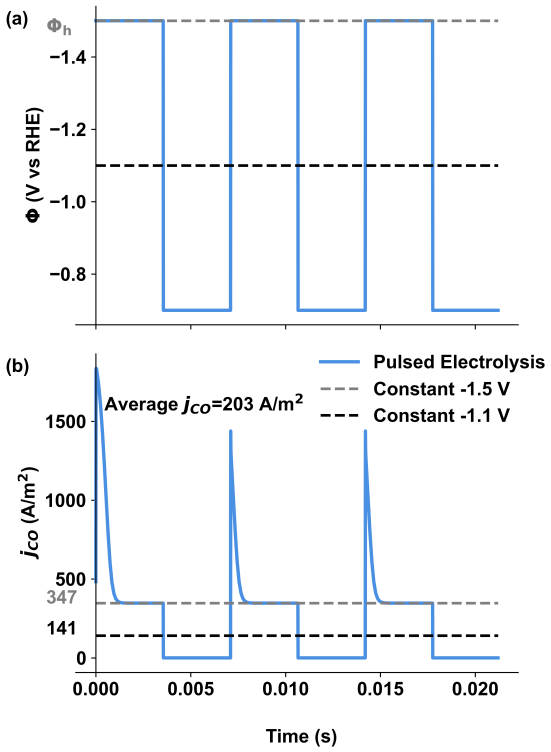

Figure 4.2: (a) Pulsed potential profile for a 200 nm thick CL. The dotted line represents the mean potential of the pulsed operation (b) Corresponding current density of CO_2 conversion to CO (j_{CO}), averaged over the length of the pore. Dotted lines correspond to the j_{CO} values for the constant potential operations

Φ_l section of the pulsed system. During the Φ_l section of the pulse, the reaction rate of CO_2ER will initially be lower than HER because of CO_2 deficiency at the OHP. As the CO_2 concentration gradually replenishes near the OHP, the gap between the reaction rates for both catalytic reactions decreases (fig. C.10). The time-averaged j_{CO} of a pulsed system is $\approx$ 41% lower than j_{CO} of a system operating continuously at a potential of Φ_h (fig. 4.2b). Unlike the comparison with a constant -1.1 V system, the current density during the Φ_h section of the pulse steadies to the benchmark case. The pulsed system spends a further half cycle at Φ_l. At this potential, there is barely any CO_2 reduction and any advantage due to the transient high current densities in the Φ_h section of the cycle is not high enough to compensate for this drop.

Fig. 4.3 shows that contrary to the current density, there is a significant drop in FE of CO_2ER reaction under a pulsed operation compared to a constant potential operation at the mean value of -1.1 V. This is because at -1.1 V there is a negligible amount of H_2 evolution reaction (HER) compared to CO_2ER. This results in a larger selectivity towards CO. However, unlike CO_2ER, HER scales exponentially with the applied potential, and since the pulsed system spends half a cycle at the more cathodic Φ_h, the production of

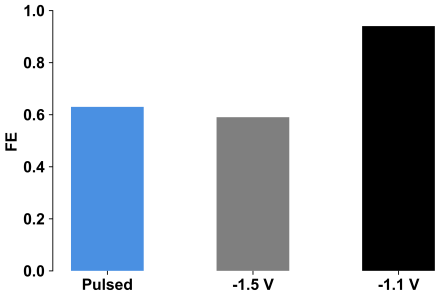

Figure 4.3: Faradaic efficiencies for a 200 nm thick CL under pulsed operation (Φ_h= -1.5 V, Φ_l= -0.7 V, τ_h= τ_l= 3.5 ms.) and with constant potentials of -1.1 V and -1.5 V.

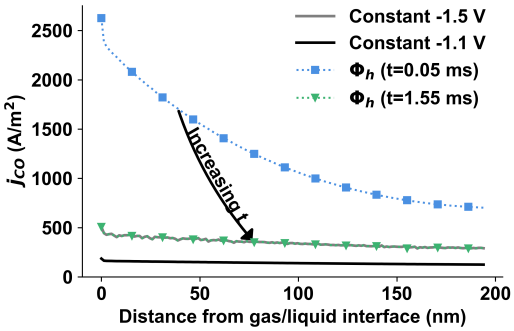

Figure 4.4: Local current density against the distance from the gas/liquid interface in a 200 nm thick CL for pulsed electrolysis (Φ_h= -1.5 V, Φ_l= -0.7 V, τ_h= τ_l= 3.5 ms) at different times compared to the current density profile of systems operating at constant potentials of -1.1 V and -1.5 V.

HER increases significantly, leading to a drop in the selectivity towards CO. In contrast, an $\approx$ 4% increase in selectivity towards CO is observed in a pulsed operation compared to a system operation at a constant -1.5 V potential. This increase is largely due to the transient high current densities observed in the Φ_h phase of the pulse, as illustrated in fig. 4.2b. The transient peaks in the pulsed operation are facilitated by the large cathodic potential combined with a high initial CO_2 concentration at the outer Helmholtz plane (OHP). It can also be seen that initially, the current density is much higher near the gas/liquid interface compared to the rest of the CL and after some time it decays to a steady state (fig. 4.4). This decay is due to two concurrent mechanisms: In the first place, the CO_2 at the catalyst surface is consumed faster than it is supplied from the gas/liquid interface. Second, as more cations migrate from the bulk reservoir into the CL, their accumulation at the OHP sterically hinders the remaining CO_2 molecules. The competition between the transport and consumption rates suggests a strong dependence of both the local and global current density on the actual thickness of the CL.

4.3.2. INFLUENCE OF CL THICKNESS

It is clear from the above analysis that the time spent in the transient state is critical in controlling the performance of pulsed electrolysis. This transient time depends on the transport time scales in the CL, which in turn are affected by the pore length and radius. Due to the high aspect ratio of the pore, the length will be decisive for the duration of the transient. Therefore, we compare the current density profile under pulsed electrolysis for 100-400 nm thick CLs (fig. 4.5a). The applied potential range and the pulse duration are similar to the previous results. It can be observed that with increasing thickness of the CLs, the decay time of the current density from its initial peak to a steady value increases, and this increase follows an almost linear trend as shown in fig. 4.5b.
It is also evident from fig. 4.5a that the current densities converge to lower values with increasing thickness of the CL. An almost linear decrease in the current density is observed (fig. 4.5c) as a result of CO_2 mass transfer limitations. The greater the distance is from the CO_2 inlet (gas/liquid interface), the more deficient in CO_2 concentration that point would be inside the CL. Hence, a thick CL has a significantly larger section of its length in a CO_2 mass transfer limited regime than a thinner CL. This implies that a significant part of the CL is not efficiently used for the CO_2ER reaction. The current density will decrease with increasing CL thickness regardless of the mode of operation (pulsed or constant). However, we observe that this decrease is less severe in pulsed electrolysis (fig. 4.5c). It is also worth pointing out that under pulsed electrolysis, these current densities are achieved at higher cathodic efficiency ($\frac{\Phi_0}{\Phi_m} \cdot FE$) (fig. C.7). Fig. 4.6 shows that the Faradaic efficiency of a system under pulsed electrolysis is generally higher than that of a system operating at a constant potential of -1.5 V due to the higher driving force for HER of the latter. This difference in FE between the two modes of operation increases with the thickness of CL, since the drop in j_{CO} as the thickness of CL increases is weaker in pulsed electrolysis. As suggested before, the primary reason for the improved FE in fig. 4.6 and the diminishing difference between the current density of a pulsed system and a constant potential system with increasing CL thickness in fig. 4.5c, is the time spent in a transient state during the Φ_h section of the pulse. This can be observed in fig. 4.7a. More CO_2 is available during the transient period and this CO_2 also has easier access to the catalyst surface, resulting in higher transient j_{CO} values compared to the steady state at the same applied potential. 0.5 ms after starting the application of Φ_h, CO_2 reaches a low concentration near the CO_2 inlet in the case of the 200 nm CL, whereas the 400 nm CL retains a concentration at least twice as high after the same duration. This results in transient peaks of CO_2ER current density for the 400 nm CL. Even after 1 ms, the 400 nm CL shows higher CO_2 concentration compared to a 200 nm CL, which has reached a steady state. The main reason for the difference in CO_2 concentration between the two layers, is the difference in the amount of steric hindrance posed by cations. For a 400 nm CL, it takes longer for K^+ to reach a similar concentration as a 200 nm thick CL, hence the CO_2 molecules in that region face lower steric effects relative to a smaller CL. The inverse relation between the cation concentration and the presence of CO_2 molecules near the OHP has been extensively documented in previous works [10, 33]. Fig. 4.7b shows that the K^+ concentration has almost reached a steady state after 0.5 ms, in a 200 nm CL, unlike for the 400 nm CL. The longer transient period in the thicker CL corresponds to maintaining a high CO_2 concentration at the catalyst surface for longer, directly leading to a higher

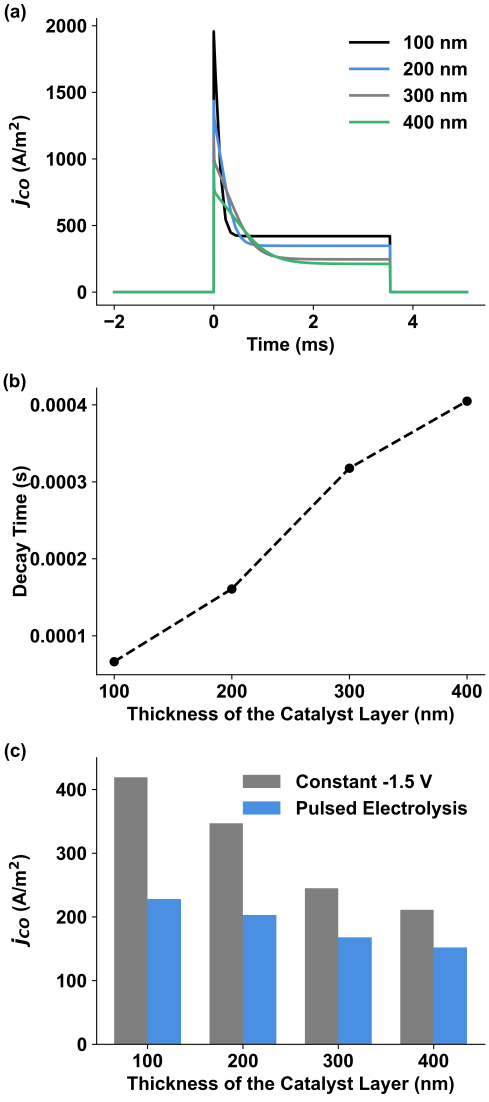

Figure 4.5: (a) j_{CO} profile with time for an Ag polycrystalline GDE system under pulsed electrolysis for varying thicknesses of CL. (b) Variation of j_{CO} decay time with changing thickness of the CL. (c) Comparison of absolute j_{CO} between a constant potential operation at -1.5 V and pulsed electrolysis, for various thicknesses of the CL. Φ_h= -1.5 V, Φ_l= -0.7 V, τ_h= τ_l = 3.5 ms.

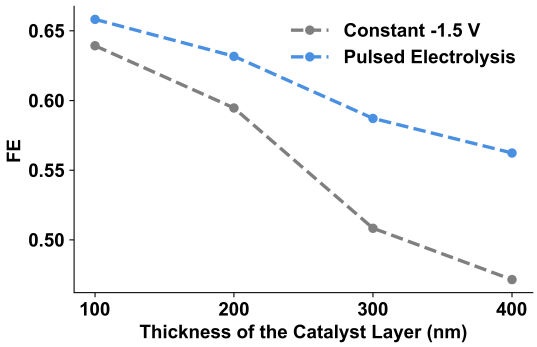

Figure 4.6: FE of CO_2ER under pulsed electrolysis compared to a constant potential system at -1.5 V, for various thicknesses of the CL. Φ_h= -1.5 V, Φ_l= -0.7 V, τ_h= τ_l = 3.5 ms.

j_{CO}.
Fig. 4.8 shows local (15 nm away from the CO_2 input) current densities with increasing CL thickness. In the early stages of Φ_h (t = 0.05 ms), the value of j_{CO} increases with the thickness of the CL due to the prolonged transient state of cations and CO_2, as previously discussed. After 3.05 ms, the cation concentration at the catalyst surface stabilizes, leading to a steady current density. Within the first 15 nm, this steady-state current density remains unaffected by transport limitations and is therefore independent of pore length. However, increasing the thickness of the catalyst layer generally reduces the overall pore-averaged current density (Fig. 4.5c). To maximize the gains from pulsed electrolysis, we could design a porous layer where the active catalyst loading is concentrated in the section close to the gas/liquid interface. As experiments with gradient catalyst loading have demonstrated, simply adding more catalyst does not ensure improved performance, since this would also require more CO_2 to be transported to the catalyst surface [34]. Instead, if the active catalyst material is only present until a certain distance from the gas/liquid interface, then the remainder of the porous layer primarily serves to prolong cationic transport, whereas the CO_2 only faces a short transport path. Under these conditions, the overall current densities for pulsed and constant potential operations will align with those depicted in the t = 0.05 ms and t = 3.05 ms plots in Fig. 4.8. This means that in a pulsed operation, the current densities would be significantly higher than in a constant potential operation and will increase with increasing CL length. Fig. C.1 shows that the local current densities increase with the thickness of the CL up to the first 45 nm away from the gas/liquid interface. Hence, this could serve as a cut-off length for the active CL.
Interestingly, immediately after the onset of ϕ_h, the cation concentration exhibits a non-monotonic temporal trend with accumulation occurring near the gas/liquid interface (fig. C.11). The primary reason for this is the relatively slow screening of the electric potential near the gas/liquid interface (fig. C.6). In contrast, the region of the CL closest to the bulk phase has readily available cations, resulting in a more rapid potential screening. This initial imbalance in electric potential creates a strong migratory force that pulls cations

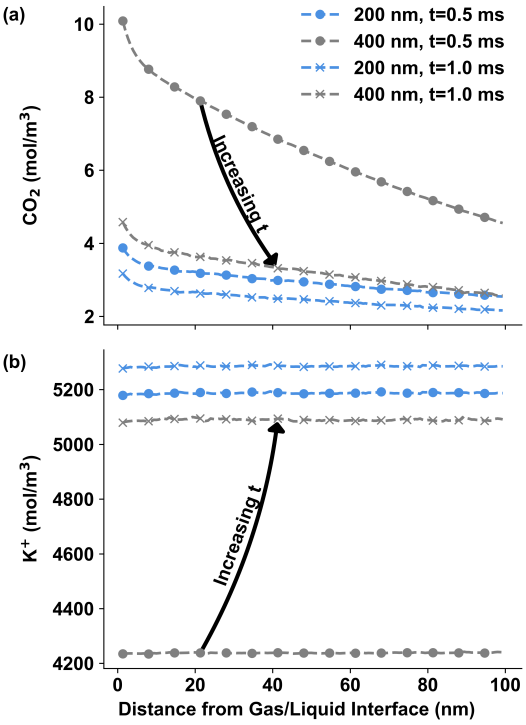

Figure 4.7: Comparison of concentration profiles up to 100 nm away from the gas/liquid interface for overall CL thicknesses of 200 and 400 nm at different times during the Φ_h section of the periodic pulse, (a) CO_2, (b) K^+. Φ_h= -1.5 V, Φ_l= -0.7 V, $\tau_h = \tau_l = 3.5$ ms.

from the bulk toward the gas/liquid interface. This effect is evident in fig. C.11, where the cation concentration reaches its highest value at a distance of 10 nm away from the gas/liquid interface after 10^{-5} s. Although diffusive forces attempt to oppose the migratory flux, the migratory flux dominates at this stage, leading to a net accumulation of cations and a depletion of anions near the gas/liquid interface. This causes a charge imbalance even at the center of the CL, which is not expected in a pore of 5 nm radius at the bulk electrolytic concentration of 0.1 M. To quantify this behavior for a 400 nm thick CL, the ratio of migratory flux (J_{mig}) to diffusive flux (J_{diff}) can be expressed as: $\frac{J_{\text{mig}}}{J_{\text{diff}}} = \frac{C_{K,\text{avg}}}{\Delta C_K}\left(\frac{\Delta\phi}{V_{\text{ther}}}\right)$. At $t \sim 10^{-5}$ s, the average K^+ concentration is approximately $C_{K,\text{avg}} = 125\,\text{mol/m}^3$, the concentration difference is $\Delta C_K = 170\,\text{mol/m}^3$, and the normalized potential difference is $\Delta\phi/V_{\text{ther}} = 2$. The value for $\frac{J_{\text{mig}}}{J_{\text{diff}}}$ is ≈ 1.5 at $t \sim 10^{-5}$ s. Over time, as the electric field stabilizes and approaches bulk values, the flux ratio decreases, reducing the concentration gradient between the bulk phase and the gas/liquid interface (as seen at $t \sim 10^{-4}$ s in fig C.11). By $t \sim 10^{-3}$ s, the cations near the OHP have reached the steric limit, leading to a subsequent radial thickening of the cation layer. This results in the final observed increase in the cation concentration at the center of the CL.

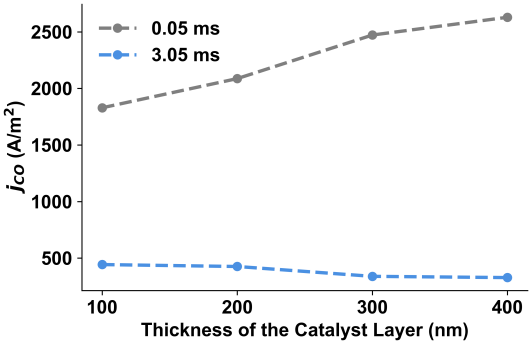

Figure 4.8: Local j_{CO} at a location 15 nm away from the gas/liquid interface for 100-400 nm thick CLs at different times. Φ_h= -1.5 V, Φ_l= -0.7 V, τ_h= τ_l = 3.5 ms.

This dynamic interplay between migration and diffusion highlights the transient and spatially dependent nature of ion transport in catalyst layers. Importantly, this challenges the widely used assumption of electroneutrality, which is rarely valid inside these narrow catalyst layers at any time during the process. The deviations from electroneutrality are significant and persist throughout the system, influencing the overall ion transport dynamics and concentration profiles.

4.3.3. INFLUENCE OF PULSE DURATION

Until now we have discussed modifications in terms of thickness of the CL to optimize the performance of pulsed electrolysis in a GDE. Another way to increase the performance of pulsed systems is to optimize the applied potential profile. This can be done by either decreasing the duration of a pulse (τ_h, τ_l) or by optimizing the upper and lower bounds of applied potential during the pulse (Φ_h, Φ_l).

Fig. 4.9a shows the j_{CO} profile for the same Φ_h and Φ_l values as used in fig. 4.2, but the duration of each half of the cycle is now ≈ 1.55 ms, compared to ≈ 3.5 ms in fig. 4.2. The time-averaged j_{CO} is still less than that obtained from a constant potential system but the difference is now significantly smaller compared to the difference observed for the longer τ_h and τ_l in fig. 4.2b. A shorter τ_h corresponds to less time spent at the steady state plateau, hence, more efficiently leveraging the benefits of the transient regime. Similarly, the smaller τ_l also reduces the time spent in the low CO_2ER phase.

The pulse profile can be further optimized by applying Φ_h and Φ_l for unequal duration. It can be observed in fig. 4.9b that unequal duration (τ_h = 2.5 ms, τ_l = 1.55 ms) results in a higher time-averaged j_{CO} compared to the equal duration pulse in fig. 4.9a. It should also be pointed out that the mean potential of the pulse system in fig. 4.9b is ≈ −1.2 V as compared to -1.1 V in 4.9a and 4.2b. Thus, the increase in current density comes at the cost of a lower voltage efficiency.

We have shown that increasing the catalyst layer thickness reduces the difference in j_{CO} between pulsed and constant potential systems when Φ_h=Φ_l (Fig. 4.5c). Applying an unequal pulsed operation to a thicker CL should further minimize this difference. Fig.

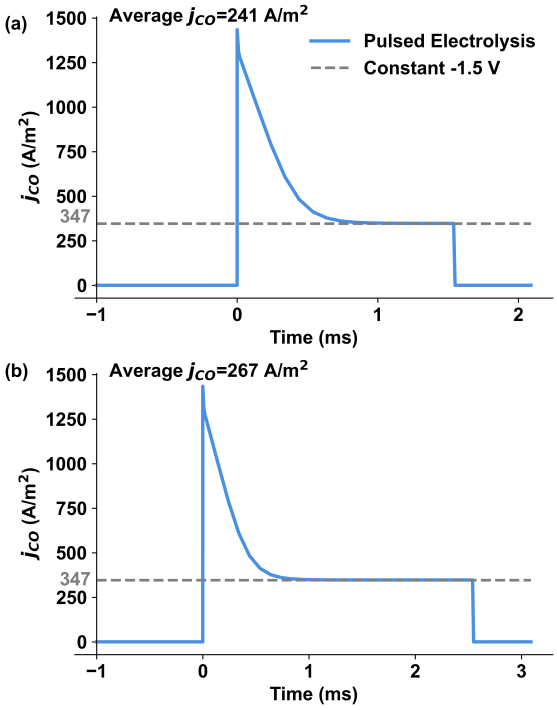

Figure 4.9: Comparison of j_{CO} between pulsed electrolysis and a constant potential operation of -1.5 V for a 200 nm thick CL. (a) Φ_h= -1.5 V, Φ_l= -0.7 V, τ_h= τ_l = 1.55 ms, (b) Φ_h= -1.5 V, Φ_l= -0.7 V, τ_h = 2.5 ms, τ_l = 1.55 ms.

4.10 depicts the current density profile for an unequal duration (τ_h = 2.5 ms, τ_l = 1.55 ms) in a 400 nm thick CL. It can be observed that the time-averaged current density of the periodic pulse reaches almost the same value as that in a constant potential system but at a higher cathodic efficiency (fig. C.8). Fig. 4.11a compares the current density values for a system operating at a constant potential with pulsed systems at both equal and unequal τ_l and τ_h. The data shows that the lower current density in pulsed operation compared to constant potential operation can be remedied by unequal pulsing, although this effect becomes more apparent for the thicker CL, ultimately resulting in a negligible difference between constant and pulsed operation. The Faradaic efficiency remains higher for a pulsed operation regardless of the CL thickness and the mode of the pulse (equal or unequal) (fig. 4.11b). However, the gain is again higher when $\Phi_h \neq \Phi_l$ and for the thicker CL. Naturally, the unequal mode corresponds to a higher mean potential relative to the equal mode operation, hence there will be a drop of cathodic efficiency but it remains higher than that of the constant potential system (fig. **??**). Thus, for a larger CL, the operating parameters of pulsed electrolysis can be tuned to give better FE results at a higher cathodic efficiency compared to a constant potential operation without compromising the current density of CO_2ER.

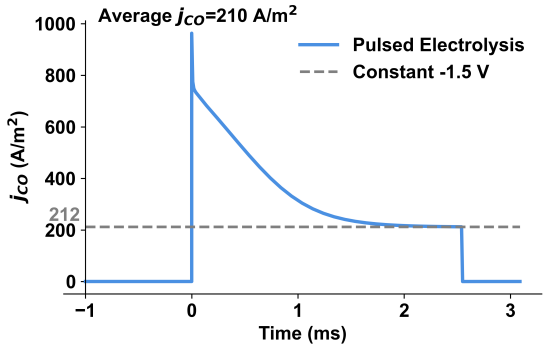

Figure 4.10: Comparison of j_{CO} between pulsed electrolysis and a constant potential operation of -1.5 V for a 400 nm thick CL. (a) Φ_h= -1.5 V, Φ_l= -0.7 V, τ_h = 2.5 ms, τ_l = 1.55 ms.

4.4. DISCUSSION

The duration for which Φ_h and Φ_l are applied is crucial to maximize the performance of pulsed electrolysis in a GDE. The suitable choice for τ_l depends on the CO_2 replenishing time, which in turn depends on the thickness of CL. In this work, a minimum τ_l = 1.5 ms was enough to replenish the concentration of CO_2 in each of the studied catalyst layers. The benefits of transient current density can be optimally leveraged if τ_h is similar to the decay time for the j_{CO}. A τ_h higher than the decay time would diminish the transient gains in FE whereas lowering it will decrease the time averaged j_{CO}. It is also worth pointing out that the decay time could be several orders of magnitude larger (of the order of a few seconds) in a planar electrode assembly due to increased mass transport limitations. As fig. 4.5b showed, the decay time for current density increases linearly with an increasing catalytic layer thickness. Hence, a suitable τ_h can be inferred on the thickness of the GDE CL.

At high pulsing rates, the energy associated with capacitative charging during each cycle can become prohibitive. This capacitive energy lowers the energy efficiency and becomes dissipated as heat. We note that specific adsorption onto the catalytic surface is not modeled in this study. This has previously been shown to influence the stabilization of reaction intermediates, which influences the product selectivity, especially for CO_2ER processes focusing on C_{2+} products[35, 36]. Future modeling approaches should incorporate microkinetic models to accurately determine the influence of intermediate species on product selectivities [21]. Although the current densities predicted by our model are entirely associated with the Faradaic reactions, capacitive charging can be predicted on electrical double layer theory. For a 200 nm thick CL, $W = \frac{1}{2}C\Delta\Phi_m^2 \approx 5\ \mu J/cm^2$ per pulse cycle. This is 40 times smaller than the energy going into the CO_2ER reaction (for $\tau_h = \tau_l = 3.5$ ms). For the GDE geometry under consideration, the time constant for the decay of capacitative current density is only a few nanoseconds, $T = \lambda_d R/D$. Here, λ_d is the Debye length, R is the radius of a pore in the CL, and D is the diffusion coefficient of the dominant cation (in this case potassium). This is also in accordance with EDL equilibration times found in molecular dynamic simulations [37]. This capacitive time

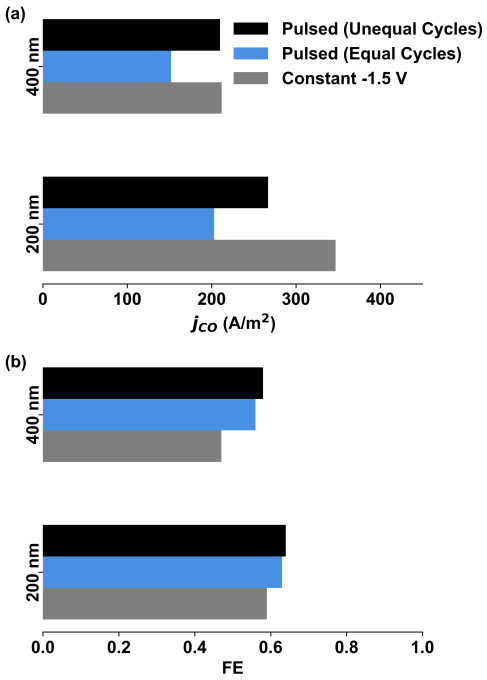

Figure 4.11: Comparison of constant potential operation of -1.5 V, pulsed electrolysis with equal cycles (τ_h= τ_l = 3.5 ms.) and pulsed electrolysis for unequal cycles (τ_h = 2.5 ms, τ_l = 1.55 ms) for 200 and 400 nm thick CL, (a) j_{CO}, (b) FE.

is extremely short compared to τ_h studied in this work. Additionally, the ability to sustain high-frequency pulsing rates is contingent not only on the chemical and physical properties of the catalytic system but also on the performance of the associated power electronics. Power electronics must be capable of rapidly switching potentials without significant losses or inefficiencies, which can pose a challenge at these timescales. Future studies could explore the interplay between power electronics performance and reaction efficiency, as well as the associated energy costs for different switching regimes.

4.5. CONCLUSION

We simulated the behavior of a GDE- (polycrystalline Ag) CO_2ER system under the application of pulsed electrolysis. To analyze the performance, we compared the current density and FE attained under a pulsed operation with a system under the application of constant potential. Pulsed electrolysis was shown to yield a significant increase in j_{CO} compared to the mean potential owing to the transient high current densities during the Φ_h part of the pulse. The FE, however; drops significantly because the rate of HER increases exponentially with potential. When comparing the performance of pulsed electrolysis with a system under a constant high potential of -1.5 V (Φ_h), we observed a 41% drop of j_{CO} and an $\approx$ 4% increase in FE of CO_2ER reaction.

We determined that the relative performance of a pulsed system is intricately linked to the time spent in the transient current density state with longer transient leading to improved Faradaic and cathodic efficiencies. This transient state can be prolonged by increasing the thickness of the catalyst layer due to the increased time for the cationic transport. This directly influences the CO_2 concentration at the OHP due to less steric hindrance. We also observed that current density near the gas/liquid interface increases with CL thickness. on this, we recommended a CL that is catalytically active only until a certain distance, maximizing the current density and reducing the catalyst cost. This study also shows that transient cation accumulation near the gas/liquid interface leads to significant deviations from electroneutrality, challenging widely held assumptions in catalyst layer modeling and affecting overall ion transport. We further determined that tuning the time for each part of the pulse (τ_h vs τ_l) also leads to an increased performance. A shorter pulse with unequal duration ($\tau_h > \tau_l$) performed better than an equal duration pulse. Both equal and unequal pulses lagged in terms of j_{CO} compared to a constant potential operation for a 200 nm thick CL. For a 400 nm thick CL, a shorter unequal pulse resulted in similar j_{CO} as a system under constant potential at a higher cathodic efficiency. Furthermore, both equal and unequal pulses resulted in increased FE for CO_2ER, with unequal pulse outperforming the equal pulsed operation. We also showed that τ_h can be selected on the decay time for j_{CO}. The decay time increases almost linearly with the increased thickness of the CL. This is especially helpful for researchers working with varying thicknesses of the CL.

The analysis provided in this study proves that pulsed electrolysis can be extremely beneficial for GDE- CO_2ER systems, especially for thicker catalyst layers. In the future, more research needs to be done on ways of optimizing the duration of each half of the pulse cycle for a porous GDE.

REFERENCES

[1] Zhifei Yan, Jeremy L. Hitt, John A. Turner, and Thomas E. Mallouk. “Renewable electricity storage using electrolysis”. In: *Proceedings of the National Academy of Sciences of the United States of America* 117 (23 June 2020), pp. 12558–12563. ISSN: 10916490. DOI: 10.1073/pnas.1821686116.

[2] Xu Lu, Dennis Y.C. Leung, Huizhi Wang, Michael K.H. Leung, and Jin Xuan. “Electrochemical Reduction of Carbon Dioxide to Formic Acid”. In: *ChemElectroChem* 1 (5 2014), pp. 836–849. ISSN: 21960216. DOI: 10.1002/celc.201300206.

[3] Joaquin Resasco, Leanne D. Chen, Ezra Clark, Charlie Tsai, Christopher Hahn, Thomas F. Jaramillo, Karen Chan, and Alexis T. Bell. “Promoter Effects of Alkali Metal Cations on the Electrochemical Reduction of Carbon Dioxide”. In: *Journal of the American Chemical Society* 139 (32 Aug. 2017), pp. 11277–11287. ISSN: 15205126. DOI: 10.1021/jacs.7b06765.

[4] Devin T. Whipple and Paul J. A. Kenis. “Prospects of CO_2 Utilization via Direct Heterogeneous Electrochemical Reduction”. In: *J. Phys. Chem. Lett.* 1 (24 2010), pp. 3451–3458. DOI: doi:10.1021/jz1012627.

[5] Richard I. Masel, Zengcai Liu, Hongzhou Yang, Jerry J. Kaczur, Daniel Carrillo, Shaoxuan Ren, Danielle Salvatore, and Curtis P. Berlinguette. "An industrial perspective on catalysts for low-temperature CO_2 electrolysis". In: *Nature Nanotechnology* 16 (2021), pp. 118–128. DOI: https://doi.org/10.1038/s41565-020-00823-x.

[6] Fengwang Li, Douglas R. MacFarlane, and Jie Zhang. "Recent advances in the nanoengineering of electrocatalysts for CO_2 reduction". In: *Nanoscale* 10 (2018), pp. 6235–6260. DOI: https://doi.org/10.1039/C7NR09620H.

[7] Dui Ma, Ting Jin, Keyu Xi, and Haitao Huang. "An overview of flow cell architecture design and optimization for electrochemical CO_2 reduction". In: *J. Mater. Chem. A* 9 (37 2021), pp. 20897–20918. DOI: https://doi.org/10.1039/D1TA06101A.

[8] Saket S. Bhargava, Federica Proietto, Daniel Azmoodeh, Emiliana R. Cofell, Danielle A. Henckel, Sumit Verma, Christopher J. Brooks, Andrew A. Gewirth, and Paul J.A. Kenis. "System Design Rules for Intensifying the Electrochemical Reduction of CO_2 to CO on Ag Nanoparticles". In: *ChemElectroChem* 9 (9 2020), pp. 2001–2011. DOI: https://doi.org/10.1002/celc.202000089.

[9] Junjun Li, Sulaiman Umar Abbas, Haiqing Wang, Zhicheng Zhang, and Wenping Hu. "Recent Advances in Interface Engineering for Electrocatalytic CO_2 Reduction Reaction". In: *Nano-Micro Lett.* 13 (2021), p. 216. DOI: https://doi.org/10.1007/s40820-021-00738-9.

[10] Esaar Naeem Butt, Johan T. Padding, and Remco Hartkamp. "Local Reaction Environment Deviations within Gas Diffusion Electrode Pores for CO_2 Electrolysis". In: *Journal of The Electrochemical Society* 171 (1 2024), p. 014504. DOI: DOI10.1149/1945-7111/ad1cb4.

[11] Thomas Burdyny and Wilson A. Smith. "CO2 reduction on gas-diffusion electrodes and why catalytic performance must be assessed at commercially-relevant conditions". In: *Energy Environ. Sci.* 12 (2019), p. 1442. DOI: DOI:10.1039/c8ee03134g.

[12] Rileigh Casebolt, Kelsey Levine, Jin Suntivich, and Tobias Hanrath. "Pulse check: Potential opportunities in pulsed electrochemical CO_2 reduction". In: *Joule* 5 (8 2021), pp. 1987–2026. DOI: https://doi.org/10.1016/j.joule.2021.05.014.

[13] Tao Liu, Jinling Wang, Xuejing Yang, and Ming Gong. "A review of pulse electrolysis for efficient energy conversion and chemical production". In: *Journal of Energy Chemistry* 59 (2020), pp. 69–82. DOI: https://doi.org/10.1016/j.jechem.2020.10.027.

[14] Ryuichi Shiratsuchi, Yoshihisa Aikoh, and Gyoichi Nogami. "Pulsed Electroreduction of CO_2 on Copper Electrodes". In: *J. Electrochem. Soc.* 140 (1993), p. 3479. DOI: DOI10.1149/1.2221113.

[15] Ryuichi Shiratsuchi and Gyoichi Nogami. "Pulsed Electroreduction of CO_2 on Silver Electrodes". In: *J. Electrochem. Soc.* 143 (1996), p. 582. DOI: DOI10.1149/1.1836484.

[16] Chanyeon Kim, Lien-Chun Weng, and Alexis T. Bell. “Impact of Pulsed Electrochemical Reduction of CO_2 on the Formation of C2+ Products over Cu”. In: *ACS Catalysis* 10 (21 2020), pp. 12403–12413. DOI: https://doi.org/10.1021/acsenergylett.0c02401.

[17] Jesse Kok, Jim de Ruiter, Ward van der Stam, and Thomas Burdyny. “Interrogation of Oxidative Pulsed Methods for the Stabilization of Copper Electrodes for CO_2 Electrolysis”. In: *Journal of the American Chemical Society* 146.28 (2024), pp. 19509–19520. DOI: 10.1021/jacs.4c06284. URL: https://pubs.acs.org/doi/full/10.1021/jacs.4c06284.

[18] Hyo Sang Jeon, Janis Timoshenko, Clara Rettenmaier, Antonia Herzog, Aram Yoon, See Wee Chee, Sebastian Oener, Uta Hejral, Felix T. Haase, and Beatriz Roldan Cuenya. “Selectivity Control of Cu Nanocrystals in a Gas-Fed Flow Cell through CO2 Pulsed Electroreduction”. In: *J. Am. Chem. Soc.* 143 (19 2021), pp. 7578–7587. DOI: https://doi.org/10.1021/jacs.1c03443.

[19] Daniel Schrödera, Vincent Lauea, and Ulrike Krewera. “Numerical simulation of gas-diffusion-electrodes with moving gas–liquid interface: A study on pulse-current operation and electrode flooding”. In: *Computers and Chemical Engineering* 84 (2016), pp. 217–225. DOI: https://doi.org/10.1016/j.compchemeng.2015.09.005.

[20] Justin C. Bui, Chanyeon Kim, Adam Z. Weber, and Alexis T. Bell. “Dynamic Boundary Layer Simulation of Pulsed CO_2 Electrolysis on a Copper Catalyst”. In: *ACS Energy Letters* 6 (4 2021), pp. 1181–1188. DOI: https://doi.org/10.1021/acsenergylett.1c00364.

[21] Matthias Heßelmann, Daniel Felder, Wenzel Plischka, Sajad Nabi, John Linkhorst, Matthias Wessling, and Robert Keller. “Dynamics of the Boundary Layer in Pulsed CO_2 Electrolysis”. In: *Angew. Chem. Int. Ed.* 63 (34 2024), e202406924. DOI: https://doi.org/10.1002/anie.202406924.

[22] P. M. Biesheuvel, M. van Soestbergen, and M. Z. Bazant. “Imposed currents in galvanic cells”. In: *Electrochimica Acta* 54 (21 2009), pp. 4857–4871. ISSN: 00134686. DOI: 10.1016/j.electacta.2009.03.073.

[23] Martin Z Bazant, Mustafa Sabri Kilic, Brian D Storey, and Armand Ajdari. “Towards an understanding of induced-charge electrokinetics at large applied voltages in concentrated solutions.” In: *Advances in colloid and interface science* 152 (1-2 Nov. 2009), pp. 48–88. ISSN: 1873-3727 (Electronic). DOI: 10.1016/j.cis.2009.10.001.

[24] Mustafa Sabri Kilic, Martin Z. Bazant, and Armand Ajdari. “Steric effects in the dynamics of electrolytes at large applied voltages. II. Modified Poisson-Nernst-Planck equations”. In: *Physical Review E - Statistical, Nonlinear, and Soft Matter Physics* 75 (2 Feb. 2007), p. 021502. ISSN: 15393755. DOI: 10.1103/PhysRevE.75.021503.

[25] Laurent Pilon, Hainan Wang, and Anna d'Entremont. "Recent Advances in Continuum Modeling of Interfacial and Transport Phenomena in Electric Double Layer Capacitors". In: *Journal of The Electrochemical Society* 162 (5 2015), A5158–A5178. ISSN: 0013-4651. DOI: 10.1149/2.0211505jes.

[26] Stefan Ringe, Carlos G. Morales-Guio, Leanne D. Chen, Meredith Fields, Thomas F. Jaramillo, Christopher Hahn, and Karen Chan. "Double layer charging driven carbon dioxide adsorption limits the rate of electrochemical carbon dioxide reduction on Gold". In: *Nature Communications* 11 (1 Dec. 2020), p. 33. ISSN: 20411723. DOI: 10.1038/s41467-019-13777-z.

[27] Divya Bohra, Jehanzeb H Chaudhry, Thomas Burdyny, Evgeny A Pidko, and Wilson A Smith. "Mass transport in catalytic pores of GDE-based CO_2 electroreduction systems". In: *ChemRxiv* (2020). DOI: https://doi.org/10.26434/chemrxiv.13073348.v1.

[28] A Frumkin. "wasserstoffuberspannung und struktur der doppelschicht." In: *Zeitschrift für physikalische Chemie* 164 (1 1933), pp. 121–133.

[29] Marco Rossi, Thomas Wallmersperger, Stefan Neukamm, and Kathrin Padberg-Gehle. "Modeling and Simulation of Electrochemical Cells under Applied Voltage". In: *Electrochimica Acta* 258 (2017), pp. 241–254. ISSN: 00134686. DOI: 10.1016/j.electacta.2017.10.047. URL: http://dx.doi.org/10.1016/j.electacta.2017.10.047.

[30] Esaar Naeem Butt, Johan T. Padding, and Remco Hartkamp. "Size-modified Poisson-Nernst-Planck approach for modeling a local electrode environment in CO_2 electrolysis". In: *Sustainable Energy and Fuels* 7 (1 Nov. 2023), pp. 144–154. ISSN: 23984902. DOI: 10.1039/d2se01262f.

[31] Roger Parsons. "Structure of the electrical double layer and its influence on the rates of electrode reactions". In: *Advances in Electrochem. Electrochem. Eng.* (1 1961), pp. 1–64.

[32] Paul Delahay. *Double Layer and Electrode Kinetics*. 2nd ed. Interscience, 1965.

[33] Divya Bohra, Jehanzeb H. Chaudhry, Thomas, Evgeny A. Pidko, and Wilson A. Smith. "Modeling the electrical double layer to understand the reaction environment in a CO_2 electrocatalytic system". In: *Energy and Environmental Science* 12 (11 2019), pp. 3380–3389. ISSN: 17545706. DOI: 10.1039/c9ee02485a.

[34] Mariana C. O. Monteiro, Stefan Dieckhöfer, Tim Bobrowski, Thomas Quast, Davide Pavesi, Marc T. M. Koper, and Wolfgang Schuhmann. "Probing the local activity of CO_2 reduction on gold gas diffusion electrodes: effect of the catalyst loading and CO_2 pressure". In: *Chemical Science* 12 (41 2021), pp. 15682–15690. DOI: https://doi.org/10.1039/D1SC05519D.

[35] Rileigh Casebolt, Kevin W. Kimura, Kelsey Levine, Jessica Akemi Cimada DaSilva, Jiyoon Kim, Tyler A. Dunbar, Jin Suntivich, and Tobias Hanrath. "Effect of Electrolyte Composition and Concentration on Pulsed Potential Electrochemical CO_2 Reduction". In: *ChemElectroChem* 8 (4 2020), pp. 681–688. DOI: https://doi.org/10.1002/celc.202001445.

[36] Kevin W. Kimura, Rileigh Casebolt, Jessica Cimada DaSilva, Elyse Kauffman, Jiyoon Kim, Tyler A. Dunbar, Christopher J. Pollock, Jin Suntivich, and Tobias Hanrath. "Selective Electrochemical CO_2 Reduction during Pulsed Potential Stems from Dynamic Interface". In: *ACS Catalysis* 10 (15 2020), pp. 8632–8639. DOI: https://doi.org/10.1021/acscatal.0c02630.

[37] Max F. Döpke and Remco Hartkamp. "The importance of specifically adsorbed ions for electrokinetic phenomena: Bridging the gap between experiments and MD simulations". In: *J. Chem. Phys.* 154 (2021), p. 094701. DOI: https://doi.org/10.1063/5.0038161.

5

CONCLUSION AND RECOMMENDATIONS

5.1. CONCLUSION

This dissertation develops a comprehensive modeling framework for the CO_2ER. The research integrates advanced numerical modeling techniques to bridge key gaps in understanding the interplay of reaction kinetics, mass transport, and EDL effects. By addressing challenges in both H-cell and GDE systems, this work provides critical insights that not only advance the fundamental understanding of CO_2ER but also guide the design of scalable and efficient systems for carbon utilization.

A key focus of this dissertation has been the modeling of planar H-cell systems, presented in chapter 2. Previous studies often underpredict CO_2 concentration profiles or oversimplify the effects of EDL interactions on reaction kinetics. To address these shortcomings, the framework developed in this work extends the Poisson–Nernst–Planck equation to incorporate finite size effects and Frumkin-corrected kinetics. This enhancement enables precise predictions of CO_2 concentration gradients, local ionic concentration, and surface current densities, under industrially relevant operating conditions, such as high pressures and high potential. Validation against experimental data demonstrates the robustness and applicability of this model across a range of scenarios. One of the major enhancements of the model is related to the influence of steric effects. We concluded that numerical studies often overpredict the steric effects in CO_2ER, and a correct estimate required modification of the commonly used steric term to include the influence of solvent molecules. This work also advances the understanding of kinetic model incorporation in CO_2ER by demonstrating that models accounting for EDL interactions or steric effects must incorporate a Frumkin-corrected kinetic framework. These advancements provide researchers with a powerful numerical methodology to simulate the impact of operating parameters and optimize H-cell performance for both laboratory and industrial settings.

In Chapter 3, we delved into the intricate dynamics of GDE systems, where the incorporation of nanoporous structures enables improved mass transport by facilitating the

direct delivery of gaseous CO_2 to the catalyst layer. While this configuration enhances transport, it also introduces complex gradients in ion concentration, pH, and reactant availability within the pores, which strongly impact the reaction outcomes. To address these complexities, we developed a pore-scale model capable of resolving the interplay between these factors, shedding light on the critical influence of pore geometry, electrolyte composition, and EDL behavior on the local reaction environment. Our findings challenge the prevailing assumption that the local pH near the catalyst surface increases due to the consumption of H^+. Instead, we observed a significant drop in pH relative to bulk values, primarily driven by the electrostatic repulsion of OH^- ions. Furthermore, the electrolyte concentration was shown to play a pivotal role in determining the amount of dissolved CO_2 within the system, thereby shaping the overall reaction environment. We also discovered that contrary to expectations, smaller pores, which might be assumed to be more acidic due to higher mean potentials, can exhibit a more basic nature. This surprising behavior arises from factors such as carbonate balance and the increased surface-to-volume ratio within the smaller pores. By highlighting the delicate balance between pore radius and Debye length, our study identifies a key factor in controlling this behavior. By fine-tuning this balance, researchers can maintain optimal pH conditions near the reaction plane. This finding provides experimentalists with a valuable parameter for optimizing pore design in CO_2ER processes, offering a practical pathway to enhance reaction efficiency and selectivity.

An innovative contribution of this dissertation, presented in Chapter 4, is the exploration of pulsed electrolysis as an operational strategy for CO_2ER. Pulsed operation introduces dynamic conditions that alleviate limitations inherent in steady-state electrolysis, such as cation accumulation and CO_2 diffusion barriers within GDEs. By simulating various pulse durations for different CL thicknesses, we demonstrated that transient conditions can enhance Faradaic efficiency, catalyst utilization, and product selectivity. Notably, we discovered that the performance of the pulsed system is closely linked to the duration of the transient current density state. Prolonging this transient state, achieved by increasing the thickness of the CL, leads to improved Faradaic and cathodic efficiencies, as it extends cationic transport time and influences the CO_2 concentration at the reaction plane. Additionally, tuning the durations of each phase of the pulse, specifically using shorter pulses with unequal durations where the high-potential phase (τ_h) exceeds the low-potential phase (τ_l), resulted in better performance than equal-duration pulses. We also provided a practical approach to select the ideal pulse duration based on the CL thickness, facilitating optimal alignment between pulse parameters and the system's transport dynamics. Importantly, pulsed electrolysis was shown to yield current densities comparable to constant potential operation but with higher cathodic efficiency. These findings highlight the significant potential of pulsed electrolysis for GDE-based CO_2ER systems, offering a practical framework for researchers to optimize pulse parameters and CL design. This work provides valuable insights for enhancing reaction efficiency and selectivity, guiding future experimental efforts in the field of CO_2ER.

Beyond the specific findings of this work, the modeling methodologies developed herein are designed to be robust and versatile across a wide range of operating conditions. By adopting computationally efficient solutions to tackle numerically challenging problems—such as extreme concentration gradients and large cathodic potentials—the mod-

els ensure numerical tractability without compromising accuracy. This approach allows for easy implementation and adaptation, enabling researchers to apply these models to various CO_2ER systems. Consequently, the methodologies not only advance our understanding but also provide practical tools for optimizing and scaling up CO_2 electroreduction processes in both academic and industrial settings.

5.2. RECOMMENDATIONS

5.2.1. INCORPORATING BUBBLE DYNAMICS

Our work especially in regards to pulsed electrolysis in chapter 4 suggests that the current densities are high enough for the product species to reach their saturation limits quickly. In this dissertation, both CO and H_2 were assumed to predominantly remain in the dissolved phase. Hence, an accurate treatment necessitates the incorporation of bubble dynamics, as gas bubbles significantly impact local reaction environments by altering mass transport pathways, reducing active electrode surface area, and influencing electrolyte flow. Integrating the dynamics of bubble formation, growth, and detachment into the existing models can help researchers identify strategies to mitigate bubble-induced inefficiencies, enhance system performance, and extend the applicability of the modeling framework.

One potential approach to address this challenge is the use of semi-empirical relations to estimate effective surface coverage, mass transport modifications, and reaction rate corrections due to bubble presence. By employing experimentally validated models, these relations can provide a simplified yet effective way to account for the impact of bubbles on key parameters like local concentration gradients, active surface area, and gas saturation levels. Semi-empirical methods are computationally less intensive and can be incorporated into existing frameworks to provide quick approximations of bubble effects, especially when detailed bubble dynamics are not the focus of the study.

However, for more detailed and accurate simulations of bubble behavior and its influence on the electrochemical environment, we recommend using the phase-field method. The phase-field approach is particularly advantageous because it naturally captures complex interface phenomena, such as bubble formation, coalescence, breakup, and detachment, without requiring explicit tracking of the gas-liquid interface. It integrates seamlessly with the finite element method described in this dissertation, enabling accurate modeling of surface tension effects, dynamic interactions between electric fields and bubbles, and bubble-driven flow perturbations. Employing the phase-field method allows researchers to develop a more comprehensive understanding of bubble-induced inefficiencies and optimize system performance with higher fidelity compared to semi-empirical models.

5.2.2. OPTIMIZING CATALYST LAYER UTILIZATION

Our findings in Chapter 4 demonstrated that a significant portion of the catalyst layers (CLs) in gas diffusion electrodes (GDEs) remains largely inactive for CO_2 electroreduction (CO_2ER). Only the regions of the CLs located near the gas/liquid interface contribute significantly to the spatially averaged current density. At the same time, we observed that increasing the thickness of the CL prolongs the transient state, which, in turn, reduces steric hindrance for CO_2 diffusion. This interplay between CL thickness, cation

penetration, and resulting current densities suggests a complex relationship that can be strategically optimized.
One promising approach to address this balance is the use of partially coated active catalyst layers. By selectively activating specific regions of the CL, it is possible to both enhance the utilization of the active surface area near the gas/liquid interface and minimize the effects of cation-induced transport limitations deeper within the CL. To achieve this optimization, we recommend researchers employ the pulsed electrolysis modeling strategy outlined in this work, specifically adapted for partially coated CLs. This approach can help maximize the current density over an extended duration by leveraging the dynamic effects of pulsed conditions to regulate local ionic distributions and mitigate transport limitations effectively.

5.2.3. MULTISCALE MODELS

This dissertation has focused on providing a sub-micron scale understanding of phenomena rooted in molecular or atomic interactions, including electrode kinetics, EDL formation, and steric effects. By integrating these fundamental processes with ion transport models, we have uncovered key performance-determining mechanisms such as the influence of EDL structure, intense electric fields, and steep concentration gradients near the electrode surface and clarified the interplay among them. Building on the insights obtained from our H-cell and pore-scale models, it is a natural progression to develop multiscale models that incorporate these localized phenomena into broader reactor-level dynamics.
To scale our findings to industrial reactors, we must account for larger-scale variables such as flow distribution, pressure drops, and thermal management. Integrating the models generated in this work with reactor-level simulations can therefore guide the design of reactors that simultaneously optimize micro- and macro-scale performance, accelerating the development of practical, scalable CO_2ER. For example, to scale up pore-scale models such as the one presented in chapter 3 and 4, one can determine spatially averaged current densities and concentration fields that serve as input for electrode-level models. At this electrode scale, the electrode is treated as a continuum, allowing these averaged parameters to represent the net effect of complex pore geometries without resolving each pore explicitly. These electrode-scale results then provide boundary conditions such as effective current density distributions, concentration gradients, and reaction rates—for cell-level simulations, where the bulk electrolyte flow and associated mass, momentum, and heat transport are typically modeled using CFD. Finally, with cell-level performance metrics and operating conditions defined, it is possible to scale up to the stack level, integrating multiple cells into a larger assembly that accounts for manifold design, pressure drops, thermal effects, and overall reactor performance. In this way, the localized insights from pore-scale models guide the design and optimization at progressively larger scales, ensuring that microscale phenomena are reflected in system-level predictions for more realistic and scalable CO_2ER technologies.

5.2.4. INCLUDING ATOMISTIC/MOLECULAR INFORMATION

Based on the findings presented in this dissertation, it is evident that the EDL plays a critical role in shaping the local reaction environment by creating regions of concentrated

ionic species, such as K^+, near the electrode surface. These concentrated species can significantly influence the effective diffusivities of ions and molecules within the EDL, ultimately impacting mass transport and reaction kinetics. To further explore and quantify these effects, Molecular Dynamics (MD) simulations offer a powerful tool for advancing our understanding. MD simulations can provide detailed insights into how the local ionic environment affects diffusivities by resolving the atomic-scale interactions between ions, solvent molecules, and the electrode surface. MD can calculate the effective diffusivities of key species in the highly structured EDL region, accounting for confinement effects, solvation structures, and electrostatic interactions that continuum models cannot fully capture. These effective diffusivities can then feed into pore-scale models to capture the physics more thoroughly. Furthermore, in chapter 2 we concluded that the solvent molecules play a crucial role in determining the magnitude of steric repulsion. In this regard, MD can explore the role of water molecules and hydration shells in mediating ionic interactions and affecting transport properties near the electrode.

Our findings show that the pulsed operation strategy introduced in Chapter 4 can help mitigate surface poisoning by periodically altering the local environment and thereby reducing the buildup of harmful species. To fully understand and quantify this effect, atomic-scale modeling approaches can be leveraged to explore the mechanisms of adsorbate removal, restructuring events, and changes in binding energies that occur during pulsed operation. Such simulations can provide direct insight into how these transient conditions influence the catalyst surface at the atomic level, ultimately guiding the design of more durable and effective CO_2ER systems.

5.2.5. EXPANDING TO MULTI-CARBON PRODUCT PATHWAYS

Extending our focus on reaction pathways and local reaction environments, it is also logical to expand our models to include multi-carbon (C_2^+) products, such as ethylene and ethanol. While this dissertation primarily focused on the production of CO, C_2^+ products are economically valuable, and their formation involves complex reaction pathways sensitive to factors we have extensively studied, such as local pH, ion concentrations, and EDL effects. By adapting our modeling framework to account for the kinetics and transport phenomena associated with C_2^+ product formation, researchers can leverage our insights to maximize yields of these valuable products, thereby improving the economic feasibility of CO_2ER technologies and naturally extending our findings.

5.2.6. SUSTAINABILITY AND ECONOMIC ASSESSMENTS

Lastly, considering the environmental impact and sustainability of CO_2ER processes, integrating our modeling framework with life cycle assessment (LCA) and techno-economic analysis (TEA) would provide a holistic view of the technology's viability. By coupling our detailed models with LCA and TEA, researchers can identify the most sustainable and cost-effective strategies for implementing CO_2ER at scale, ensuring that technological advancements align with environmental and economic goals.

By pursuing these extensions of our work, researchers can further enhance the efficiency, scalability, and applicability of CO_2ER technologies. The methodologies and insights developed herein provide a robust platform for future exploration and innovation, facilitating the transition from theoretical understanding to industrial-scale solutions.

ACKNOWLEDGEMENTS

First and foremost, I would like to express my deepest gratitude to **Professor Johan Padding** for his excellent and kind supervision throughout my PhD journey. His unwavering positivity, even during challenging times, has been a tremendous source of motivation. His profound understanding of various aspects of physics and science has not only surprised me but also guided me through the complexities of my research. I feel truly privileged to have had his guidance during this critical phase of my career. I also extend my heartfelt thanks to **Dr. Remco Hartkamp** for his invaluable input and critical feedback, which has greatly supported my academic growth and will surely help me in my future career. His encouragement and support have been instrumental in pushing me to excel. I am deeply grateful for his willingness to help me, both academically and personally, whenever I sought his guidance. His support has truly been a cornerstone of my PhD experience.

To **Arvind Pari**, Mr. Dependable—you have been my go-to person for any kind of help I needed. That said, I'll never forget the time we missed the flight... but we don't talk about that! Our PhD journeys have been practically identical since day one, and your friendship and support have been invaluable throughout this journey. To **Joe Blake**, thank you for all the interesting discussions, ranging from CO_2 electrolysis to obscure internet meme culture and everything in between. To **Rong Fan** and **Rumen Georgiev**, thank you for your guidance and for creating a welcoming atmosphere in the office. To **Nagaraj Nagalingam** and **Ravi Ramesh**, I am grateful for the casual yet refreshing conversations. Thanks to **Vigness Murugesan**, **Nikhilesh Kodur**, **Fataah Ansar**, and **Ali Amiri** for keeping the office lively and fostering such a vibrant work environment. I wish you all the very best in successfully completing your own PhD journeys.

A heartfelt thanks to my parents and my sister. Saying that you have always had my back would be an understatement. You have always believed in me and supported every decision I made. I would not have reached this point without the sacrifices you made. Your unwavering support and faith in me have been the foundation of all my achievements. In moments of uncertainty, the comfort of your voices has always steadied me. Finally, to **Zara**, my wife, words cannot express my gratitude for the strength and support you have provided over the last four years. You have been my unwavering source of inspiration and, dare I say, my lucky charm. On the day we got married, I got published, and on our first anniversary, I stepped into the next phase of my career. Thank you for being there through every challenge and triumph.

To everyone who has been part of this journey, thank you from the bottom of my heart.

A

APPENDIX TO CHAPTER 2

A.1. SUPPLEMENTARY RESULTS

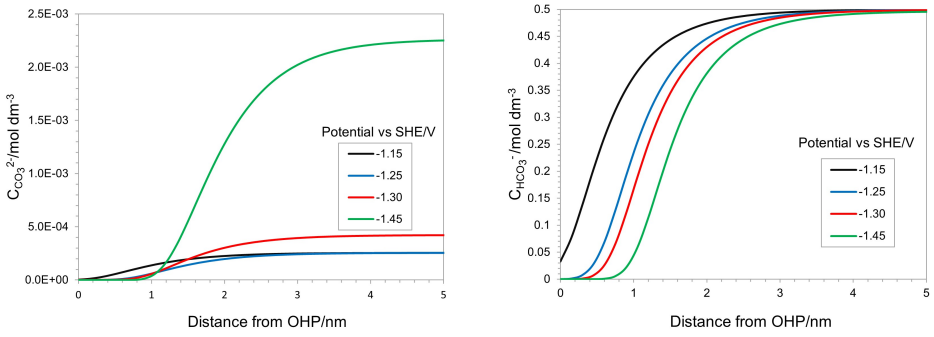

(a) (b)

Figure A.1: Concentration profile of $HCO_3{}^-$ and $CO_3{}^{2-}$ near the surface of the electrode at varied applied electrode potentials for a 0.5M $KHCO_3$ solution at 5 bar CO_2 pressure.

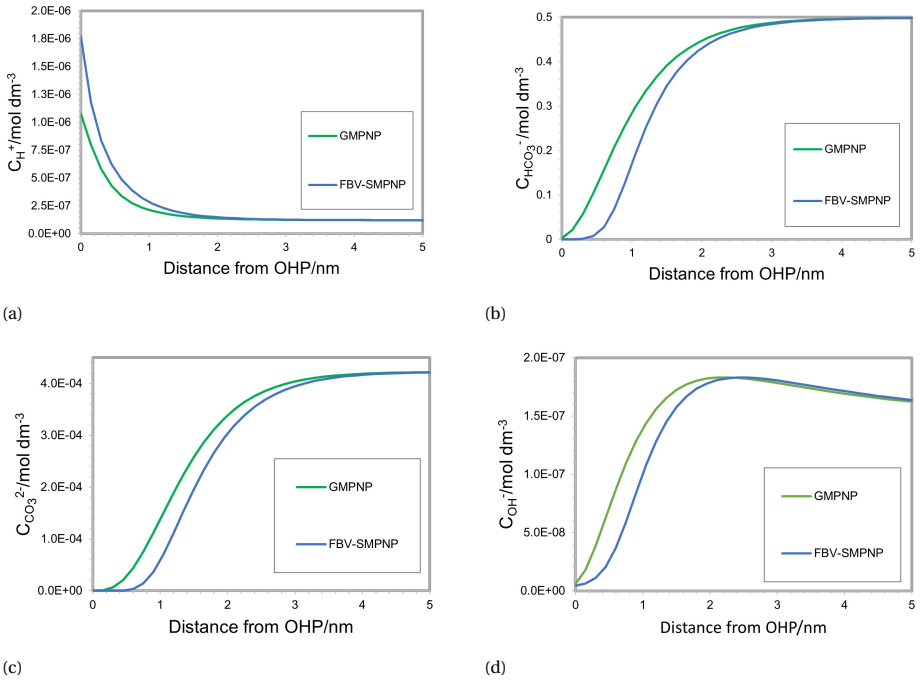

Figure A.2: Comparison of concentration profiles of different species using FBV-SMPNP and GMPNP approach for 0.5M $KHCO_3$ solution at -1.4 VS SHE/V in a 5 bar CO_2 electrolyzer.

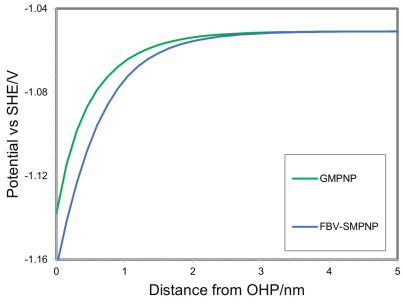

Figure A.3: Comparison of electric potential near the electrode surface using FBV-SMPNP and GMPNP approach for a 0.5M $KHCO_3$ solution at applied electrode potential of -1.4 VS SHE/V in a 5 bar CO_2 electrolyzer. The potential profiles become steady after some distance from OHP. This is the point beyond which potential is 0 vs PZC/V (bulk boundary condition).

B

APPENDIX TO CHAPTER 3

B.1. SUPPLEMENTARY RESULTS FOR GDE MODEL

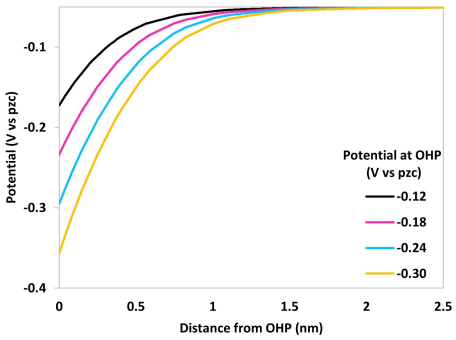

Figure B.1: Radial variation of potential profile with increasing Φ_{OHP} inside a pore of R= 2.5 nm and L=50 nm for an electrolyte concentration of 1.0 M KHCO3 at I_{ECSA} of 2 mA.cm^{-2} and CO_2 pressure= 1.0 bar.

B

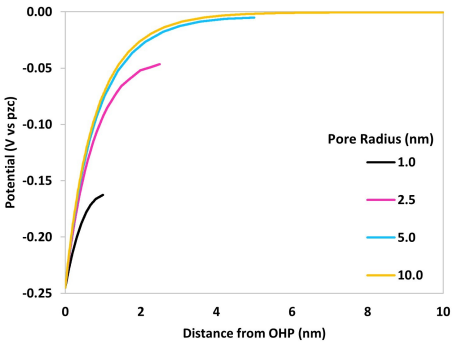

Figure B.2: Radial variation of potential profile with changing pore radius at Φ_{OHP} =-0.24 V vs SHE for an electrolyte concentration of 0.1 M KHCO3 at I_{ECSA} of 2 mA.cm^{-2} and CO_2 pressure= 1.0 bar.

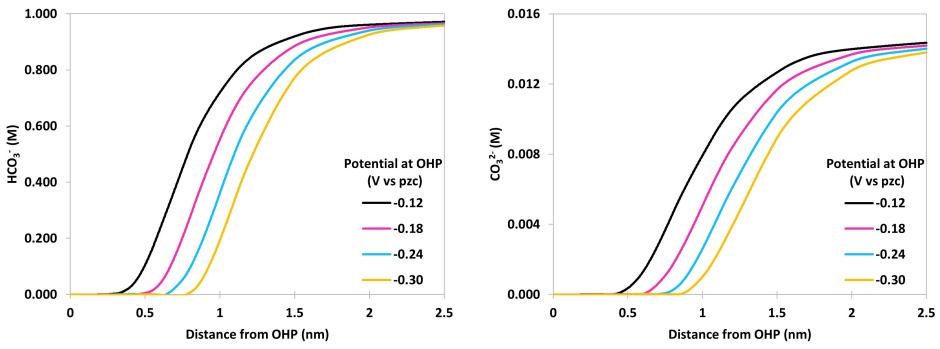

(a) (b)

Figure B.3: Radial variation of concentrations as a result of changing OHP potential (V vs pzc) for an Ag (111) catalytic nanopore (R=2.5 nm, L=50 nm) in a 1.0 M $KHCO_3$ solution at I_{ECSA} of 2 mA.cm^{-2} and 1 bar CO_2 pressure.

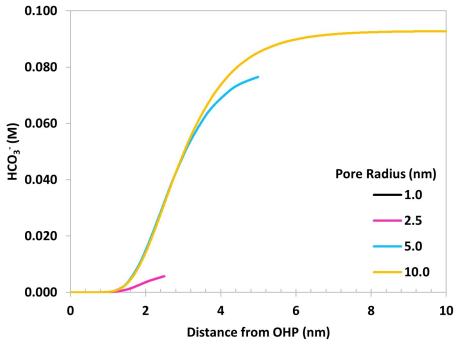

Figure B.4: Radial variation of HCO_3^- concentration with changing pore radius at Φ_{OHP} =-0.24 V vs SHE for an electrolyte concentration of 0.1 M KHCO3 at I_{ECSA} of 2 mA.cm^{-2} and CO_2 pressure= 1.0 bar.

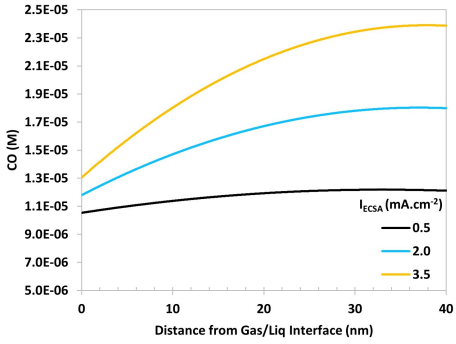

Figure B.5: Longitudinal variation of CO concentration with changing I_{ECSA} at Φ_{OHP} =-0.24 V vs SHE for a pore (R=2.5 nm, L=50 nm) in an electrolyte concentration of 0.1 M $KHCO_3$ and CO_2 pressure= 1.0 bar.

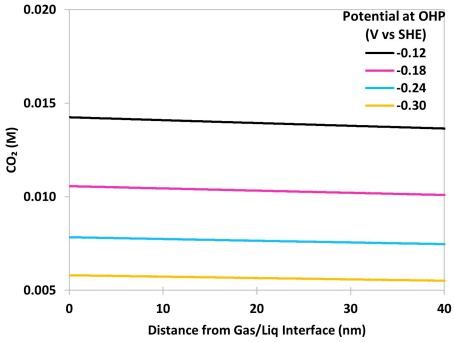

Figure B.6: Longitudinal variation of CO_2 concentration with changing OHP potential (V vs pzc) for an Ag (111) catalytic nanopore (R=2.5 nm, L=50 nm) in a 1.0 M $KHCO_3$ solution at I_{ECSA} of 2 mA.cm^{-2} and 1 bar CO_2 pressure.

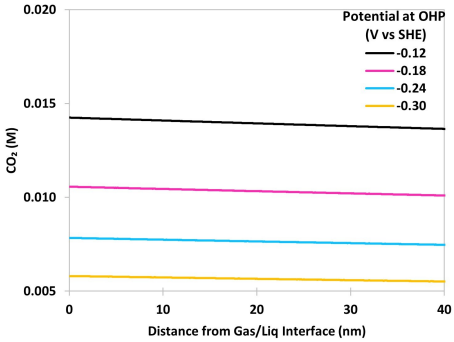

Figure B.7: Longitudinal variation of CO_2 concentration with changing OHP potential (V vs pzc) for an Ag (111) catalytic nanopore (R=2.5 nm, L=50 nm) in a 1.0 M $KHCO_3$ solution at I_{ECSA} of 2 mA.cm^{-2} and 1 bar CO_2 pressure.

C

APPENDIX TO CHAPTER 4

C.1. SUPPLEMENTARY RESULTS

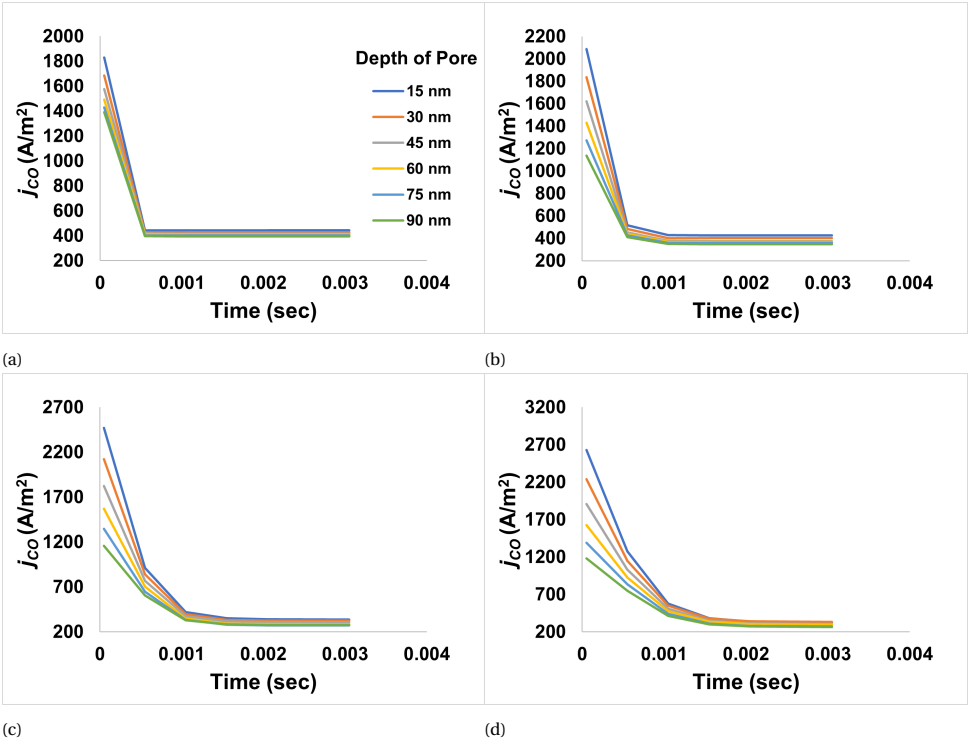

Figure C.1: Variation of j_{CO} with time during the Φ_h of the pulsed operation at different depths for, (a) 100 nm CL, (b) 200 nm CL, (c) 300 nm CL, (d) 400 nm CL.

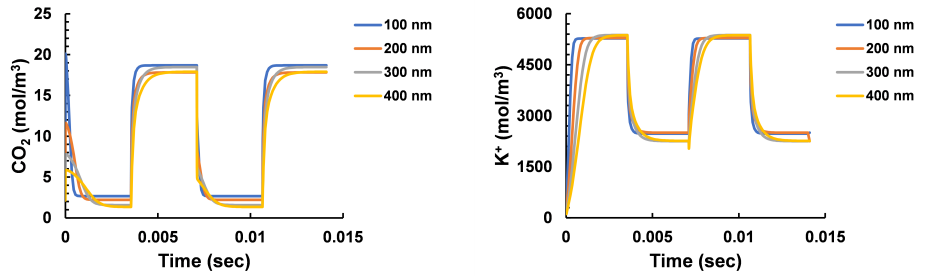

(a) (b)

Figure C.2: Concentration profile under pulsed electrolysis for a 200 nm thick catalyst layer, (a) CO_2, (b) K^+.

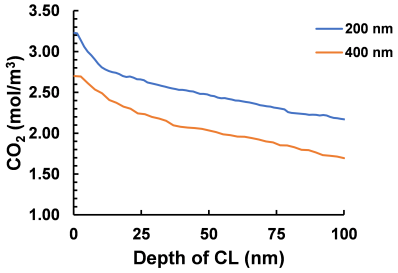

Figure C.3: Steady state concentration profile of CO_2 along the depth of the catalyst layer for a total CL thickness of 200 and 400 nm.

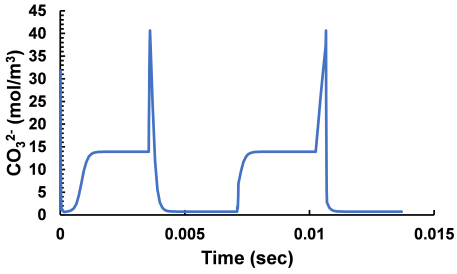

Figure C.4: Mean Concentration profile of $CO_{32}{}^{-}$ under pulsed electrolysis for a 200 nm thick catalyst layer.

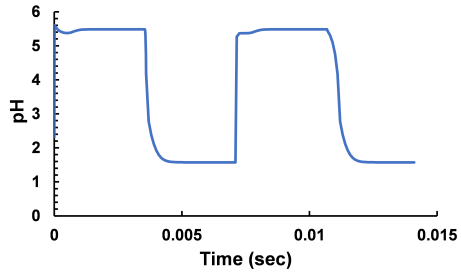

Figure C.5: pH profile of a system under pulsed electrolysis measured at r = 0 nm for a 200 nm thick catalyst layer.

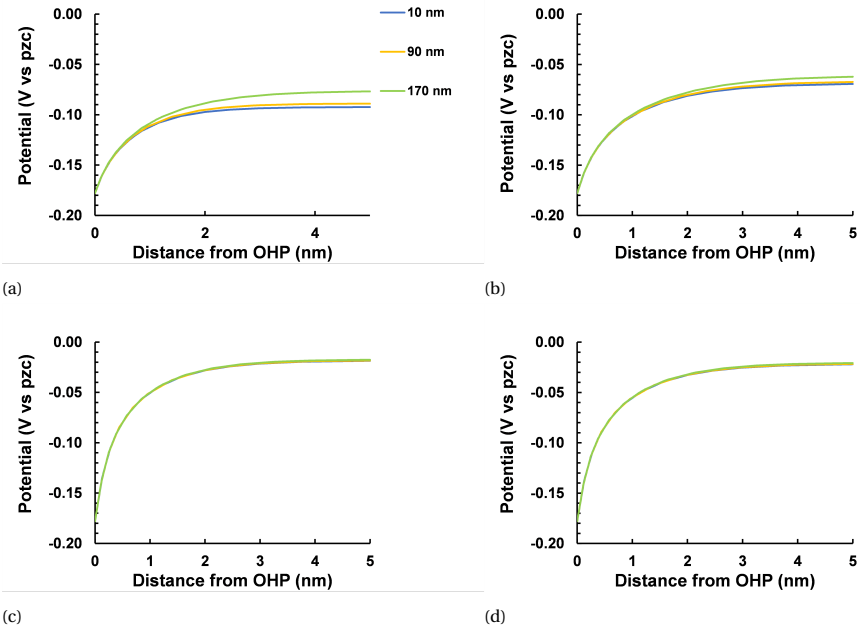

Figure C.6: Variation of potential from the OHP towards the centre during the Φ_h section of the pulse at various depths of the CL after, (a) 1.0e^{-5} sec, (b) 5.0e^{-5} sec, (c) 5.0e^{-4} sec, (d) 1.0e^{-3} sec. For polycrystalline Ag potential of zero charge (pzc) = -0.7 V vs SHE

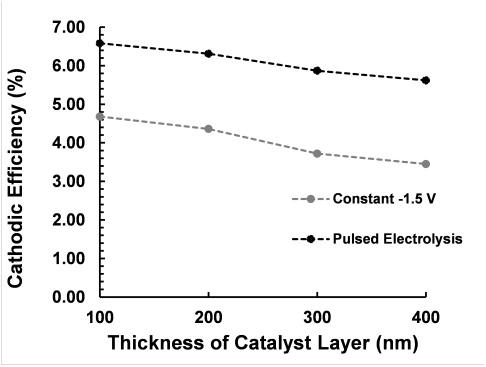

Figure C.7: Cathodic efficiency for a system under pulsed electrolysis compared to a constant potential operation at -1.5 V at various thicknesses of the catalyst layer. Cathodic Efficiency = $\frac{\Phi^0}{\Phi_m} * FE_{CO}$

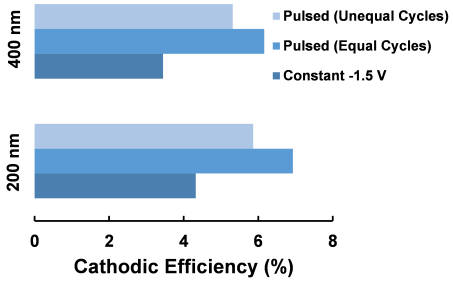

Figure C.8: Cathodic efficiency comparison for varying durations of the pulse.

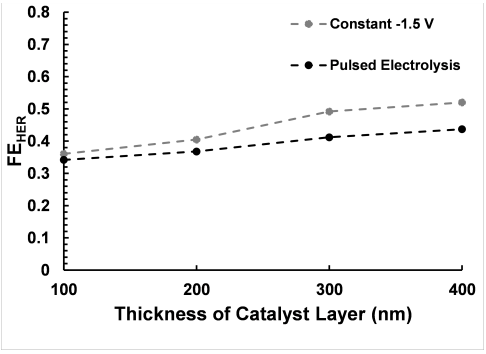

Figure C.9: FE of HER under pulsed electrolysis compared to a constant potential system at -1.5 V, for various thicknesses of the CL. Φ_h= -1.5 V, Φ_l= -0.7 V, τ_h= τ_l= 0.0035 s.

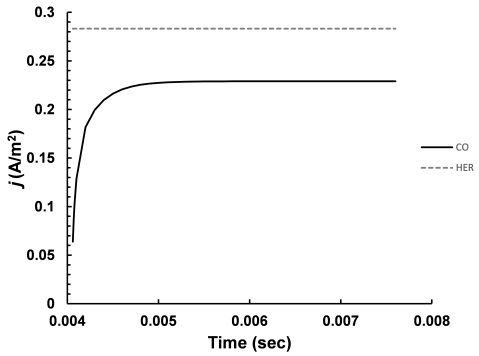

Figure C.10: CO_2ER and HER current density during the Φ_l section of the pulse.

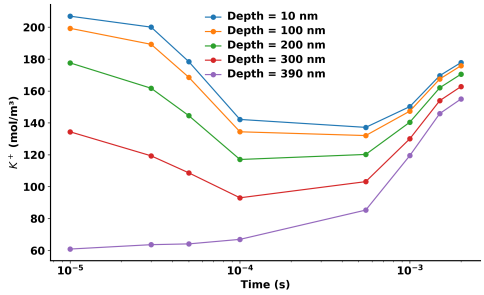

Figure C.11: Temporal trend of K^+ at the axisymmetric center (y=0) of a 400 nm thick CL at different depths of the CL.

D

HOMOGENEOUS REACTION MODEL AND PARAMETRIC DATA

D.1. BULK CONCENTRATIONS

Henry's law is assumed to be valid for CO_2 gas and Eq. (D.1) is used to evaluate the bulk concentration of CO_2 in water.

$$CO_2{}^0_{aq} = K^0_H C_{CO_2,g} \tag{D.1}$$

Henry's constant K^0_H is temperature dependent and in the presented system the temperature is taken as 298.15 K. The following equation is used to calculate its value:

$$\ln K^0_H = 93.4517 \times \frac{100}{T} - 60.2409 + 23.3585 \ln \frac{T}{100} \tag{D.2}$$

CO_2 concentration in an electrolyte will be different than in pure water. The saturated concentration of CO_2 in the electrolyte ($CO_{2\,aq}$) is given by:

$$\log\left(\frac{CO_2{}^0_{aq}}{CO_{2\,aq}}\right) = K_s C_s \tag{D.3}$$

here C_s is the concentration of electrolyte and for our work, it is 0.5 M $KHCO_3$. K_s is the Sechenov's constant given by [1]:

$$K_s = \sum_i (h_{CO_2} + h_i) n_i \tag{D.4}$$

where h_i is the Sechenov parameter for ion i and is given in Table D.1. h_{CO_2} is calculated using:

$$h_{CO_2} = h_{CO_2,0} + h_{CO_2,T}(T - 298.15) \tag{D.5}$$

and n_i is defined as:

$$n_i = \frac{c_i}{C_s} \tag{D.6}$$

Here c_i represents the ionic concentrations before injecting the CO_2 gas and are calculated from the solution of equilibrium of Eqs. (2.1-2.3) in chapter 2. The calculated concentration of saturated CO_2 (CO_{2aq}) is then used to determine the bulk concentration of all other solution species post CO_2 saturation. This balance is given by (D.7-D.11). These equations are solved until a steady state is achieved. The bulk concentration values for all solution species for both 5 and 40 bar pressure are given in Table D.8. The bulk rate equations are given by:

$$R_{H^+} = k_3 - k_{-3} C_{H^+} C_{OH^-} \tag{D.7}$$

$$R_{CO_2} = -k_2 C_{CO_2} C_{OH^-} + k_{-2} C_{HCO_3^-} \tag{D.8}$$

$$R_{CO_3^{2-}} = k_1 C_{HCO_3^-} C_{OH^-} - k_{-1} C_{CO_3^{2-}} \tag{D.9}$$

$$R_{HCO_3^-} = -k_1 C_{HCO_3^-} C_{OH^-} k_{-1} C_{CO_3^{2-}} + k_2 C_{CO_2} C_{OH^-} - k_{-2} C_{HCO_3^-} \tag{D.10}$$

$$R_{OH^-} = k_3 - k_{-3} C_{H^+} C_{OH^-} - k_2 C_{CO_2} C_{OH^-} + k_{-2} C_{HCO_3^-} - k_1 C_{HCO_3^-} C_{OH^-} + k_{-1} C_{CO_3^{2-}} \tag{D.11}$$

D.2. PARAMETRIC DATA

Table D.1: Sechenov Parameters (m^3kmol^{-1}). [1]

Species(i)	h_i
CO_3^{2-}	0.1423
OH^-	0.0839
HCO_3^-	0.0967
K^+	0.0922
CO_2,0	-0.0172
CO_2,T	-0.000338

Table D.2: Rate Constants.[2, 3]

Constant	Value	Unit
k_1	6.0×10^6	$mol^{-1}m^3s^{-1}$
k_{-1}	1.07×10^6	s^{-1}
k_2	2.23	$mol^{-1}m^3s^{-1}$
k_{-2}	5.23×10^{-5}	s^{-1}
k_3	2.4×10^{-2}	$molm^{-3}s^{-1}$
k_{-3}	2.4×10^6	$mol^{-1}m^3s^{-1}$

Table D.3: GDE Geometry.

Parameter	Value	unit
L_c	1.5×10^{-2}	m
L_{cross}	1.0×10^{-5}	m
A_{cross}	1.5×10^{-7}	m^2

Table D.4: Diffusivities ($m^2 s^{-1}$).[4, 5]

Species	Value
CO_3^{2-}	0.92×10^{-9}
OH^-	5.23×10^{-9}
HCO_3^-	1.18×10^{-9}
K^+	1.95×10^{-9}
CO_2	1.91×10^{-9}
H^+	9.31×10^{-9}
CO	2.03×10^{-9}
H_2	4.50×10^{-9}

Table D.5: Species Sizes (m).[6]

Species	Value
$a_{CO_3^{2-}}$	0.788×10^{-9}
a_{OH^-}	0.60×10^{-9}
$a_{HCO_3^-}$	0.80×10^{-9}
a_{K^+}	0.66×10^{-9}
a_{CO_2}	0.33×10^{-9}
a_{H^+}	0.56×10^{-9}
a_{CO}	0.113×10^{-9}
a_{H_2}	0.074×10^{-9}
a_{H_2O}	0.30×10^{-9}

Table D.6: Henry's Constant ($mol\,kg^{-1}\,bar^{-1}$).[7]

Species	Value
H_{CO}	9.5×10^{-4}
H_{H_2}	7.80×10^{-4}

Table D.7: Other Simulation Parameters for GDE.

Parameter	Value	unit
μ_{elec}	0.89×10^{-3}	$kg\,m^{-1}s^{-1}$
V_{elec}	0.25×10^{-6}	$m^3 s^{-1}$
ρ_{elec}	997	$kg\,m^{-3}$
p_1	1.0	bar
y_{CO_2}	0.95	–
y_{CO}	0.45	–
y_{H_2}	0.05	–
f_r	150	–
FE_{CO}	95	%
FE_{H_2}	5	%

Table D.8: Bulk Concentrations at 5 and 40 bar CO_2 pressure (mol dm^{-3}).

Species	C_i(5 bar)(pH = 6.9)	C_i(40 bar)(pH = 6.1)
CO_3^{2-}	0.23×10^{-3}	0.28×10^{-4}
OH^-	0.82×10^{-7}	0.10×10^{-7}
HCO_3^-	0.49	0.49
K^+	0.50	0.50
H^+	0.12×10^{-6}	0.97×10^{-6}
CO_2	0.17	1.36

Table D.9: Equilibrium Potential (V vs SHE).[8]

Reaction	Value
$CO_2(aq) + H_2O + 2e^- \rightleftharpoons HCOO^- + OH^-$	−0.43
$CO_2(aq) + H_2O + 2e^- \rightleftharpoons CO(g) + 2OH^-$	−0.53
$2H_2O + 2e^- \rightleftharpoons H_2(g) + 2OH^-$	−0.41

BIBLIOGRAPHY

[1] S Weisenberger and A Schumpe. “Estimation of gas solubilities in salt solutions at temperatures from 273 K to 363 K”. In: *AIChE Journal* 42 (1 Jan. 1996). doi: 10.1002/aic.690420130, pp. 298–300. ISSN: 0001-1541. DOI: 10.1002/aic.690420130. URL: https://doi.org/10.1002/aic.690420130.

[2] K. G. Schulz, U. Riebesell, B. Rost, S. Thoms, and R. E. Zeebe. “Determination of the rate constants for the carbon dioxide to bicarbonate inter-conversion in pH-buffered seawater systems”. In: *Marine Chemistry* 100 (1-2 2006), pp. 53–65. ISSN: 03044203. DOI: 10.1016/j.marchem.2005.11.001.

[3] Peter Atkins, Julio de Paula, and James Keeler. *Atkins' Physical Chemistry 11e*. 11th ed. Vol. 2. Oxford University Press, 2018.

[4] John Rumble. *Handbook of Chemistry and Physics*. 100th ed. CRC Press, 2019.

[5] Bernd Jähne, Gerhard Heinz, and Wolfgang Dietrich. “Measurement of the diffusion coefficients of sparingly soluble gases in water”. In: *Journal of Geophysical Research* 92 (C10 1987), p. 10767. ISSN: 0148-0227. DOI: 10.1029/JC092iC10p10767.

[6] E Nightingale. “PHENOMENOLOGICAL THEORY OF ION SOLVATION. EFFECTIVE RADII OF HYDRATED IONS”. In: *J. Phys. Chem* (1959).

[7] R. Sander. “Compilation of Henry's law constants (version 4.0) for water as solvent”. In: *Atmos. Chem. Phys.* 15 (2015), pp. 4399–4981. DOI: https://doi.org/10.5194/acp-15-4399-2015.

[8] Jinli Qiao, Yuyu Liu, and Jiujun Zhang. *Electrochemical Reduction of Carbon Dioxide*. 1st ed. CRC Press, 2016.

CURRICULUM VITÆ

ESAAR NAEEM BUTT

18-11-1992 Born in Gujranwala, Pakistan.

EDUCATION

2011–2015 Bachelors in Chemical Engineering
National University of Sciences & Technology
Islamabad, Pakistan

2016–2019 Master's in Chemical & Energy Engineering
Otto von Guericke University
Magdeburg, Germany

2019–2025 PhD
Delft University of Technology
Thesis: Modeling the local reaction environment in CO_2 electrolysis.
Promotors: Prof. dr. ir. J.T. Padding and dr. ir. R.M. Hartkamp

EXPERIENCE

2013 Quality Assurance Intern
CocaCola Beverages Pakistan Ltd
Gujranwala, Pakistan

2014 Operations Intern
Fatima Fertilizer Pakistan Ltd
Sadiqabad, Pakistan

2016–2019 Student Researcher
Otto von Guericke University
Magdeburg, Germany

LIST OF PUBLICATIONS

3. **Butt E. N., Padding J. T. and Hartkamp R. M.**, *Size-modified Poisson-Nernst-Planck approach for modeling a local electrode environment in CO_2 electrolysis*, Sustainable Energy and Fuels **7**, 144 (2023).

2. **Butt E. N., Padding J. T. and Hartkamp R. M.**, *Local Reaction Environment Deviations within Gas Diffusion Electrode Pores for CO_2 Electrolysis*, Journal of the Electrochemical Society **171**, (2024).

1. **Butt E. N., Padding J. T. and Hartkamp R. M.**, *Unlocking the Potential of Pulsed Electrolysis: Mechanisms for Improved CO_2 Electroreduction in GDE Systems (Submitted for publication)* .